A Study of Bhabha Scattering at the Z Resonance

Thesis by
Wenwen Lu

In Partial Fulfillment of the Requirements
for the Degree of

Doctor of Philosophy

California Institute of Technology
Pasadena, California

1997
(Submitted September 12, 1997)

Acknowledgments

I would like to take this chance to acknowledge the support and guidance of my advisor at Caltech, Prof. Harvey Newman. I would also like to express my gratitude to Prof. Samuel C. C. Ting for providing me the opportunity to join the L3 experiment.

I thank the members of the L3 Lineshape Group — in particular Joachim Mnich, Martin Grünewald, Albrecht Böhm, John Field, Maria Kienzle, Dimitri Bourilkov, Ulrich Uwer and Christoph Paus — for many stimulating discussions and for all the things I learned from them. I thank Giorgio Gratta for guiding my work during his time at CERN, and for teaching me the RFQ calibration techniques.

I am very grateful to Harvey Newman, Joachim Mnich, Martin Grünewald and Jayant Shukla for their careful reading of this manuscript and their constructive criticism.

I thank all my friends with whom I worked and played, who had made my stay at CERN such an unforgettable experience: Yuan-Han Chang, Tie-Sheng Dai, Jian-Chun Wang and his wife Jing, Yi-Fang Wang and his wife Hong, Jian-Guo Xu and his wife Hong-Yan, Bing Zhou, Yuan Zhou, Aaron Dominguez and his wife Julie, Frank Filthaut, Mirna van Hoek, David McNally and his wife Shannon, Tom Paul, Gerhard Raven, Tajsa van Rhee, Jayant Shukla, Alex Shvorob, Chris Tully and many others.

Last, but not at all least, I thank my family for the love and encouragement they have given me during my studies. This thesis is dedicated to my mother.

Abstract

In this thesis, I present a study on Bhabha scattering at the Z resonance using the L3 detector at LEP. I have measured the cross section and forward-backward asymmetry measurement for the process $e^+e^- \rightarrow e^+e^-(n\gamma)$ in the large angle region ($44^\circ < \theta_{e^+e^-} < 136^\circ$). The data used was collected during 1993 (3 energy points at the Z resonance) and 1994 (Peak point only), corresponding to a total of 66,000 e^+e^- pairs. The results of my measurement are combined with those from other L3 measurements of Z production and decays to provide a precision test of the Standard Model. Electroweak parameters are determined with unprecedented precision.

The main results in this thesis are as follows:

- the cross section of $e^+e^- \rightarrow e^+e^-(n\gamma)$ process at the Z peak:
  $\sigma = 1.072 \pm 0.005\ (stat.) \pm 0.002\ (sys.)$ nb,
- the forward-backward asymmetry of $e^+e^- \rightarrow e^+e^-(n\gamma)$ process at the peak:
  $A_{FB} = 0.122 \pm 0.006\ (stat.) \pm 0.003\ (sys.)$,
- the mass of the Z boson: $M_Z = 91188.3 \pm 2.9$ MeV,
- the total width of the Z boson: $\Gamma_Z = 2499.8 \pm 4.3$ MeV,
- the partial decay width of the Z boson into electrons:
  $\Gamma_e = 83.99 \pm 0.26$ MeV,
- the Z electroweak coupling constants to fermions:
  $\overline{g}^l_V = -0.0398^{+0.0027}_{-0.0029}$, $\overline{g}^l_A = -0.5010 \pm 0.0006$,
- the effective weak mixing angle: $\sin^2\bar{\theta}_W = 0.2304 \pm 0.0009$,

- the mass of the top quark: $M_t = 189^{+12}_{-13} \pm 17$ GeV,
- the mass of the Higgs boson: $M_H = 91^{+230}_{-81}$ GeV; $M_H < 645$ GeV $95\% CL$.

All the results from different measurements yield consistent results. No indication of a deviation from the Standard Model has been observed.

Contents

List of Tables

List of Figures

Chapter 1

Introduction and Overview

In this thesis, I present my study of the process $e^+e^- \rightarrow e^+e^-(n\gamma)$, *Bhabha Scattering*, at the Z resonance. The motivation for this study is two-fold:

(1) to determine the electroweak parameters such as the mass, the total width, the partial width of the Z boson: M_Z, Γ_Z, Γ_f and also the electroweak vector and axial-vector coupling constants g_V and g_A,

(2) to search for deviations from the Standard Model electroweak theory.

The data sample analyzed in the thesis has been collected by the L3 detector at LEP in 1993 and 1994. Z bosons are copiously produced at LEP in a very clean experimental environment via electron-positron annihilations. In 1993, an energy scan of the Z resonance was performed with half of the total 30 pb^{-1} luminosity at the two energy points approximately 2 GeV below and above the Z pole, and the other half of the luminosity on the Z peak. In 1994, a total luminosity of 40 pb^{-1} was taken on the Z peak. In total, 66,000 e^+e^- pairs of the Z decays are selected for the study of this thesis.

In the Standard Model, Z bosons decay into fermion pairs $f\bar{f}$. In lowest order, the $e^+e^- \rightarrow Z \rightarrow f\bar{f}$ cross section and forward-backward asymmetry are correlated with the electroweak parameters through the following relations:

- cross section (Z exchange)

$$\sigma(s) = \frac{12\pi}{M_Z^2}\frac{\Gamma_e\Gamma_f}{\Gamma_Z^2}\frac{s\Gamma_Z^2}{(s-M_Z^2)^2+s^2\Gamma_Z^2/M_Z^2} \tag{1.1}$$

$$\Gamma_f \propto (g_V^f)^2 + (g_A^f)^2, \tag{1.2}$$

- asymmetry at the Z pole

$$A_{FB}^{0,l} = \frac{3}{4} A_e A_f \tag{1.3}$$

$$A_f = \frac{2 g_V^f g_A^f}{(g_V^f)^2 + (g_A^f)^2}. \tag{1.4}$$

By measuring the cross section and the forward-backward asymmetry of the e^+e^- channel and combining the results with those from other channels, I am able to measure the electroweak parameters with high precision. The mass of the Z boson is determined with a precision of 10^{-5}, which is comparable to the precision of the Fermi constant G_F. With such a precise measurement, I am able to check the validity of the Standard Model and to search for new physics beyond it.

This thesis is organized as follows.

In Chapter 2, I describe the framework of the electroweak theory in the Standard Model. I concentrate on the subjects relevant to Z physics at an e^+e^- collider. Special features of Bhabha scattering are discussed.

Chapter 3 is devoted to the description of the L3 detector setup and the LEP e^+e^- collider facility.

In Chapter 4, I discuss the calibration techniques used for the Electromagnetic Calorimeter (ECAL), which is crucial for my high precision measurement of electron and photon final states. The discussion emphasizes a new *RFQ calibration* technique, which has been developed and put into use by the Caltech L3 group with major contributions from me.

In Chapter 5, I present my measurement of the cross section and forward-backward asymmetry of $e^+e^- \rightarrow e^+e^-(n\gamma)$. I have developed a new selection which is based on the information from the central tracker, the Time-Expansion-Chamber (TEC).

By controlling the TEC efficiency with a precision of 0.1%, I have studied in detail the events with $e^+e^-(n\gamma)$ (n=1,2,3) final states and I have been able to measure the cross section with a systematic error of $0.2 - 0.3\%$.

Chapter 6 presents the results on the determination of electroweak parameters, by combining my measurement of the e^+e^- channel with the results from other channels. Limits on new physics processes are derived.

Chapter 7 summarizes this thesis and concludes with remarks about future prospects of precision electroweak measurements.

Two key ingredients for the precision measurement of the electroweak parameters are the LEP energy calibration and the luminosity measurement. Therefore, Appendix A is devoted to the description of the energy calibration, and Appendix B gives a summary of the luminosity measurement at L3.

At the time of writing this thesis, LEP has entered its second phase and is running at $\sqrt{s} \geq 2M_W$. New results on electroweak physics from the high energy runs are summarized in Appendix C.

Appendix D is devoted to a review of theoretical calculations on Bhabha Scattering expressed through Monte Carlo simulations and analytical calculations.

Chapter 2

Bhabha Scattering in the Standard Model

In this chapter, I present an overview of the theoretical framework, and recall the main features of the Standard Model (SM) electroweak theory that are relevant for this thesis.

2.1 Standard Model of Electroweak Interactions

The Standard Model of electroweak interactions was developed by S. L. Glashow, A. Salam and S. Weinberg [1]. The successful unification of electromagnetic and weak interaction by the Standard Model is a great physics achievement in this century, that can be compared to the development of Maxwell's equations which provided a unified description of the electric and magnetic fields in the last century.

The development of the unification of electromagnetic and weak interactions has its beginning in the search for a weak interaction theory. Although the electromagnetic interaction has been very well understood through QED, the knowledge of the weak interaction was very limited in the beginning. In 1932, Fermi [2] made a first attempt to formulate a theory to explain nuclear β decay. Inspired by the structure of the electromagnetic interaction, Fermi described the charged weak interactions as the interactions of two vector currents. After the discovery of parity violation in 1956, amazingly the only essential change required in Fermi's original proposal was the replacement of the vector current form with a V-A current form proposed by Feynman

and Gell-Mann [3]. The V-A theory proved to be very successful and was able to explain all the available data at low energy. But the theory is not complete since it violates the unitary limit at high energy.

The first step towards a solution in this problem came from C. N. Yang and R. Mills [4], who in 1954 developed a theory of massless interacting vector particles. The theory could accommodate particles like the photon, W^+ and W^- that would interact with each other, but it required them to be massless. Since the weak interactions are of short range, their carriers $W^{\pm}$ should be massive. For this reason, the massless Yang-Mills theory didn't gain enough attention at the beginning.

An important advance was made by Peter Higgs who developed a mechanism (*Higgs mechanism*) [5] which could make the massless gauge bosons massive without violating gauge invariance. This *Higgs mechanism* was a key ingredient in the final model.

Another key ingredient of the SM is the recognition of the $SU(2)_L \otimes U(1)_Y$ gauge symmetry of the electroweak interaction. The familiar U(1) gauge symmetry is exploited by QED to describe the electromagnetic interaction. The SU(2) gauge symmetry was first introduced to understand the strong isospin symmetry in the nuclear interaction, where

$$N = \begin{pmatrix} p \\ n \end{pmatrix}$$

is an SU(2) doublet and p, n stand for the proton and the neutron. A pattern of $\overline{e}_L \gamma^\mu \nu_L$ or $\overline{u}_L \gamma^\mu d_L$ in the weak interaction has suggested strongly the SU(2) gauge symmetry.

The final SM theory is a Yang-Mills theory with $SU(2)_L \otimes U(1)_Y$ gauge invariance, whose gauge bosons acquire their masses through the *Higgs mechanism*.

Table 2.1 shows the elementary particles and fields in the electroweak sector of the SM. The left-handed fermions are grouped as $SU(2)_L$ doublets while the right-handed

Generations:	1	2	3	T_3	Y	Q
Leptons	$\begin{pmatrix}\nu_e\\ e\end{pmatrix}_L$	$\begin{pmatrix}\nu_\mu\\ \mu\end{pmatrix}_L$	$\begin{pmatrix}\nu_\tau\\ \tau\end{pmatrix}_L$	1/2 −1/2	−1 −1	0 −1
	e_R	μ_R	τ_R	0	-2	-1
Quarks	$\begin{pmatrix}u\\ d\end{pmatrix}_L$	$\begin{pmatrix}c\\ s\end{pmatrix}_L$	$\begin{pmatrix}t\\ b\end{pmatrix}_L$	1/2 −1/2	1/3 1/3	2/3 −1/3
	u_R	c_R	t_R	0	4/3	2/3
	d_R	s_R	b_R	0	−2/3	−1/3
Gauge Bosons	γ			0	0	0
	Z			0	0	0
	W^+			1	0	1
	W^-			−1	0	−1
Higgs	$\overline{\Phi} = \begin{pmatrix}\phi^+\\ \phi^0\end{pmatrix}$			1/2 −1/2	1 1	1 0

Table 2.1: Particles and associated fields in the SM model of electroweak theory.

fermions are $SU(2)_L$ singlets. The fermions carry the quantum numbers of the weak isospin T, with its third component T_3, and the hyperchange Y. The electric charge Q is related to the electroweak quantum numbers by

$$Q = T_3 + \frac{1}{2}Y\,.$$

Besides the familiar photon (γ) with its electromagnetic interaction, a neutral gauge boson (Z) is introduced as the carrier of a new weak neutral current, and two charged gauge bosons ($W^{\pm}$) are introduced as the carriers of the known weak charged current. The *Higgs mechanism* is invoked to give masses to the $W^{\pm}$ and Z while keeping the photon massless.

With the proof of the renormalizability of the SM from G.t'Hooft [6], the problem of the violation of unitary limit at high energy for the V-A theory is overcome. The

Fermi theory, now equivalent to the exchange of only charged weak bosons $W^{\pm}$, survives as the low energy description of the charged weak interactions.

In the following sections, the construction of the electroweak theory of the SM is presented.

2.1.1 Massless Yang-Mills Theory

The construction of the SM starts with an introduction of a gauge-covariant derivative $\mathcal{D}_\mu$ to ensure the gauge invariance of the Lagrangian:

$$\begin{aligned} \mathcal{L} = \overline{\psi}\,(i\,\gamma^\mu \partial_\mu)\,\psi \quad &\rightarrow \quad \overline{\psi}\,(i\,\gamma^\mu \mathcal{D}_\mu)\,\psi \\ \partial_\mu \quad &\rightarrow \quad \mathcal{D}_\mu = \partial_\mu + i\,g_1\,\frac{1}{2}\,B_\mu \cdot Y + i\,g_2\,\vec{W}_\mu \cdot \vec{T}\,, \end{aligned} \tag{2.1}$$

where g_1 and g_2 are the coupling constants to the $\mathrm{U(1)_Y}$ and the $\mathrm{SU(2)_L}$ parts of the gauge group respectively. The factor of $1/2$ in the second term is a convention.

The massless Yang-Mills fields are the B, an isosinglet and $\vec{W}_\mu$, a triplet of the SU(2) symmetry. The fields

$$W^{\pm} \;=\; \frac{W_1 \mp i\;W_2}{\sqrt{2}} \tag{2.2}$$

describe the charged bosons $\mathrm{W}^{\pm}$ which mediate the charged weak interactions.

The two neutral fields W^0 and B from SU(2) and U(1) respectively are mixed through the electroweak mixing angle θ_w to produce the physical particles, namely the photon (represented as A) that carries the electromagnetic field, and the Z boson, that carries the weak neutral current:

$$Z_\mu \;=\; \cos\theta_\mathrm{W}\,W^3_\mu - \sin\theta_\mathrm{W}\,B_\mu \tag{2.3}$$

$$A_\mu \;=\; \sin\theta_\mathrm{W}\,W^3_\mu + \cos\theta_\mathrm{W}\,B_\mu\,. \tag{2.4}$$

The group coupling constants g_1, g_2 and the familiar coupling constant of the electromagnetic interaction e are constrained through the mixing angle:

$$g_1 \cos\theta_{\rm W} \; = g_2 \sin\theta_{\rm W} \; = e\,. \tag{2.5}$$

With the essence of Fermi's view of an interaction as a current-current interaction, the interaction part of the Lagrangian 2.2 can be explicitly written in the form:

$$-\mathcal{L}_{int} = J^{\mu}_{em}\, A_{\mu} + J^{\mu}_{NC}\, Z_{\mu} + J^{\pm\mu}_{CC}\, W^{\pm}_{\mu}, \tag{2.6}$$

where the currents are:

$$J^{\mu}_{em} = e\,\overline{\psi}\,\gamma^{\mu}\psi \tag{2.7}$$

$$J^{\pm\mu}_{CC} = g_2\,\overline{\psi}_L\,\gamma^{\mu}T^{\pm}\psi_L$$

$$= g_2\,\overline{\psi}_L\,\gamma^{\mu}\,(1-\gamma_5)\,\psi_L \tag{2.8}$$

$$J^{\mu}_{NC} = \frac{g_2}{2\cos\theta_{\rm W}}\overline{\psi}\gamma^{\mu}(g_V - g_A\gamma_5)\psi. \tag{2.9}$$

The structure of the electromagnetic current J^{μ}_{em} is of a pure vector type; while the weak charged current $J^{\pm\mu}_{CC}$ is a familiar V-A pattern. The structure of the neutral weak current J^{μ}_{NC} can be recognized as a mixture of vector and axial vector currents with the couplings $g_{\rm V}$ and $g_{\rm A}$ as follows:

$$g_V = T_3 - 2\,Q\sin^2\theta_{\rm W} \tag{2.10}$$

$$g_A = T_3\,. \tag{2.11}$$

To summarize, the electroweak theory described by the Lagrangian 2.6 has successfully incorporated the electromagnetic and weak interaction, and it predicts the existence of the weak neutral current and the $\rm W^{\pm}$, Z bosons. But the theory at this

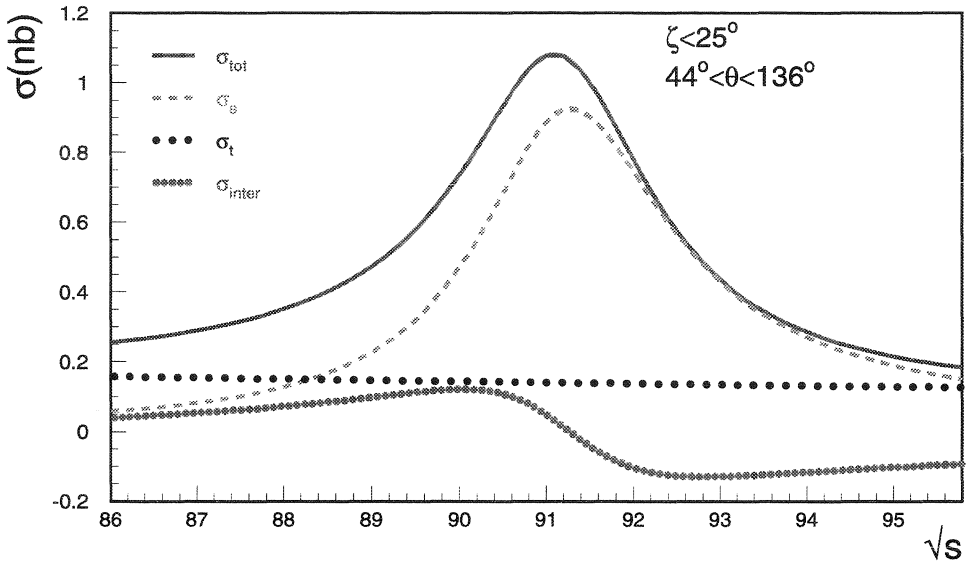

Figure 2.3: Cross section of Bhabha scattering as a function of $\sqrt{s}$.

L3 is $44° < \theta < 136°$, which is referred to as *large angle Bhabha scattering.*

To extract the s-channel information for e^+e^- final states and to compare it with the productions of other fermion pairs, a procedure generally called "t-channel subtraction" is commonly adopted. This is discussed in detail in the Section 6.1.1.

In Figure 2.3 and Figure 2.4, the large angle Bhabha scattering cross section σ and forward-backward asymmetry A_{FB} are shown as a function of $\sqrt{s}$.

Since only the s-channel is relevant to the Z physics study, the following discussion is focused on the s-channel contribution. Formulas are given for more general $e^+e^- \rightarrow f\bar{f}$ reactions, where a simple substitution $e = f$ will provide the corresponding formulas for the e^+e^- s-channel.

Cross Section

The total s-channel cross section for $e^+e^- \rightarrow f\bar{f}$ is shown in Eq. 2.26. We recognize that the first two terms correspond to the photon exchange and the $\gamma - Z$ interference terms respectively; both of them contribute very little at $\sqrt{s} \approx M_Z$. The third term,

the Z-exchange term, has a familiar Briet-Weigner resonance shape, thus the name of line shape. We further recognize the important role of the Bhabha channel from Eq. 2.26 and the fact that the coupling constants $g_{\rm V}^e, g_{\rm A}^e$ appear in the cross sections for every fermion channel.

$$\begin{aligned}\sigma_0(s) &= \frac{4\pi\alpha^2}{3s} N_c^f \{Q_e^2 Q_f^2 \\ &\quad -2\, Q_e Q_f g_{\rm V}^e g_{\rm V}^f Re\chi(s) \\ &\quad +|\chi(s)|^2[(g_{\rm V}^e)^2+(g_{\rm A}^e)^2][(g_{\rm V}^f)^2+(g_{\rm A}^f)^2]\}, \end{aligned} \tag{2.26}$$

where the color factor N_c^f is 1 for leptons and 3 for quarks.

The cross section on the Z peak, $\sqrt{s} = {\rm M_Z}$, is:

$$\sigma_0({\rm M_Z}) = \frac{12\pi}{{\rm M_Z}^2}\frac{\Gamma_{\rm e}\Gamma_{\rm f}}{\Gamma_{\rm Z}^2} \tag{2.27}$$

$$\propto [(g_{\rm V}^e)^2+(g_{\rm A}^e)^2][(g_{\rm V}^f)^2+(g_{\rm A}^f)^2]. \tag{2.28}$$

From the cross section measurement, basic Z parameters such as the mass $\rm M_Z$, the total width $\Gamma_{\rm Z}$ and the partial width $\Gamma_{\rm f}$ for $\rm Z \to f\bar{f}$, can be determined (Chapter 6).

Forward-Backward Asymmetry

The forward-backward asymmetry is defined as:

$$A_{\rm FB} = \frac{\sigma_{\rm F}-\sigma_{\rm B}}{\sigma_{\rm F}+\sigma_{\rm B}}, \tag{2.29}$$

where

$$\sigma_{\rm F} = 2\pi\int_0^1 d(cos\theta)\frac{d\sigma}{d\Omega}, \qquad \sigma_{\rm B} = 2\pi\int_{-1}^0 d(cos\theta)\frac{d\sigma}{d\Omega}. \tag{2.30}$$

Neglecting terms of the order of $(\Gamma_{\rm Z}/{\rm M_Z})^2$, the asymmetry can be approximated

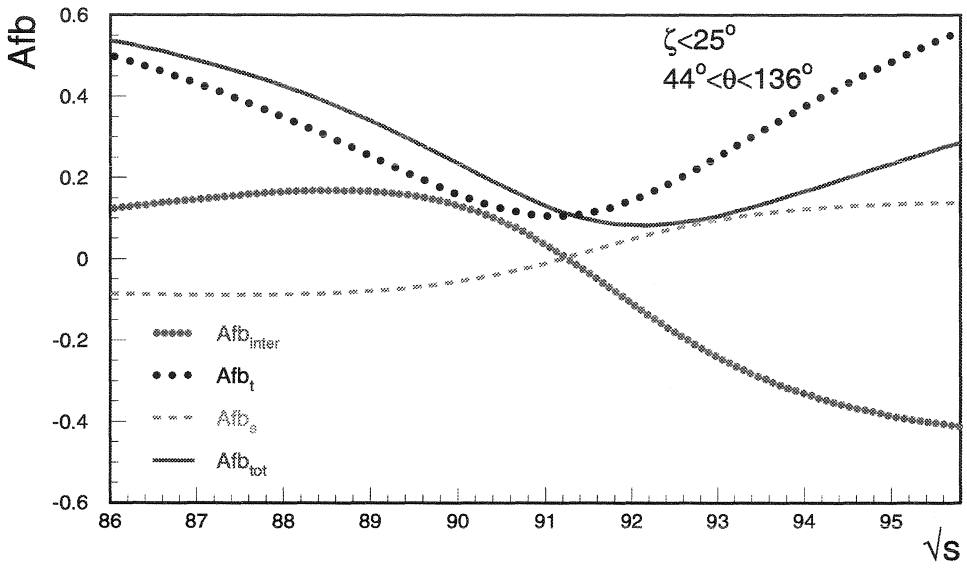

Figure 2.4: Forward-backward asymmetry of Bhabha scattering as a function of $\sqrt{s}$.

as:

$$A_{\rm FB}(s) = \frac{3}{8}\frac{-4\,Q_f g_{\rm A}^e g_{\rm A}^f Re\chi(s) + 8 g_{\rm A}^e g_{\rm V}^e g_{\rm A}^f g_{\rm V}^f |\chi(s)|^2}{Q_f^2 - 2\,Q_f g_{\rm V}^2 g_{\rm V}^f Re\chi(s) + [(g_{\rm V}^e)^2 + (g_{\rm A}^e)^2]\,[(g_{\rm V}^f)^2 + (g_{\rm A}^f)^2]|\chi(s)|^2}. \quad (2.31)$$

The asymmetry on the Z peak, ($\sqrt{s} = {\rm M_Z}$), is:

$$A_{\rm FB}({\rm M_Z}^2) \approx 3\frac{g_{\rm V}^e g_{\rm A}^e}{(g_{\rm V}^e)^2 + (g_{\rm A}^e)^2}\frac{g_{\rm V}^f g_{\rm A}^f}{(g_{\rm V}^f)^2 + (g_{\rm A}^f)^2}. \quad (2.32)$$

The absolute value of the neutral current electroweak couplings $g_{\rm V}$ and $g_{\rm A}$ can be determined from a combination of the peak cross section (Eq. 2.28) measurement which depends on $(g_{\rm V}^2 + g_{\rm A}^2)$, and the peak asymmetry measurement (Eq. 2.32) which is a function of $(g_{\rm V} g_{\rm A})/(g_{\rm V}^2 + g_{\rm A}^2)$.

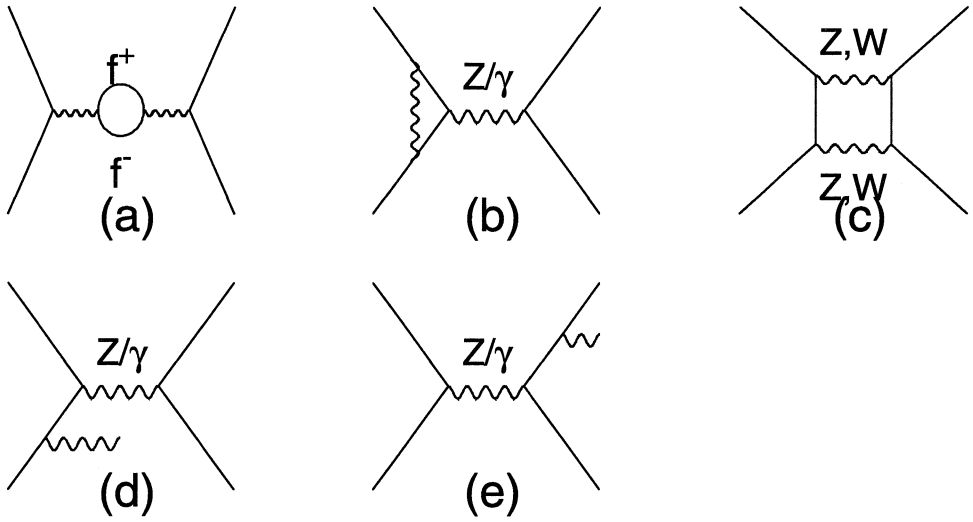

Figure 2.5: Radiative corrections.

2.2.2 Radiative Corrections

To compare with the experimental measurements, the lowest order (Born Approximation) theoretical calculations are not always adequate. Higher order diagrams need to be included to match the precision of the data. These high order corrections are usually called *Radiative Corrections.*

Radiative corrections can be separated into virtual electroweak corrections and QED bremsstrahlug corrections. Typical virtual electroweak corrections are illustrated in the top row of Figure 2.5. QED bremsstrahlug corrections are those with additional photon lines added to the Born diagrams as shown in bottom row of Figure 2.5.

The virtual electroweak corrections and the QED bremsstrahlug corrections are treated separately due to their different features:

- Virtual electroweak corrections are independent of the experimental setup, but they are dependent on the inner structure of theory. Therefore, the virtual electroweak corrections are sensitive to the mass of the top and the Higgs and

to new physics.

- QED bremsstrahlug corrections, theoretically, are not of great interest, but, practically, are very important. Their effects depend on the actual experimental setup and need to be calculated by Monte Carlo simulations of the specific detector and selection procedure. The existence of the additional photon changes the kinematics and the phase space of the reaction, and thus the calculations are much more complicated.

In the following sections, the implementation of radiative corrections is explained. More details may be found in the literature [14, 15].

Virtual Electroweak Radiative Correction

As shown in Figure 2.6, virtual electroweak corrections have three main sources : propagator corrections, vertex corrections and box diagram corrections.

To incorporate the propagator corrections, an s-dependent width is introduced:

$$\Gamma_Z \rightarrow \Gamma_Z\,(s) = \frac{s}{{M_Z}^2}\Gamma_Z. \tag{2.33}$$

The photon vacuum polarization leads to the running of the electromagnetic coupling constant α:

$$\alpha\,(s) = \frac{\alpha}{1-\Delta\alpha}. \tag{2.34}$$

The main uncertainty on $\Delta\alpha$ is the hadronic part of the photon vacuum polarization. This is a non-negligible uncertainty in the Z parameter determinations (Chapter 6).

Vertex corrections can be accounted for with the introduction of *effective couplings*:

$$\begin{aligned} g_A^f &\rightarrow \overline{g}_A^f = g_A^f\sqrt{\overline{\rho}^f} \\ g_V^f &\rightarrow \overline{g}_V^f = g_A^f\sqrt{\overline{\rho}^f}(1-4\,|Q_f|\sin^2\overline{\theta}_W) \end{aligned}$$

$$\sin^2\theta_W \rightarrow \sin^2\overline{\theta}_W = (1 + \frac{\cos^2\theta_W}{\sin^2\theta_W}\overline{\rho}^f + \ldots)\sin^2\theta_W. \quad (2.35)$$

Although the effective couplings are in principle dependent on the fermion species f, at the present experimental accuracy they can be taken as equal for a given electric charge Q_f, except for the b quark. Due to the large mass difference between the top quark and the b quark, the vertex corrections to the effective couplings are large. This also makes $\sin^2\overline{\theta}_W$ a useful variable which can be obtained from different $Z \rightarrow f\overline{f}$ ($f \neq b$) decay channels and can be compared with each other.

Box diagram corrections at LEP are relatively small, $< 0.02\%$ at $\sqrt{s} = M_Z$, due to the large suppression of the Z resonance.

With the prescription given in Eqs. 2.33, 2.34, 2.35, most of the electroweak radiative corrections can be absorbed in the lowest-order Born approximation formulas by replacing a variable with its corresponding effective variable. This prescription [15] is generally called the *Improved Born Approximation.*

Two useful parameters that play important roles in the electroweak radiative corrections are ρ and Δr [16]. The ρ parameter is defined in Section 2.1.2 and is unity to lowest order. The deviation from unity is defined as $\Delta\rho$:

$$\overline{\rho} = 1 + \Delta\rho. \quad (2.36)$$

The Δr parameter enters through the relation between M_W and G_F:

$$\frac{G_F}{2} = \frac{\pi\alpha}{2}\frac{1}{M_W{}^2\sin^2\theta_W}\frac{1}{1-\Delta r}. \quad (2.37)$$

Δr is zero to the lowest order. It can be further split into the QED correction due to the running of the QED coupling $\Delta\alpha$ and the pure weak corrections Δr_w which are sensitive to the mass of the top quark M_t and the mass of the Higgs boson M_H. The

leading contributions are:

$$\Delta\rho_t = \frac{3G_F}{8\pi^2\sqrt{2}}\mathrm{M_t}^2 + \ldots, \tag{2.38}$$

and

$$\Delta\rho_{Higgs} = \frac{3\sqrt{2}\,G_F\mathrm{M_W}^2}{16\pi^2}\frac{\sin^2\theta_\mathrm{W}}{\cos^2\theta_\mathrm{W}}(\ln\frac{\mathrm{M_H}^2}{\mathrm{M_W}^2} - \frac{5}{6}), \tag{2.39}$$

where

$$\Delta\mathrm{r}_w = \frac{\cos^2\theta_\mathrm{W}}{\sin^2\theta_\mathrm{W}}\Delta\rho. \tag{2.40}$$

The fact that the effect of the top quark mass on the radiative corrections is large (Eq. 2.38) has been used to constrain the top mass from the precision measurements at LEP. The result from this indirect measurement has been compared with the direct measurement. It provides a powerful test of the SM. The SM prediction for the Higgs mass using the current data still has large errors, because of the logarithmic dependence on $\mathrm{M_H}$ in Equation 2.39.

QED Bremsstrahlug Radiative Correction

QED bremsstrahlug radiation corrections arise from initial state radiation, final state radiation and the interference between initial and final state radiation.

The main contribution comes from initial state radiation. This can been explained by the rapid change of cross sections near the Z resonance. When an initial state radiated photon takes away some energy, the fermion pair production effectively takes place at a lower $\sqrt{s}$, with a different cross section (and asymmetry). The result can be written in the form:

$$\sigma\ (s) = \int_{\frac{4m_f^2}{s}}^{1} dz\, G(z)\, \sigma_{IB}(sz), \tag{2.41}$$

where the cross section with improved Born approximation is denoted as σ_{IB}. $s' = sz$ is the invariant mass of the produced $\mathrm{f\bar{f}}$ pair.

$G(z)$ is usually called the *Radiator Function.* In general, $G(z)$ has the following form:

$$G(z) = \delta\ (1 - z) + (\frac{\alpha}{\pi})^n \sum_{i=0}^{n} a_{ni} L^i, \tag{2.42}$$

where L is the usual logarithm of the type $L = \log \frac{s}{m_e^2}$ which has the value ≈ 24 at the Z resonance. Details on the coefficient a_{ni} can be found in Ref. [15].

The final state radiation gives an overall multiplicative factor $(1 + \delta_{QED})$, where

$$\delta_{QED} = \frac{3\alpha}{4\pi} Q_f^2 \tag{2.43}$$

which is smaller than 0.17%.

Since the total width Γ_Z is large ($\approx$ 2.5 GeV), the effect of interference between the initial and final state radiation in the Z resonance region is negligible.

To summarize, Figure 2.6 shows the effect of radiative corrections on the cross section and forward-backward asymmetry of $e^+e^- \rightarrow e^+e^-(n\gamma)$.

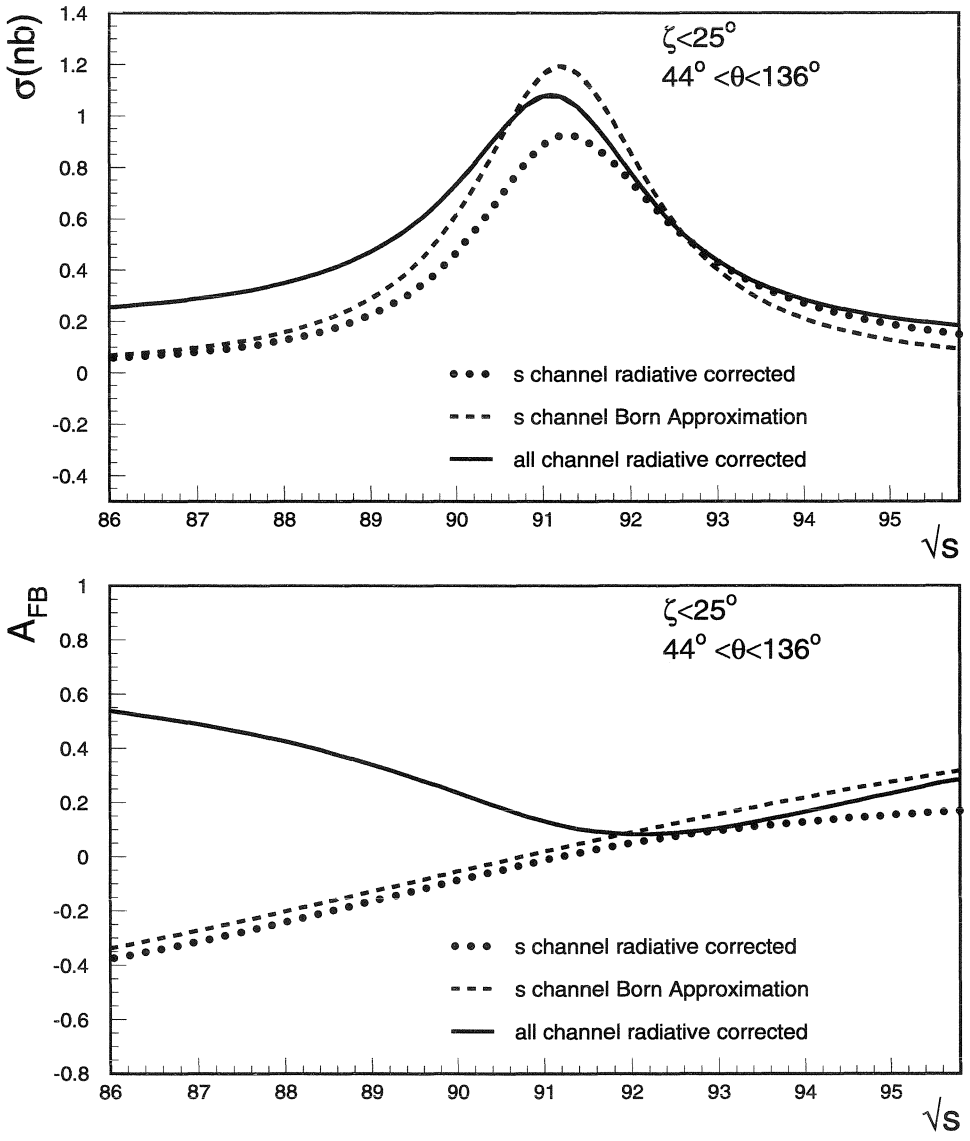

Figure 2.6: Effects of radiative corrections on cross section and forward-backward asymmetry of Bhabha scattering.

Chapter 3

The L3 Detector at LEP

This chapter is devoted to the description of the experimental apparatus used for the study in this thesis. After a brief introduction to the LEP collider facility, the components of the L3 detector are presented with emphasis on its electromagnetic calorimeter.

3.1 The LEP Collider

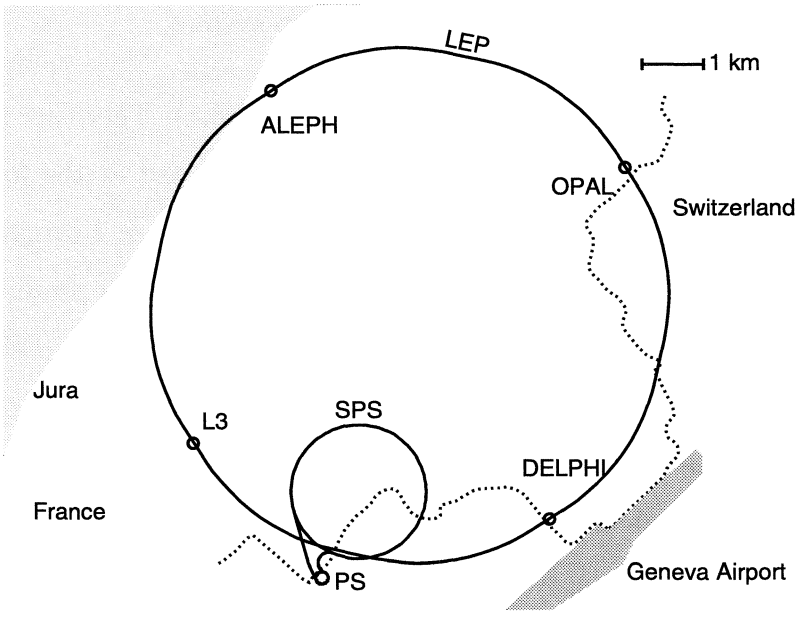

Figure 3.1: The LEP collider at CERN.

The Large Electron Positron collider LEP [17, 18], operated by CERN, is situated in a tunnel of 27 km circumference, roughly 50 to 150 meters underground at the

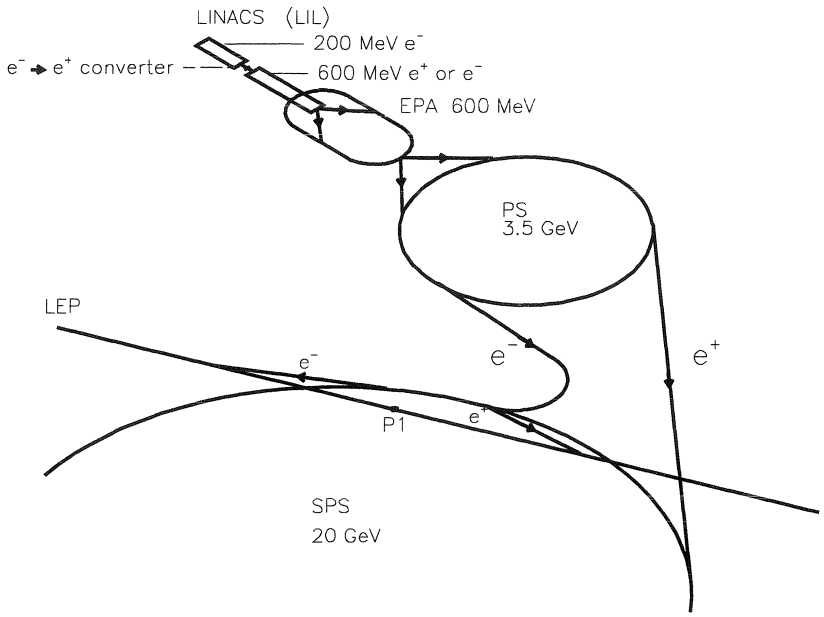

Figure 3.2: LEP injection system.

border of France and Switzerland near Geneva (Figure 3.1). There are four detectors, ALEPH [19], DELPHI [20], L3 [21] and OPAL [22], located at the four interaction points. The physics plan of LEP has two phases. The phase I program, known as *LEP1* (1989 to Oct. 1995), has been finished successfully with a production of about 15 million Z bosons. Since 1996, LEP has entered its second phase *LEP2* with beam energies above the threshold of W^+W^- pair production.

Figure 3.2 shows the stages of the LEP injection system. The first stage is known as LIL (LEP Injecteur Linéaire). One linear accelerator (LINAC) shoots 200 MeV electrons on a tungsten target to produce positrons via photon conversion. A second LINAC accelerates the positrons together with electrons to 600 MeV. The electrons and the positrons are then injected into the electron-positron accumulation ring (EPA), which condenses the beams in phase space through synchrotron radiation damping. The modified proton synchrotron (PS) receives the electrons and

the positrons from the EPA and accelerates them to 3.5 GeV. The pre-acceleration chain is completed by the super proton synchrotron (SPS) which boosts the electrons and the positrons to 20 GeV to be ready for filling the LEP ring. A typical injection current per bunch is 0.8 mA.

The LEP ring is the last part in the whole chain of accelerators. It serves both as a storage ring for the electron and positron bunches and as an accelerator which ramps the electron and positron bunches from the injection energy (20 GeV) to the collision energy ($\approx$ 45.5 GeV at LEP1). The whole ring is divided into eight bending sections and eight straight sections. The eight bending sections, with a length of 2840 m each, consist of 3304 dipole magnets which force the beam into its orbit. At 45 GeV, the required magnetic field is 0.048 Tesla. Four out of the eight straight sections house the four experiments. On both sides of each experiment, superconducting quadrupole magnets are installed to focus the beams at the interaction point and to optimize the luminosities. Two of the straight sections (near the L3 and OPAL sites) contain 120 copper RF cavities that accelerate the beam from injection energy to collision energy and compensate the energy losses due to the synchrotron radiation. The beam lifetime is about 20 hours after ramping to the collision energy.

The rate of collisions is determined by the luminosity, and is proportional to the number of bunches up to a current limit where inter-bunch effects within a single beam become important. During 1989-1991, LEP was operated with four electron bunches colliding with four positron bunches (Pretzel scheme [23, 24]). To increase the luminosity, the number of bunches were increased to eight during the running of 1992-1994. A typical instantaneous luminosity delivered to the experiments was $1.5 \times 10^{31}\mathrm{cm}^{-2}\mathrm{s}^{-1}$ in 1994. Since 1995, LEP has switched to bunch train mode [25, 26] in order to obtain higher luminosity.

Figure 3.3 shows the history of the luminosity recorded by the L3 detector at LEP1. In 1991, a scan of the Z resonance was performed with about 60% of the

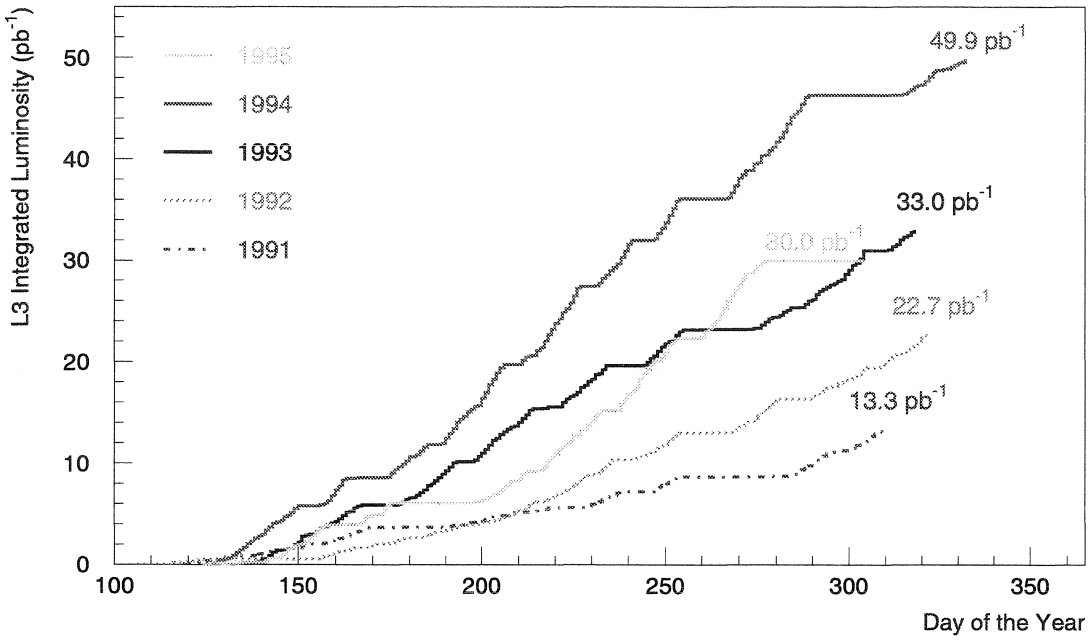

Figure 3.3: Integrated luminosity recorded by the L3 detector each year at LEP 1.

luminosities taken on the peak and the rest at six energy points approximately ± 1, ± 2 and ± 3 off the peak. In 1992 and 1994, data were taken on the peak. In 1993 and 1995, two scans of the Z resonance curve were performed with about half of the luminosity on the peak and another half of the luminosity at two energy points approximately ± 2 GeV off the peak. Up until October 1995, the LEP1 program successfully delivered a total luminosity of 4×150 pb^{-1}. The large statistics of the data has enabled a determination of the electroweak parameters with unprecedented precision.

In November 1995, LEP took a pilot run, referred to as LEP1.5, with $\sqrt{s} = 130 - 140$ GeV and an integrated luminosity of 5 pb^{-1}. In 1996, LEP entered its second phase LEP2, running at energies above the W^+W^- pair production threshold: $\sqrt{s} \approx 161$ GeV with 11 pb^{-1} and $\sqrt{s} \approx 172$ GeV with 10 pb^{-1}. The electroweak physics results from these high energy runs are summarized in Appendix C.

The energy calibration of the LEP beam energy, which is one of the key issues in the precision measurement of the Z parameters, is presented in Appendix B.

3.2 The L3 Detector

The L3 detector shown in Figure 3.4 and Figure 3.5 is designed to study e^+e^- collisions up to 200 GeV with emphasis on high resolution energy measurements of electrons, photons and muons. The e^+ and e^- beams collide in the center of the detector. Viewed from the interaction point towards the outside, the L3 detector consists of the following subdetectors:

- Microvertex Detector
- Central Tracking Detector
- Electromagnetic Calorimeter
- Scintillation Counters
- Hadron Calorimeter
- Muon Chambers.

The whole L3 detector is installed inside a 7800 ton magnet which provides a 0.5 Tesla field along the beam axis. The detectors are supported by a 32 m long, 4.45 m diameter steel tube which is concentric with the LEP beam line. The muon spectrometer is located outside the support tube and separated from the other subsystems. The two luminosity monitors are located at $z = \pm\ 2.65\ m$ from the interaction point where the z direction is defined as the direction of the LEP e^- beam. In the following, the status of the L3 detector is presented.

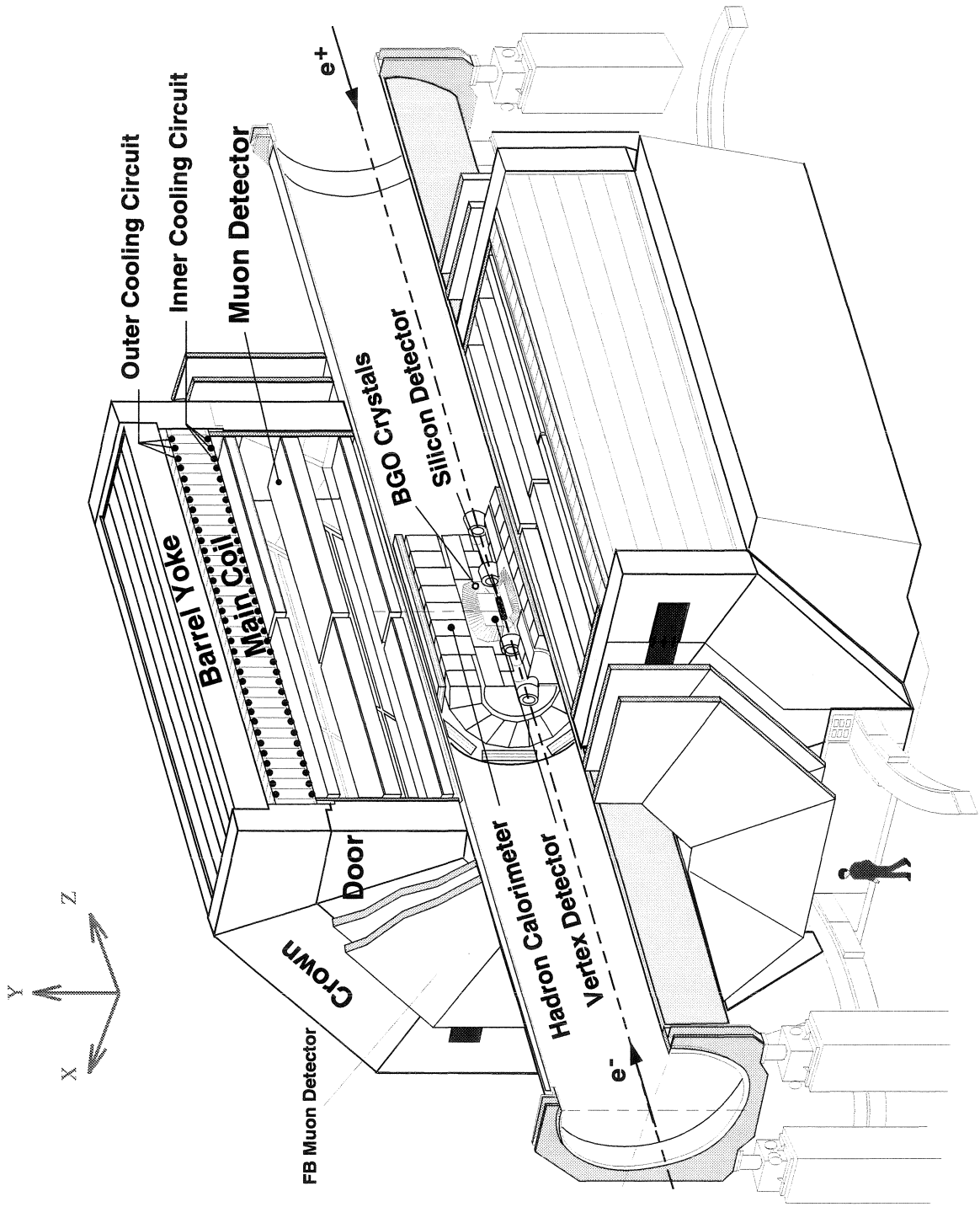

Figure 3.4: Perspective view of the L3 detector. The L3 coordinate system is represented by the axes in the top left corner.

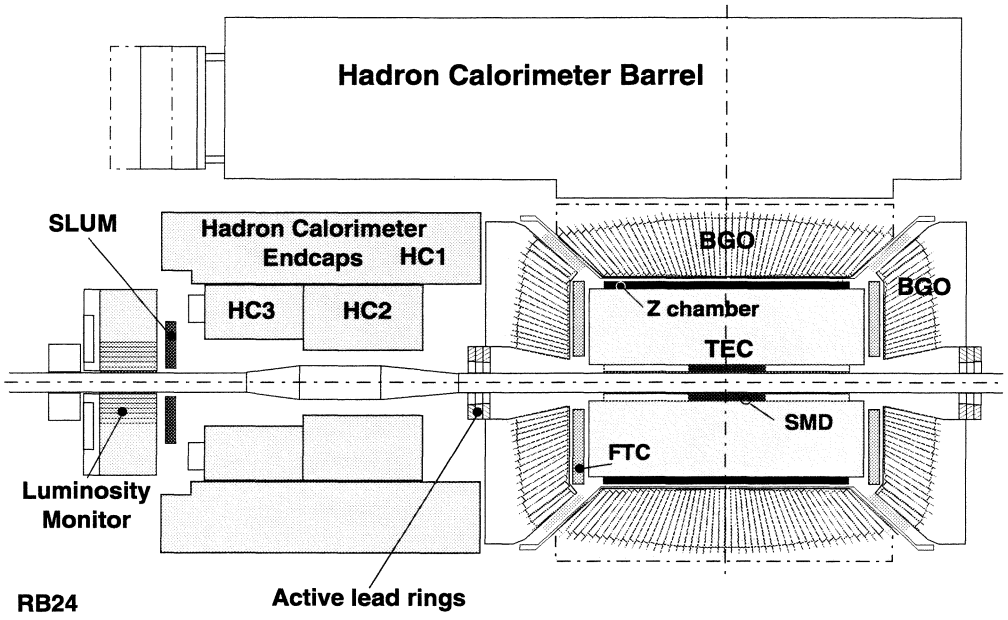

Figure 3.5: Side view of the inner structure of the L3 detector.

3.2.1 Microvertex Detector

In 1991, the radius of the LEP beam pipe at its four interaction points was reduced from 8.0 cm to 5.5 cm. This presented L3 with an opportunity to design and install a silicon microstrip detector (SMD) [27] to improve its central tracking ability.

The L3 SMD is a two-layer, double-sided silicon strip detector. It is 35.5 cm long covering the range of polar angles $29^0 - 151^0$ with two layers and down to $22^0 - 158^0$ with one layer. The SMD is arranged in 24 ladders (Figure 3.6) at radii of approximately 6 cm and 8 cm from the z axis. Each ladder is built from two separate "half ladders" which in turn are built from two electrically and mechanically joined double-sided silicon sensors. Each SMD sensor is 70 mm long, 40 mm wide and made from 300 μm thick high purity n-type silicon. On the junction side of the sensors, the strips are parallel to the beam line to provide $r - \phi$ measurements, with a readout

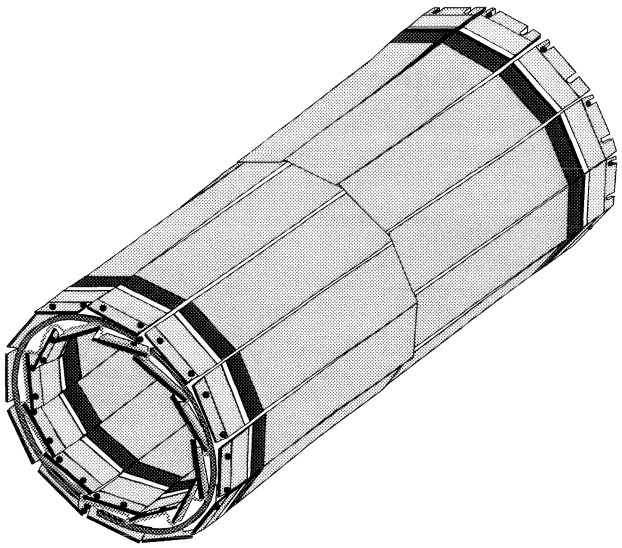

Figure 3.6: The ladder structure of the SMD.

pitch of 50 μm. On the ohmic side of the sensor, the strips are perpendicular to the beam line to provide $r - z$ measurements, where the readout pitch is 200 μm over the polar angle range $0.53 < |cos\,\theta| < 0.93$, and 150 μm over the polar angle range $|cos\,\theta| < 0.53$. The intrinsic resolutions of the SMD are 7 μm and 14 μm for the $r-\phi$ side and $r-z$ side respectively. To enhance the correlation between the detected hits on a track and to resolve ambiguities, the outer layer ladder is placed with a stereo angle of 2^0 with respect to the beam axis.

The SMD was not fully operational during 1993, the year when it was first installed, due to initial technical problems. Since 1994, the SMD has been fully functional and successfully implemented for physics analysis such as the forward-backward asymmetry measurement in this thesis (See Section 5.3).

3.2.2 Central Tracking Detector

The central tracking detector consists of a drift chamber that operates in the time expansion mode (Time-Expansion-Chamber, TEC).

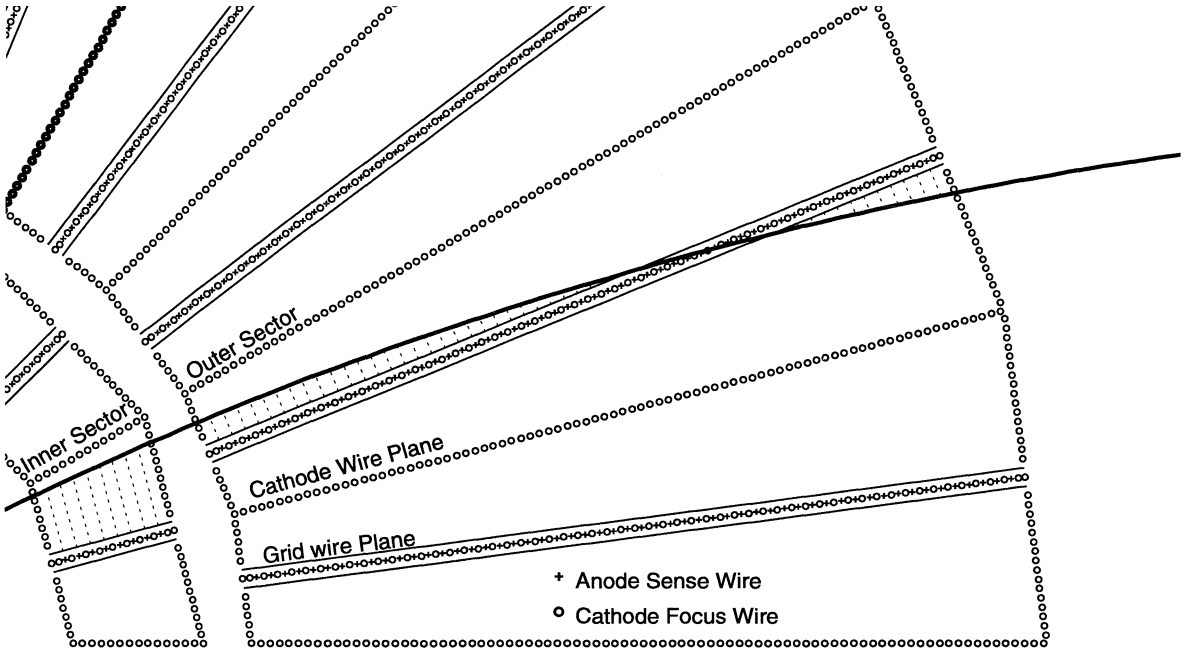

Figure 3.7: Diagrams of several drift cell of the L3 tracking detector in $r - \phi$ view.

The TEC is 900 mm in length. It has an inner radius of 86 mm and an outer radius of 457 mm, resulting in a lever arm of 317 mm radially for the track measurement. The inner and outer TEC are radially divided into 12 and 24 sectors respectively, with each inner TEC sector covering two outer sectors (Figure 3.7). There are 8 and 54 anode sense wires in one inner and outer sector respectively, among which 2 and 9 wires are charge division wires which are read out at both ends, and hence may be used to determine the $r - \phi$ coordinates and z coordinates at the same time. At each side of the sense wire plane, there is a plane of grid wires that is used to separate the low field drift region from the high field amplification region. The cathode wires are located along the sides of the sector.

The TEC is operated with a gas mixture (80% CO_2 and 20% iso-C_4H_{10}) with low longitudinal diffusion and a low drift velocity of 6 μm/ns. A single wire resolution of 50 μm is achieved. The transverse momentum resolution is given by: $\sigma(P_T) = 0.018 P_T$.

The TEC is surrounded by a "Z chamber" which consists of two cylindrical multi-wire proportional chambers with cathode strip readout and covers the outer cylinder of the TEC. The cathode strips are inclined with respect to the beam -z direction by 69^0 and 90^0 for the inner chamber, and by -69^0 and 90^0 for the outer chamber. The Z chamber supplements the $r - \phi$ measurements from the TEC with z-coordinates measurement at a resolution of 320 μm just outside TEC.

3.2.3 Electromagnetic Calorimeter

The L3 electromagnetic detector is designed to provide excellent energy and spatial resolution for photons and electrons over a wide energy range (from 100 MeV to 100 GeV). The whole calorimeter is mounted around the central tracking detector. It consists of 10734 Bismuth Germanate (BGO) crystals which are arranged into two half-barrels and two endcaps. The crystals are arranged with a pointing geometry towards the interaction point so that the calorimeter barrel and endcaps are each hermetic.

BGO Crystal

Bismuth Germanate is a high density inorganic crystal scintillator. When a high energy photon or electron is incident on the BGO crystal, it initiates an electromagnetic cascade or "shower." The processes of electron-positron pair production and bremsstrahlug radiation generate more electrons, positrons and photons with lower energy. The energy of the shower particles eventually fall below the critical energy and then dissipate the remaining energy by ionization. The ionization further creates excitations in the crystal lattice that decay by emitting scintillation photons with a wavelength spectrum peaked near 480 nm for BGO.

Convenient variables to describe the electromagnetic shower development are the *radiation length* and *Molière radius* which are intrinsic properties of the shower ma-

	$Bi_4Ge_3O_{12}$	NaI(Tl)	CsI(Tl)	$PbWO_4$
Density (g/cm^3)	7.13	3.67	4.51	8.28
Radiation length (cm)	1.12	2.59	1.86	0.89
Molière radius (cm)	2.4	4.5	3.7	2.0
Peak emission wavelength (nm)	480	410	565	420-450
Relative light yield	1	7.7	2.7	0.05
Temperature coefficient ($\%/^0C$)	-1.55	0.22	0.1	-1.9
Hygroscopic	no	very	somewhat	no
Refractive index	2.20	1.85	1.80	2.16

Table 3.1: Main properties of BGO and a few other commonly used inorganic crystal scintillator.

terial. The *radiation length*, X_0, is the longitudinal length through which an electron losses $1/e$ of its energy. The *Molière radius*, R_M, describes the lateral profile of the shower development, such that 90% of the shower is typically contained within a transverse distance of R_M from the direction of the incident particle and 99% of the shower is contained within $3R_M$.

Table 3.1 lists the main properties of BGO and a few other commonly used crystal scintillators.

Due to its high density, BGO crystal has high stopping power for photons and electrons: $X_0 = 1.12$ cm and $R_M = 2.4$ cm. This ensures the compactness of the calorimeter.

Each BGO crystal in the L3 electromagnetic calorimeter has a truncated pyramid shape with a front face $\approx 2 \times 2\,cm^2$, a rear face $\approx 3 \times 3\,cm^2$ and a length of 24 cm. Produced by the Shanghai Institute of Ceramics in China, the crystals have been cut and polished with the tolerances of -300 to 0 μm in transverse dimension and -400 to 0 μm in length. The dimensional tolerances achieved are within 100 μm.

During production, several batches of crystals were evaluated for radiation hardness. After exposure to a dose of 10^3 rad (100 times of the dose in the worst case

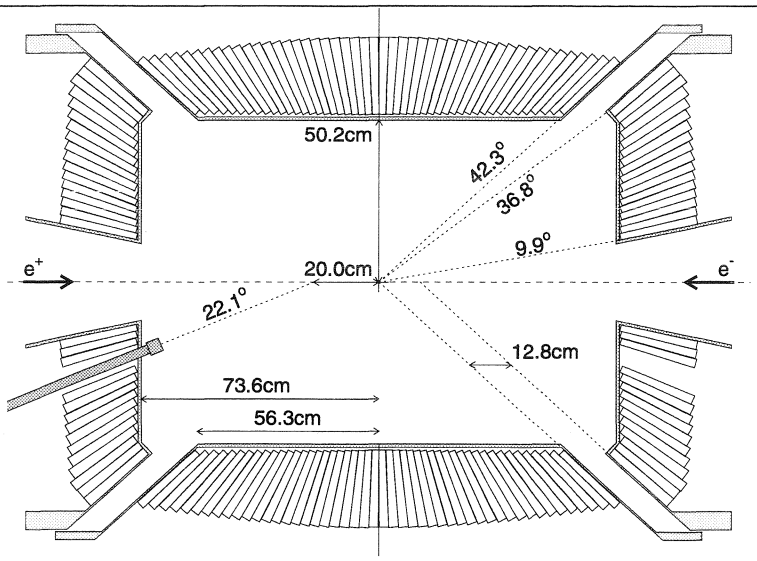

Figure 3.8: Side view of the L3 electromagnetic calorimeter.

scenario of a LEP beam accident), the light output immediately dropped by 40% and then fully recovered spontaneously at room temperature after a month. The crystals at small angles in the endcaps, produced with Europium doping, are found to have shorter recovery time.

The light collected at the rear face of a tapered crystal with its six faces polished increases strongly with the distance from the light source to the rear face. Good linearity and energy resolution require a nearly uniform light collection efficiency. By coating the crystals with a 40 to 50 μm thick layer of high reflectivity NE560 paint, one obtains uniform light collection with a tolerance of -5 to +10%.

Calorimeter Structure

The L3 electromagnetic calorimeter (Figure 3.8) consists of the following structures.

- *Two half-barrels:* Each half-barrel has 3840 crystals that are arranged into 24 rings with 1 crystal in θ and 160 crystals in ϕ in each ring. The total angular coverage is $42.3^0 < \theta < 137.7^0$.

- *Two endcaps:* The crystals in each endcap are arranged into 6 rings; from inner to outer, the numbers of crystals for each ring are: 2, 3, 3, 3, 3, 3 in θ and 48, 64, 80, 96, 112, 128 in ϕ respectively. Nine crystals are taken out from each endcap at $\phi \approx 270^0$ and $\theta(180^0 - \theta) \approx 16^0$ to leave a hole for the last section of the beam pipe for the RFQ calibration system (See Chapter 4). The total number of crystals in each endcap is 1527 and the total angular coverage is $9.9^0 < \theta, (180^0 - \theta) < 36.8^0$.

Each crystal is held in a separate cell of 200-250 μm thick carbon fiber composite wall and kept in position with pressure applied from the back by a spring-loaded screw. Cellular walls and clearances represent about 2.1% of the total solid angle coverage. To minimize the shower leakage through this dead space, each crystal is tilted in ϕ by about 10 mrad to aim at a point 5mm away from the beam line. The tilt in θ is not necessary due to the fact that the spread of the LEP beam position in z is about $\pm$2 cm relative to the nominal interaction point. The endcaps were installed at the beginning of 1991 and are located at positions displaced about $\pm$12.8 cm from their nominal positions long the z axis due to the space requirements of the central tracking detector. The configuration induces a $2.1^0 - 5.4^0$ tilt in θ of each crystal's long axis in the endcaps in respect to the nominal direction.

The overall mechanical support for each half-barrel and endcap is provided by a carbon fiber composite and acrylic foam sandwich structure consisting of a 10 mm thick cylindrical inner tube, with steps on its outer surface matching the front face of each crystal and a 5 mm thick conical shell along the length of the edge crystals. A 0.5 mm thick steel membrane reinforces the surface where the two half barrels join.

Readout Electronics

Since the BGO calorimeter is operated in a 0.5T magnetic field and space is at premium, photodiodes are used to detect the BGO scintillation light. They are insensitive

to magnetic field and have a quantum efficiency of 70% at 480 nm. Each crystal has two photodiodes, each with 1.5 cm^2 active area glued to its rear face. Operated at 15V reverse bias, the photodiode produces a signal of 0.2 fC (1200 electrons) for each MeV of energy deposition and the signal is amplified by the charge sensitive preamplifier mounted directly behind each crystal. The preamp signal is first fed through a shaping circuit and the shaped signal is sent to be digitized by a specially designed analog-to-digital converter (ADC). The digitizing range of the ADC is 21 bits, with a resolution of at least 10 bits for signals greater than 100 MeV. The linearity is better than 1% over the full range. The actual dynamic range achieved for the BGO signals is from 1 MeV to 200 GeV. The digitization takes about 220 μs and is done inside the L3 detector in order to keep the system compact and the loss of information low. 12 ADC channels are grouped into an ADC card. The ADC cards are grouped in boxes with 20 ADC cards for the barrel and 8 for the endcaps, and are mounted just outside the hadron calorimeter.

The BGO data acquisition system consists of 4 levels. Level-1 is formed by the ADC boards containing the analog front-end electronics and the single chip microcomputers that perform the digitization. The level-1 channels are organized in token ring networks of 60 (barrel), 48 (endcap) or 38 (luminosity) crystals and are read out by level-2 which is a single board Motorola 68010 in a VME crate, located more than 100 meters away in the counting room. A VME crate contains 16 level-2 modules and is controlled by a level-3 computer, the VME crate controller. There are 13 of these crates including those for the barrel, endcaps and the luminosity monitors. Each level-3 computer gets data from the level-2 over the VME crate databus and sends it to the level-4 system by a VME to VME link. The level-4 collects the data in First-In-First-Out (FIFO) memory buffers and sends it to a FASTBUS memory in the main L3 data acquisition system.

Thermal Regulation

The light response of a BGO crystal is strongly correlated to the crystal temperature with a coefficient $-1.55\%/^0C$, which makes it necessary to control and monitor the crystal temperature in order to achieve and maintain high energy resolution. The temperature control needs to dissipate the heat from preamplifier boards (0.2 W/Channel) and level 1 readout boards (2 W/Channel), and to prevent heat transfer from outside. It is realized by using brass cooling screens to which copper pipes have been soldered to carry cooling fluid.

The temperature at the front and back of the crystals is monitored by 1280 AD590 sensors. There is one front and back temperature measurement for every 12 crystals with a reading accuracy of 0.1^0C. The temperature sensor data is digitized by the level-1 module and is read out in the same way as the crystal light output data. On the basis of these data, a two-dimensional fit is performed yielding the temperature at the front and back side of each crystal. The temperature T_{max} at the location of the shower maximum x_{max} is given as:

$$T_{max} = T_{front} + x_{max} \cdot \ (T_{back} - T_{front}). \tag{3.1}$$

A temperature correction C_T is applied further for the energy reconstruction which has been normalized to the reference temperature $T_0 = 18\ ^0C$:

$$C_T = 1 + 0.0155 \cdot (T_{max} - T_0). \tag{3.2}$$

Energy Reconstruction

The energy reconstruction is performed in two steps. The first step is *Calibration* which provides the transformation from the raw ADC signal to an energy value on a crystal-by-crystal basis. The transformation takes into account the temporal effects

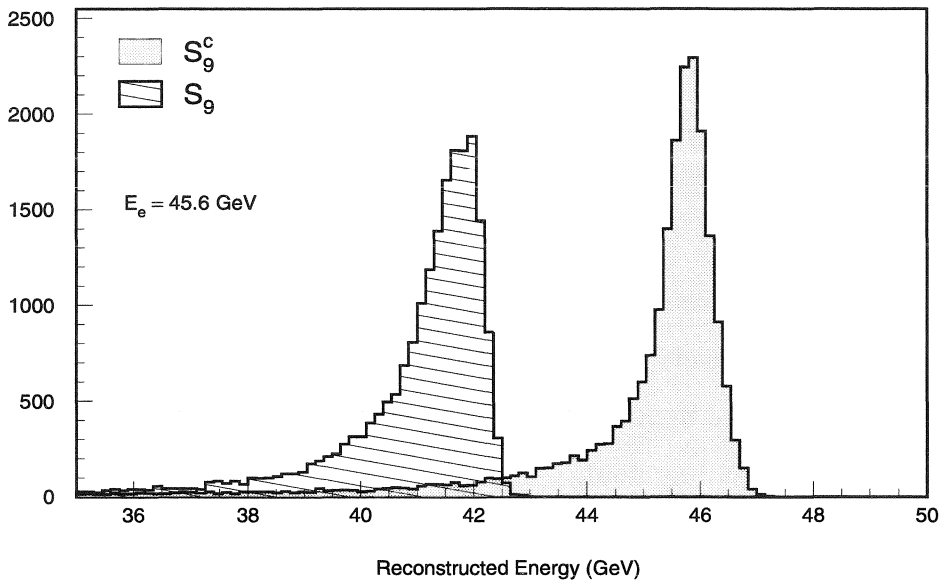

Figure 3.9: Distribution of the reconstructed energy variable S_9 and S_9^c for a 45.6 GeV Bhabha electron at the Z peak simulated in the detector.

on the crystal scintillation response due to temperature variations and intrinsic losses associated with aging and radiation damage. Since energy resolution relies strongly on the calibration precision, much effort has been put into developing precise calibration techniques. Among these, the RFQ calibration system, developed by Caltech, has succeeded in providing better than 1% calibration. A separate chapter, Chapter 4, is devoted to the discussion on calibration techniques with an emphasis on the RFQ calibration system.

The second step in the energy reconstruction is *Pattern Recognition* which identifies the basic physics objects. The algorithm applied is based on *cluster* finding and *bump* reconstruction. A cluster is an array of crystals that are geometrically connected. Each crystal in a cluster has energy greater than 10 MeV and each formed cluster has energy greater than 40 MeV. The local energy maxima in the clusters are called *bump crystals* which are required to have energy greater than 40 MeV. A *bump* is formed by assigning the non-bump crystals in the cluster according to the distance

to their nearest bump crystal. A bump is assumed to be associated with a particle that is incident on the crystals. The energy of the particle is reconstructed based on the summation of the energies over the 3 $\times$ 3 crystal matrix centered on the bump crystal, denoted as S_9. To account for the leakage from the 3 $\times$ 3 matrices, which is correlated with the ratio S_1/S_9 (S_1 is the energy of the bump crystal), a correction factor is applied to S_9 defining a *corrected sum-of-9* energy:

$$S_9^c = \frac{S_9}{c_1 \cdot S_1/S_9 + c_2}, \tag{3.3}$$

where c_1 is 0.1231 and c_2 is 0.8222 for the barrel, and $c_1 = 0.006823$ and $c_2 = 0.8582 + EC(\theta)$ for the endcap. $EC(\theta)$ is a θ-dependent correction with a typical value of 0.01. Figure 3.9 shows improvement of S_9^c over S_9, for a 45 GeV electron.

3.2.4 Scintillation Counters

The scintillation counter system is arranged between the electromagnetic and hadronic calorimeters. 30 plastic counters in the barrel part cover 93% of the azimuthal angular range and $|\cos\theta| < 0.83$ of the polar angular range. 16 plastic counters in the endcap installed in 1995 extend the polar angular coverage to $|\cos\theta| < 0.90$. The primary purpose for the scintillation counters is to provide discrimination of dimuon events from cosmic muons, by using their good time resolution (0.5 ns). A single cosmic muon passing near the interaction point resembles a muon pair event produced in an e^+e^- interaction, but the time-of-flight difference between opposite scintillation counters is 5.8 ns for cosmic muons and zero for muon pairs.

3.2.5 Hadron Calorimeter

The hadron calorimeter in L3 serves a dual purpose. Together with the BGO crystals, it measures the energy of hadrons emerging from the e^+e^- collisions. It also acts as a

filter allowing only non-showering particles to reach the precision muon spectrometer.

The L3 hadron calorimeter consists of depleted uranium (and brass) absorber plates interleaved with proportional wire chambers read out in mini-towers to provide fine transverse and longitudinal samplings. The barrel covers the central region ($35^0 < \theta < 145^0$), while the endcaps cover $5.5^0 < \theta < 35^0$ and $145^0 < \theta < 174.5^0$. The total coverage of the hadron calorimeter is 99.5% of 4π.

The hadron calorimeter has a modular structure. The barrel consists of 9 rings of 16 modules each. Each endcap consists of three separate rings and each is split vertically into half-rings, resulting in a total of 12 modules. The modularity of the endcap detectors permits their fast withdrawal to provide access to the other L3 central detector components. The wires in each module are grouped to form readout towers with $\Delta\theta = 2^0, \Delta\phi = 2^0$.

The amount of material traversed by a particle originating at the interaction point varies between 6 and 7 nuclear absorption lengths. A resolution on hadron jet energies of $\sigma/E = (55/\sqrt{E} + 5)\%$ has been obtained with the L3 hadronic calorimeter.

Muon filter

The muon filter is mounted on the inside wall of the support tube. It adds 1.03 absorption lengths to the hadron calorimeter to ensure that hadrons are fully absorbed inside the support tube. The muon filter consists of eight identical octants, each made of six 1 cm thick brass (65% Cu + 35% Zn) absorber plates, interleaved with five layers of proportional chambers, and followed by five 1.5 cm thick absorber plates matching the circular shape of the support tube.

3.2.6 Muon Chambers

The muon chamber system in L3 is designed to provide precision measurement of muons.

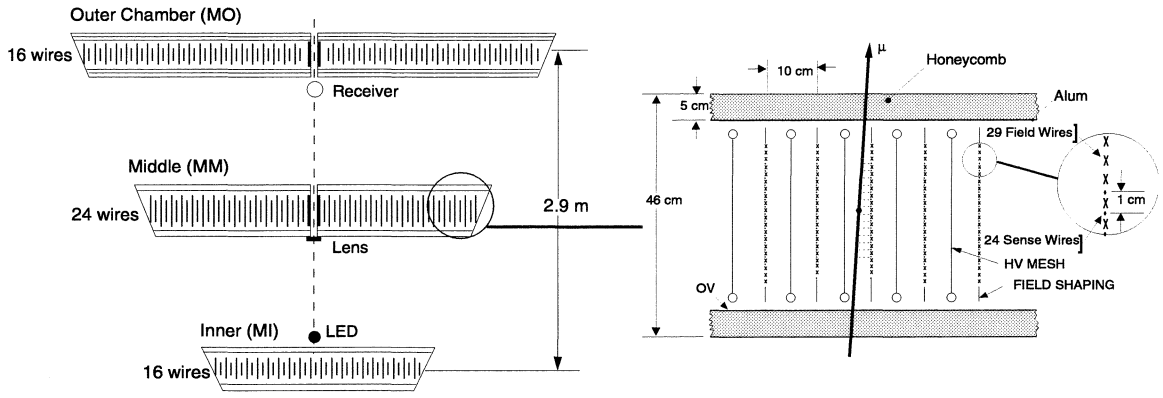

Figure 3.10: Muon chamber layout in an octant and the structure of a P chamber in the central muon spectrometer.

The barrel part of the muon chamber system consists of two "ferris wheels," each having eight octants. Each octant (Figure 3.10) has five precision (P) chambers, arranged into three layers. The outer layer (MO) and the middle layer (MM) have two chambers each, the inner layer (MI) has one chamber. There are 16, 24 and 16 signal wires in MO, MM and MI layer respectively to provide measurements of the track coordinates in the bending plane. The position of the wires is controlled by precision Pyrex glass and carbon fiber bridges. An accuracy of 10 μm in the position is achieved using a system of straightness monitors, with each monitor composed of an LED, lens and a quadrant photodiode. Since muons more energetic than 3 GeV are confined to a single octant, the internal octant alignment is critical. Several alignment systems are used to monitor and correct the chamber positions that result in a 30 μm precision:

- an opto-mechanical system using LED's for vertical alignment;
- a laser beacon using a He-Ne laser for parallel chamber alignment;

- a UV laser to simulate infinite momentum particles originating from the interaction point and passing through all three layers.

In addition, the top and bottom covers of the MI and MO chambers also consist of drift chambers which measure the z coordinate along the beam direction. In total there are 6 z-chambers per octant. Each z-chamber consists of two layers of drift cells offset by one half cell with respect to each other to resolve left-right ambiguities.

In θ, the regions $44° - 87°$ and $93° - 136°$ are covered by three layers of P-chambers, while the regions from $35° - 44°$ and $136° - 145°$ are covered only by two layers (MI and MM). In ϕ, the muon spectrometer covers about 95% of 2π due to the gaps between P-chambers and between octants. In total, about 64% of the full solid angle is covered by at least two layers of P-chambers.

The P(Z) chambers are filled with a gas mixture of 38.5% (8.5%) ethane and 61.5 % (91.5%) argon and are operated in drift mode with average drift velocity of 50 μm/ns (30 μm/ns). A typical single wire resolution is less than 200 μm for the P-chambers and 500 μm for the Z-chambers. The momentum resolution of L3 barrel muon chamber is $\sigma(P_T)/P_T \approx 2.5\%$ at 45 GeV and is in agreement with the design value.

A forward-backward (FB) muon chamber system has been designed to extend the angular coverage to $22° - 158°$ resulting in a 76% coverage of the full solid angle. Half of the FB muon chamber system was installed in the 1993-1994 shutdown period at $z < 0,\ x < 0$ and $z > 0,\ x > 0$. The remaining half was installed in the 1994-1995 shutdown period. The FB muon chamber mounted on the magnet door has three layers, each with 16 chambers filled with the same gas mixture as in the P-chamber. Each cell has 4 anode signal wires with an average resolution of 200 μm. Momentum determination in the region of $36° - 43°$ and $137° - 144°$ relies on the MI, MM layers in the central chambers and the inner layer in the FB chambers and has a resolution $\sigma(P_T)/P_T$ from 2-20% degraded with θ. The momentum measurement in the angular

regions $22° - 36°$ and $144° - 158°$ uses three layers in the FB chamber and has a resolution $\sigma(P_T)/P_T \approx 25\%$, limited by the multiple scattering due to the 1 m thick magnet door.

3.2.7 Luminosity Monitors

The integrated luminosity serves as an absolute normalization for the event rates observed in the detectors. In e^+e^- colliders, small angle Bhabha scattering is usually used to measure the luminosity (See Section 2.5 and Appendix B). In L3, the luminosity is measured with a luminosity monitor which consists of a calorimeter made of Bismuth Germanate (BGO) crystals and a silicon strip tracker (SLUM).

The BGO calorimeter consists of two detectors situated on each side of the interaction point at a distance of approximately 2730 mm. Each calorimeter is cylindrically symmetric and consists of 304 BGO crystals parallel to the beam axis. The BGO calorimeter is split into two halves vertically which can be separated during the filling of the LEP ring in order to protect the crystals from radiation damage. The movement is controlled by a hydraulic device with a position reproducibility of better than 10 μm. The performance of the BGO crystals is monitored using LEDs mounted in the front of the BGO crystals.

The SLUM (Figure 3.11) is mounted in front of each BGO calorimeter. On each side, the detector has three layers. Two layers of strips concentric with the beam axis (r wafers) to measure the θ angle of a transversing particle, and one layer of strips perpendicular to the beam axis (ϕ wafers) to measure the ϕ angle. Each layer is built out of 16 wafers. An r wafer contains 96 silicon strips of three different patches (64×0.5mm, 16×1.875mm and 16×1.0mm), and a ϕ wafer has 96 channels resulting in a total of 8192 channels for the whole detector. The wafers have very high intrinsic geometrical precision (1-2 μm) and are accurately positioned and measured with an accuracy of 6 μm.

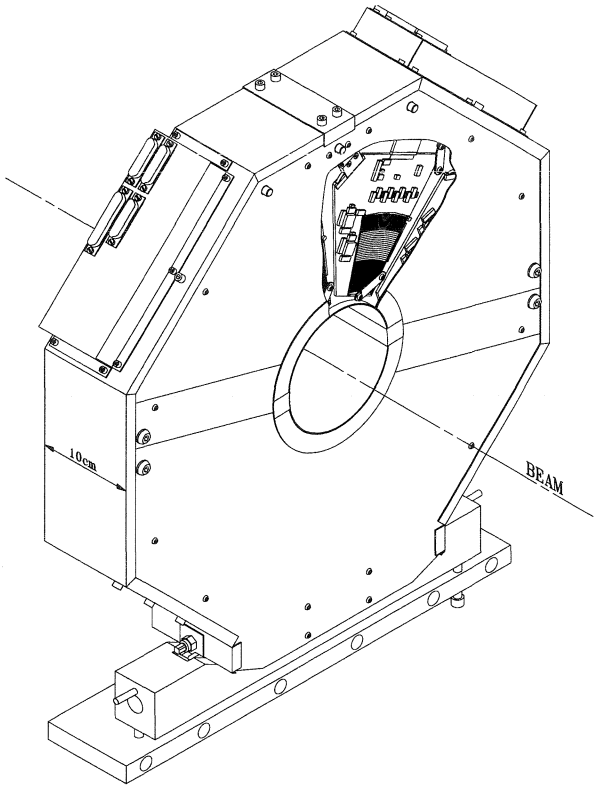

Figure 3.11: Perspective view of the silicon tracker for the luminosity monitor with a cutout showing an r wafer.

Since the silicon tracker is sensitive to individual particles, it is desirable to minimize the amount of material in front of the detector in order to reduce the amount of showering before the silicon. A specially designed beam pipe (Figure 3.5) was installed on the $+z$ side of the interaction point while for the $-z$ side, it was not possible as it would interfere with the installation jig of the L3 microvertex detector.

3.2.8 Trigger System and Data Acquisition

The primary goal for the trigger system is to record the detector signal with high redundancy and high efficiency. The L3 trigger system is a cascade of three digital

trigger levels with intermediate buffering. After each bunch crossing, all the signals in the subdetectors are read out by front end electronics. It is up to the trigger system to decide before the next bunch crossing, *i.e.*, within 11 μs (8 bunch mode), whether it is an interaction of physics interest or a background event such as a beam particle scattering from the molecule of the residual gas in the beam pipe or cosmic rays or electronic noises. The events of physics interest are recorded and the background events rejected, resulting in a few Hz event rate finally written to tape compared to the bunch crossing rate of 91 kHz.

The level-1 and level-2 triggers make their decisions based on special trigger data with coarse granularity and lower resolution provided by the subdetectors, while the level-3 trigger is embedded in the main flow of the data acquisition. The functions of the three trigger levels are described below and the typical rates are quoted in parentheses.

Level-1 Trigger

The level-1 is a logic OR of the five triggers based on the calorimeter (electromagnetic and hadronic), luminosity monitor, scintillation counter, muon chamber and the TEC chamber. Each is gated by the beam crossing signal. A positive result from any of the five will initiate the digitization process which takes 500 μs. A negative result will signal all the electronics to be cleared and be ready for the next beam crossing. The combined rate of level-1 triggers is $5 - 15$ Hz.

Energy trigger (3 Hz) The level-1 energy trigger selects events which deposit more than a few GeV of energy in the calorimeter (electromagnetic or hadronic). The calorimeters are divided into 896 cells. For the electromagnetic calorimeter, the BGO crystals are grouped into $32\,\phi \times 16\,\theta = 512$ cells. The hadron calorimeter is split into 2 radial layers and grouped into 16×11 (16×13) cells for the layer less than (greater than) about one absorption length in depth. The analog sums

of the energies in each cell are digitized and converted into GeV depositions and then calculated to compare with the preset threshold. The quantities used are the total calorimeter energy, the energy in the electromagnetic calorimeter alone and these two energies measured in the barrel region. Typical thresholds are 25, 25, 15 and 8 GeV respectively. Events with localized energy depositions of more than 6 GeV (2.5 GeV in spatial coincidence with a TEC track) also are triggered. A special single photon trigger is implemented to search for events with a single isolated electromagnetic cluster. It uses a threshold of 1 GeV.

TEC trigger (5.5 Hz) The TEC trigger selects events with charged tracks which is a common signature for most of the physics events. It uses information given by 14 pre-selected anode sense wires in every outer sector, binned into two bins of drift time, and searches for correlated hits to form tracks. The TEC trigger is fired when a event has two tracks with minimum transverse momentum of 150 MeV and acoplanarity less than 60°.

Scintillator trigger (0.5 Hz) The scintillator trigger is used to select high multiplicity events and together with the muon trigger, to reject cosmic rays. It requires at least 5 out of 30 scintillation counters fired within 30 ns of the bunch crossing. Among the scintillator counts that have been fired, at least two should be separated by more than 90° in ϕ.

Muon trigger (1.0 Hz) The muon trigger selects events with at least one particle reaching the muon chamber with a transverse momentum larger than 1 GeV where at least 2 out 3 P chambers or 3 out of 4 Z chambers are hit. A coincidence with at least one good hit in a scintillator within a 30 ns gate is required to reduce the background from cosmic rays.

Luminosity trigger (4.0 Hz) The luminosity trigger is designed to accept events coming from small angle Bhabha scattering. An event is triggered if both BGO

calorimeters of the luminosity monitor have at least 15 GeV energy deposition, or if one side of the BGO calorimeter has more than 5 GeV and the other side more than 25 GeV, or if either side has more than 30 GeV.

Level-2 Trigger

The level-2 trigger is designed to reject non-physical background events from electronic noise, beam-gas, beam-wall interactions and synchrotron radiation. The event rate fed through the level-1 trigger is reduced by about 50%.

In case of a positive decision from the level-1 trigger, the level-2 trigger begins to work. Events triggered by more than one level-1 subtriggers are never rejected. Events triggered by only one level-1 subtrigger are further checked using the following criteria which is based on the information not available in time for level-1 decision:

- the clustered energies in the electromagnetic calorimeter and two lateral layers of the hadron calorimeter have to be correlated in the $\theta - \phi$ map;
- the clustered energies have to be balanced in both longitudinal and transverse direction;
- a rough vertex along the beam axis is reconstructed based on the information from the charge division wires of the TEC chamber.

If level-2 gives a positive decision, the input to level-2 together with all level-2 results are fed to the level-3 trigger.

Level-3 Trigger

The decision of the level-3 trigger is based on the full detector readout. Having access to the complete digitized data with finer granularity and higher resolution, the level-3

trigger has a lower threshold than that of level-2 trigger. Several algorithms are used to examine the event.

- The events which are selected by more than one level-1 trigger or the luminosity trigger are passed through untouched,
- The calorimeter algorithm recalculates the event energies and applies similar criteria to those of the energy trigger to pass the event,
- Muon triggers are required to pass a more stringent scintillator coincidence in time, $\pm 10ns$, and space, $\pm 60°$,
- Tracks from TEC trigger events are correlated with at least 100 MeV of energy in the calorimeters. Track quality and vertex position are also examined.

All of these algorithms result in a rate reduction of about 50%, with an output rate of 1 to 4 Hz.

3.3 Data Sample of 1993 and 1994

The data analyzed in this thesis was taken in 1993 and 1994. The total data sample is classified into several subsamples according to the LEP running period and the LEP beam energy. Table 3.2 lists the conventions used in this thesis.

Convention	Run Period			$\sqrt{s}$ (GeV)
93a	May 17	- June 17	1993 prescan	91.3
P-2	June 27	- November 15	1993 scan	89.4
93s	June 27	- November 15	1993 scan	91.2
P+2	June 27	- November 15	1993 scan	93.0
94a	May 5	- June 16	1994	91.2
94b	June 24	- September 12	1994	91.2
94c	September 25	- October 16	1994	91.2
94d	November 12	- November 29	1994	91.2

Table 3.2: Conventions used in this thesis for the classification of the 1993 and 1994 data samples.

Chapter 4

RFQ Calibration

The L3 electromagnetic calorimeter consists of two half barrels and two endcaps, a total of 10734 BGO crystals. It has been designed to provide precise energy measurement of electrons and photons, from less than 100 MeV to 100 GeV. The experiment's ability to detect new physics processes that involve multilepton or multiphoton final states depends on the resolution of the BGO calorimeter, and hence on the quality of its calibration.

This chapter presents a review of the energy calibration techniques of the electromagnetic calorimeter at L3, with an emphasis on the RFQ calibration.

4.1 Introduction

In general, there are two types of calibration. One is *intercalibration* that provides a relative calibration channel-to-channel. The other is *absolute calibration* that provides also an absolute energy scale on top of the intercalibration. In principle, an absolute calibration would be the ideal solution.

One of the absolute calibration techniques is to use a test beam [28] (see Section 4.1.1). It provides an absolute calibration but can only serve as an initial calibration point, since the response of each element (crystal, photodiode, readout chain) of the calorimeter differs over time from channel to channel due to radiation damage and aging effects of the crystal, the crystal-to-photodiode joint, etc. A degradation of resolution from 0.5% at the test beam (50 GeV) to 1.3% at LEP run (45 GeV) has

been observed.

An ideal absolute calibration would make use of a physical process which can provide real-time calibration and doesn't require additional hardware. A common calibration line used at e^+e^- colliders is the electrons from the Bhabha scattering since the electron energy is close to the beam energy. But the fact that the rate of Bhabha events at LEP is too low ($\sim$ 6 electrons/crystal per year on average for the barrel at LEP1) makes it impractical to be used as an intercalibration basis.

An effort has been made to use the cosmic muons that penetrate the BGO crystal longitudinally and deposit on average 220 MeV in the crystal. This technique turns out not to be feasible since it needs too long a time ($\sim$ 1 month) to accumulate enough statistics to calibrate each crystal [29].

A calibration method using a Xenon flash lamp, filters and optical fibers, has been developed by L3. The calibration technique is based on:

(1) the initial calibration set by the test beam result,

(2) tracking of the transparency of the crystals by the Xenon light flash monitors [30](see Section 4.1.2),

(3) the normalization from Bhabha events.

This technique has been able to maintain an energy resolution of 1.3% at LEP1. But it is facing difficulty to maintain the same resolution for the barrel at LEP2 since the Bhabha event rate is about 40 times lower for the barrel at LEP2 than that at LEP1.

The RFQ (See Figure 4.1) calibration, with a design goal to provide an accuracy of better than 1% calibration especially for LEP2, uses a pulsed H^- beam from a Radiofrequency Quadrupole (RFQ) accelerator to bombard a lithium target permanently installed inside the BGO calorimeter. After focusing and steering, the beam is neutralized to allow it to pass undisturbed through the magnetic field of L3. Radiative

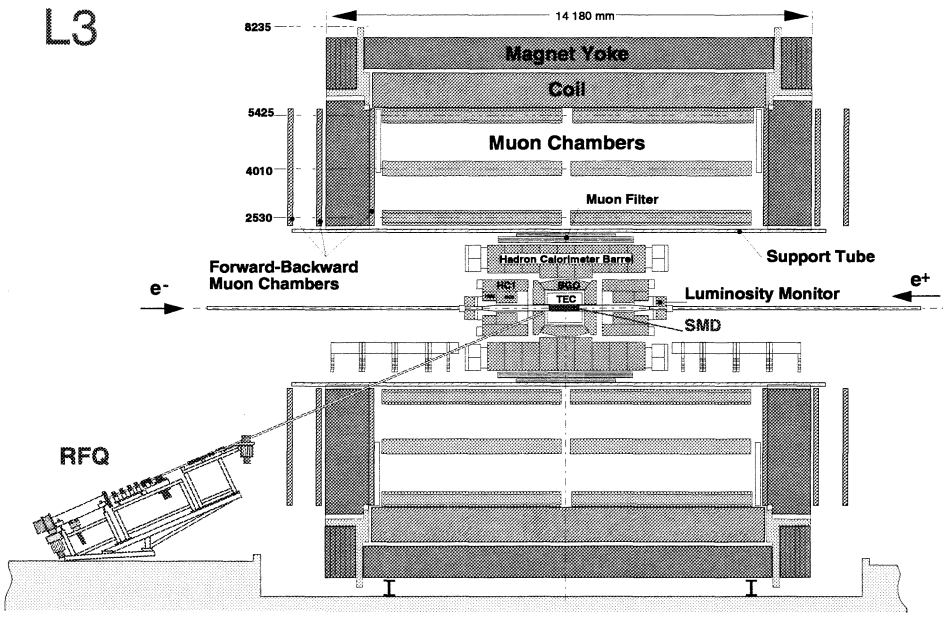

Figure 4.1: Side view of the RFQ system installed in L3.

capture of the protons

$$^{7}_{3}\mathrm{Li}(\mathrm{p},\gamma)\,^{8}_{4}\mathrm{Be}$$

produces 17.6 MeV photons that are used to calibrate the calorimeter in a short time. This technique has achieved an energy resolution of 1.3% for Bhabha electrons at 161 and 172 GeV and therefore is considered unique and successful for LEP 2. Details of this calibration technique are presented in Section 4.2 and Section 4.3.

4.1.1 Test Beam

The two half barrels of the BGO calorimeter were calibrated in 1987 and 1988, with electron beams at four energies: 2, 10, 20 and 50 GeV [28]. During the calibration run, each of the half barrels was installed in a rotating table to permit azimuthal and polar movement in the beam line. A position accuracy of better than 1 mm and an angle between the beam and the crystal longitudinal axis less than 5 mrad were

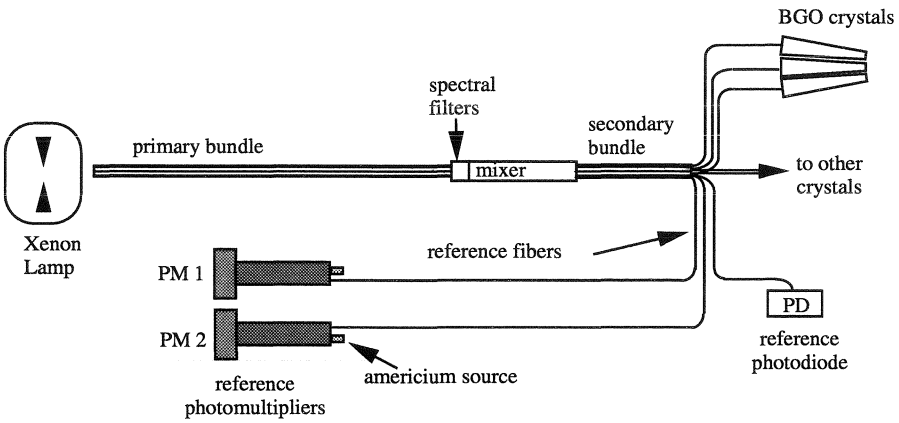

Figure 4.2: Diagram of the Xenon monitoring system.

achieved. The half barrel was enclosed in an air-conditioned tent with a stabilized nominal temperature of $18.0° \pm 0.5°C$. Together with a study at a specially designed beam line with a 180 MeV electron beam extracted from the LEP injector Linac, the test beam results demonstrated an energy resolution of 4% at 180 MeV and 0.5% at 50 GeV.

4.1.2 Xenon Calibration

A simplified diagram of the Xenon monitor is shown in Figure 4.2 and the full configuration is summarized in Table 4.1. The light flashes are generated by a set of Xenon lamps with its spectrum tuned to match with the spectrum of the BGO scintillation light. For each lamp, the light is transported by bundles of optical fibers ("primary fiber bundles") to light mixers and then to the crystals by "secondary fiber bundles." From each mixer, additional fibers transport light to reference detectors, i.e., two photomultipliers (PM) and one photodiode (PD). In the barrel, each crystal receives two fibers from two independent systems, one for high energy pulses (typically 30 GeV equivalent), the other for low energy (about 1.1 GeV equivalent). It

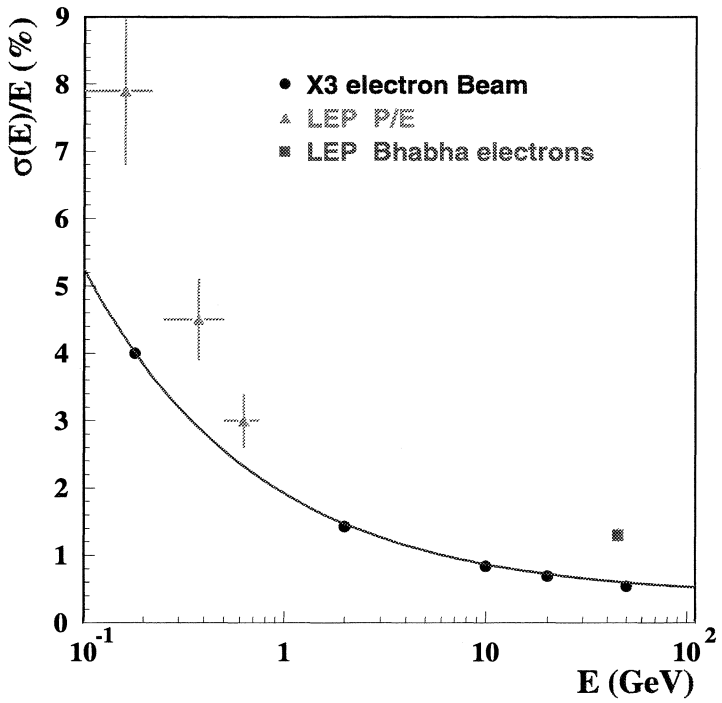

Figure 4.3: Energy resolution with Xenon calibration and test beam.

is therefore possible to monitor the low and high gain channels of the BGO readout electronics. Furthermore, the sectors of the barrel covered by neighboring high and low energy fiber bundles are offset by a few crystal rows in order to investigate systematic effects. The gains of the reference PMs and PDs are monitored by NaI(Am) light pulsers and by ^{241}Am γ rays (for the barrel only) respectively.

Number of elements	Barrel	Endcaps
Xenon lamps	16	16
Mixers per lamp	4	1
Crystals per mixer	240	192
Fibers per crystal	2	1

Table 4.1: Configuration of the Xenon monitor system.

With such a dedicated monitor system, the variation of the crystal transparency as well as the electronic gains are monitored, providing an intercalibration of each crystal

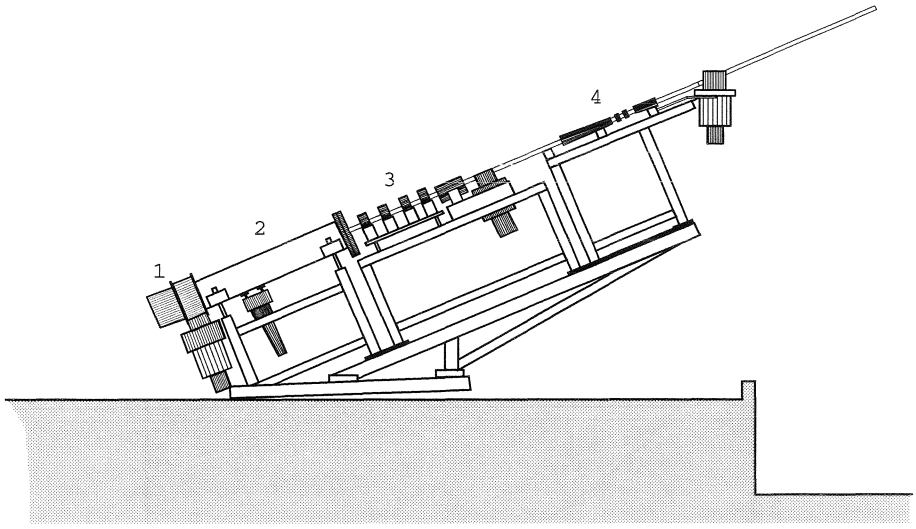

Figure 4.4: The RFQ system: 1) ion source; 2) RFQ ion accelerator; 3) steering and focusing magnets; 4) beam neutralizer.

response relative to its neighbor with the same mixer. The calibration between each mixer is obtained by using the normalization from the Bhabha electrons. The Xenon calibration results in a set of Xenon corrections $X(t)$ to the initial set of calibration constants obtained from the test beam $C(t_0)$:

$$Calibration\ Constant\ = C(t_0) \cdot X(t). \tag{4.1}$$

The energy resolution achieved with Xenon calibration together with the test beam results are shown in Figure 4.3.

4.2 RFQ Calibration System

A general view of the RFQ system is shown in Figure 4.4. The main components of the system are listed as follows:

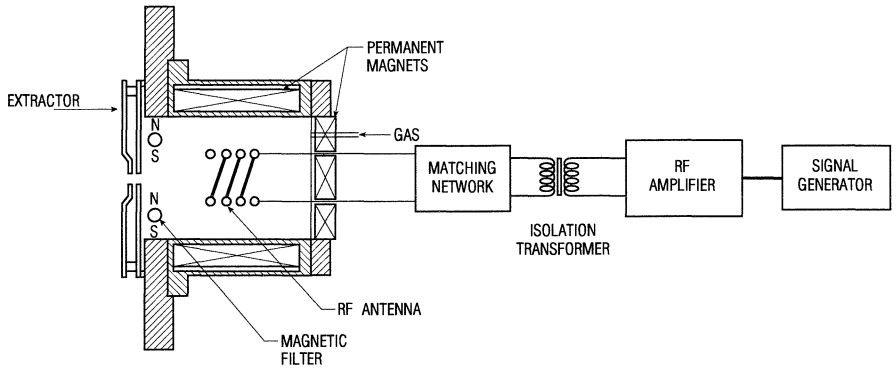

Figure 4.5: A schematic showing the RF-driven H^- ion source.

- a 30 keV H^- ion source,
- a 1.85 MeV RFQ accelerator,
- steering and focusing magnets,
- a ~1 m long beam neutralizer with nitrogen cell,
- a Li Target.

The RFQ accelerator, ion source and beam neutralizer cell are enclosed inside a magnetic shield made of 15mm thick mild steel plates to shield the low energy ion beam from the fringe field of the L3 magnet.

4.2.1 Ion Source

The H^- ion source used is an RF driven volume source originated by LBL [31], and developed and constructed by AccSys Technology Inc. [32] [33].

The source chamber is a copper bucket surrounded by columns of permanent magnets that form a longitudinal linecusp configuration. Its back flange also consists of permanent magnets that provide longitudinal confinement. An H_2 pressure of about 30 mTorr is maintained inside. A 30 kW pulsed RF generator feeds 1.8 MHz

through in the helicoidal antenna to ionize the gas. A hot filament serves as a starter for the plasma.

A pair of water cooled permanent magnet filter rods, which provides a narrow transverse magnetic field to enhance the H^- yield, separates the extraction region from the plasma chamber. The extraction of the H^- beam (populated mostly by e^-) is achieved by the extraction potential between the plasma bucket floating at -30 kV and the grounded extraction electrodes. The e^- component of the beam is further dumped in a spectrometer at 14 keV and the H^- beam is accelerated to 30 keV and focused by electrostatic lens into the RFQ with a typical $\sim$ 7 mA H^- beam current.

4.2.2 RFQ Accelerator

Made by AccSys Technology Inc., the 1.85 MeV RFQ accelerator is a 1.626 m long copper plated mild iron structure of four vane type. It is tuned at 425 MHz resonant frequency and has a typical transmission efficiency of 75% for the injected 30 keV H^- beam. The RFQ is operated with an input of 240 kW RF power and an output pulsed beam of 5 μs at a repetition rate up to 150 Hz. The residual vacuum in the RFQ is maintained to be less than 1×10^{-6} Torr.

The output beam from the RFQ is further focused and steered by a set of quadrupole and dipole magnets before the beam enters the neutralizer.

4.2.3 Beam Neutralizer

The focused and steered H^- beam is neutralized in a N_2 gas cell at 5-9$\times 10^{-4}$ Torr pressure such that the neutral beam can pass through the 0.5 T L3 magnetic field without disturbance. The neutralizer consists of two coaxial steel cylinders with a length of 1 m. The inner cylinder has several hundred holes (diameter $\phi < 1mm$), through which the N_2 gas diffuses into the central region. A typical neutralizing efficiency of $\approx 60\%$ has been achieved with this gas cell.

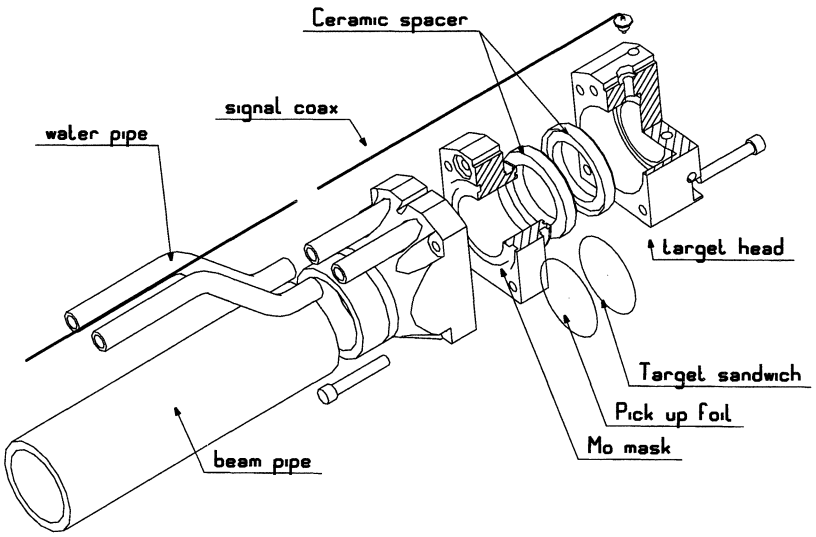

Figure 4.6: The mechanical structure of the target.

At this stage, the beam is focused, steered and neutralized, ready to be transported through a 10 m long beam pipe penetrating the L3 magnet, support tube and calorimeters to reach the Lithium target near one end flange of the TEC chamber.

4.2.4 Target

The Lithium target is based on water cooled metallic Lithium layers (See Figure 4.6). To protect Lithium from exposure to air and humidity, the Lithium foil (50 μm) is sandwiched between two Tantalum foils (5 μm) and then sealed (melted) in a pure Argon atmosphere. Another 6 μm Tantalum foil is mounted isolated from the beam pipe ground on ceramic spacers, about 2 mm upstream. The foil serves two purposes:

(1) as an energy degrader - the resulting thickness of Tantalum upstream (11 μm) is able to degrade the energy of H^0 beam to avoid the unwanted Lithium resonance at 1.03 MeV;

(2) as a Farady cup - the electrons are stripped by this foil to provide a negative signal proportional to the charge of each beam pulse reaching the target.

The target material is encapsulated in a Molybdenum holder. The choice of Molybdenum or Tantalum material is based on the fact that these materials exhibit low radiative capture cross sections such that the unwanted γ ray background is kept to minimun. This Lithium target provided a 17.6 MeV photon yield of up to 160/nCoulomb.

This design of target was used up until 1995 when it was discovered that the Lithium foil would still degrade within a few months, resulting in a LiOH compound which has a six times lower photon production rate. A new target made out of LiH compound (a white power which is stable in dry air and easily handled) was successfully tested in a 1996 run. While the LiH target proved to have a photon yield that is half that of a newly made metallic-Li one, the LiH one is favored due to its long term reliability.

4.2.5 Beam Profile Chambers

To improve the neutral beam diagnostics and facilitate the tuning of the beam optics, a beam profile chamber has been built based on electron secondary emission from gold plated tungsten wires. The chamber consists of two orthogonal wire planes, each with 10 negative biased sense wires interleaved with 11 ground wires. The 10 μm wires are fixed on ceramic frames built using thick film hybrid circuit technology.

When the H^0 beam hits the wires, it knocks out secondary electrons that are expelled due to the negative bias of the sense wire and produce a positive signal proportional to the beam intensity. The charge deposited on the sense wire within $\approx$ 10 μs of the beam passage (typically 0.1 pC) is integrated and amplified by a preamplifier used for the BGO calorimeter readout. After further amplification, the signal is transmitted to the counting room, where a sample and hold circuit synchronized with the beam pulse produces a DC signal proportional to the collected charge

and drives an LED display.

The beam diagnostic chamber was installed about 2 m upstream of the target and has been in use since June 1995.

4.2.6 Trigger and Data Acquisition

The RFQ run is taken with the BGO calorimeter in its "local" standalone read out mode and with a timing configuration very similar to that used during LEP data taking.

The 5 μs RFQ beam pulse on the target is tuned to be coincident with the BGO time mark. Since 1995, a BGO integration gate of 11μs has been used due to the new bunchlet structure (it was 5 μs before). If an RFQ trigger signal is received during the integration gate, the BGO signals, that have been stored in sample/hold circuits are then digitized. The RFQ "trigger accept" signal is generated by detecting the signal from the Faraday cup at the target or by detecting the proton beam pulse as it scatters on a thin wire located upstream of the target.

The RFQ signals registered in the crystals are read out through the BGO token-passing network, and further recorded by the specially designed online histograming module VHC (Veto-Histogram-Counter). The VHC has a 256 channel histogram memory for 8192 crystals. A veto scheme is applied such that a channel will not be histogramed if a neighboring crystal registers a hit above threshold. The veto threshold was set to be 1.0 σ for 1995 and 1.5 σ for 1996 due to the different noise condition. The groundings for the BGO electronics were improved in 1996 which made it possible to set a tighter threshold. The motivation behind this veto scheme is to ensure that the photon shower is well contained in a single crystal.

With this system, a readout speed of 80 Hz has been achieved. To accommodate the memory limitation of the VHC, only half of the detector was read out each run, which is to be fixed when a new VHC with double-sized memory is implemented.

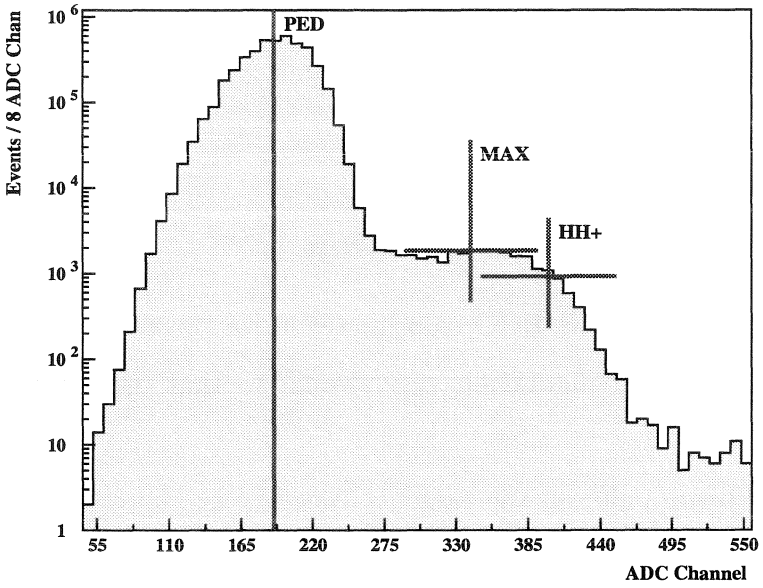

Figure 4.7: Definition of the HH^+ calibration feature.

4.3 RFQ Calibration Technique

4.3.1 Calibration Principle

As mentioned above, the calibration source is the 17.6 MeV photon flux generated by the radiative capture reaction: ${}^{7}_{3}\mathrm{Li}(\mathrm{p},\gamma)\,{}^{8}_{4}\mathrm{Be}$. A typical photon spectrum registered by a BGO crystal is shown in Figure 4.7.

The calibration principle is:

$$\begin{aligned} \textit{Calibration Constant } (KeV/ADC\ Channel) &= \frac{E_{\mathrm{HH+}}}{\mathrm{HH^+} - \textit{Pedestal}} \\ E_{\mathrm{HH+}} &\approx 17.6 \text{ MeV}. \end{aligned} \tag{4.2}$$

where the "HH^+" edge is the specific feature used for calibration and is defined as the point half-way below and to the right of the calibration signal peak. The sharpness

of this falling edge ensures that the HH^+ point is the least sensitive to a variety of possible systematic effects such as the noise level, incident photon angle and materials in front of the crystals, etc. This has been indicated by early Monte Carlo studies, by early tests with a Van de Graaf at Caltech [35], and by tests at AccSys technology [34].

The energy at the HH^+ edge, E_{HH+}, is approximately (but only approximately) equal to 17.6 MeV. There is no reason to believe that E_{HH+} is equal to 17.6 MeV exactly. Since each crystal has a different incident photon angle, different amount of material in front, and different shape, these geometric effects result in a different E_{HH+} for each crystal and are taken into account in the analysis. Details are presented in Section 4.3.4.

HH^+ edge determination

A simple *moving window averaging* algorithm is implemented to determine the HH^+ point. The procedure starts with finding the maximum of the signal peak: we define three adjacent windows and assume the spectrum is parabolic in the windowed region. The windows are slid along until the estimated maximum is found within the windowed region. The maximum is then a weighted average of different estimates obtained with varying window sizes, from 16 to 48 ADC counts.

After the maximum is found, the HH^+point is obtained using almost the same procedure with the only difference being that it uses two adjacent windows and assumes that the spectrum is linear in the windowed region.

Another method of HH^+ edge determination [34] using a cubic spline fit has also been tested and gives similar results.

4.3.2 Data Taking

The RFQ machine system was delivered to CERN at the end of 1991. After a year of recommissioning and system testing, the first RFQ calibration run was taken in 1993,

for half of the BGO calorimeter. With another year's effort devoted to improving the reliability and raising the intensity of the system, we had two successful runs with about 6 million triggers each taken in August and October 1995. Another successful run with similar statistics was taken in June 1996.

The RFQ data was taken during the LEP machine development period. With a DAQ speed of 80 Hz, a run of 6 million triggers takes about 30 hours.

As mentioned before (See Section 4.2.6), a veto scheme is applied to ensure that the photon shower is well contained in a single crystal.

4.3.3 Data Quality

The photon rate is characterized by the *photon occupancy*, defined as the fraction of triggers with energy deposition in a single crystal larger than 14 MeV. The occupancy differs from crystal to crystal due to its different location relative to the Lithium target. Figure 4.8 shows the photon occupancy for the crystals of the half calorimeter on the RB24 side - the RFQ near-side. Typical occupancy is 0.02% for the RB24 side (near side) and 0.005% for the RB26 (far side).

The calibration constants using $E_{\mathrm{HH+}} = 17.6$ MeV are shown in Figure 4.9 with a typical value of 80 KeV/ADC Channel. The calibration constants are all corrected to the reference temperature (18°C) using Eqs. 3.1 and 3.2. The temperature for each crystal was observed to have less than 0.4°C variation.

The quality of the calibration is evaluated by the correlation between two sets of calibration constants derived from two independent runs. A nice correlation is observed (Figure 4.10) between the calibration constants derived from the August run in 1995 and the one derived from the October run in 1995. The width of the distribution of the difference between these two sets of calibration constants (Figure 4.11) provides an estimate for the intrinsic calibration error. An error of 0.7% is concluded from Figure 4.11 for the half barrel on RB24 side. The rest of the detector has a bit

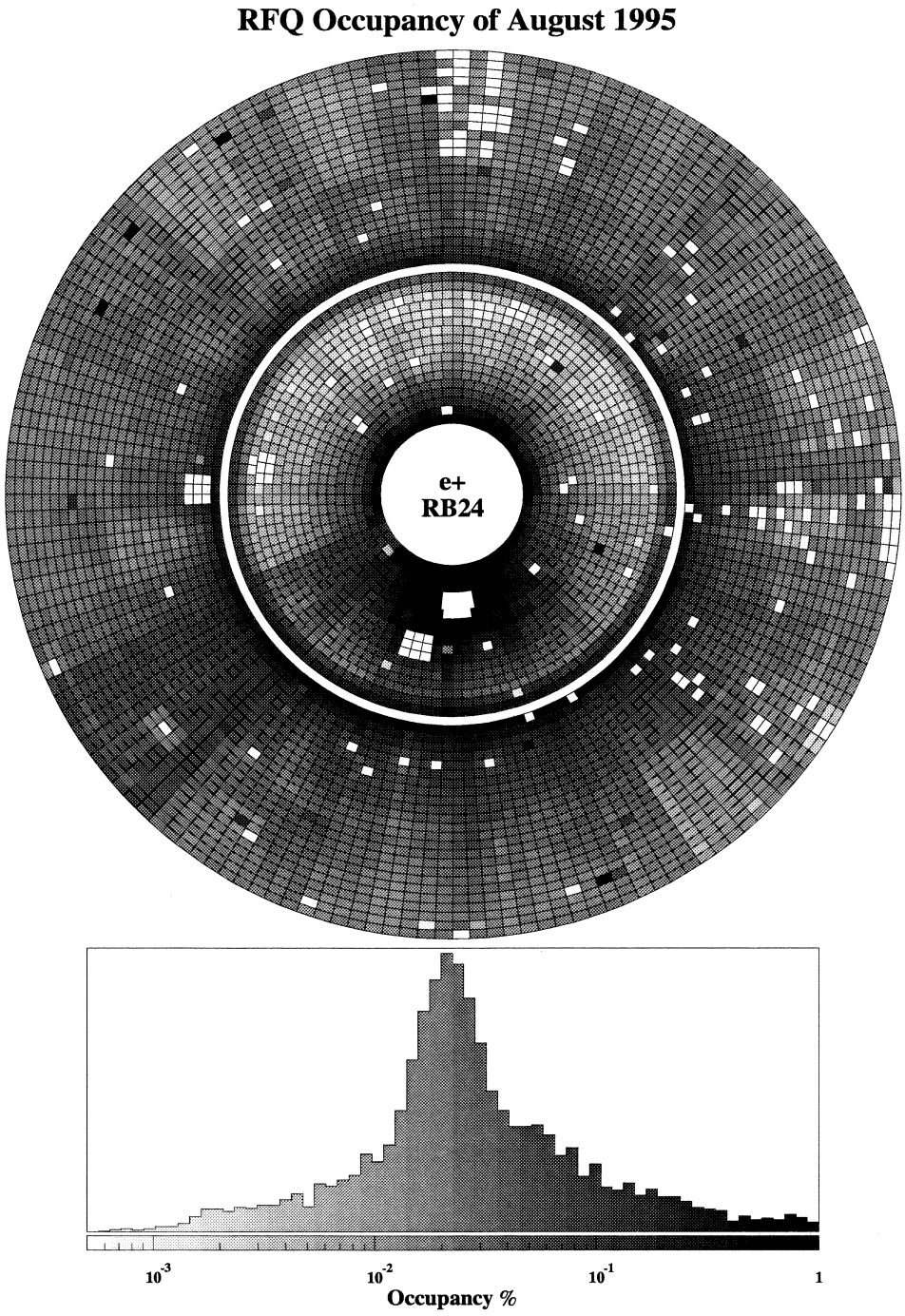

Figure 4.8: RFQ occupancy for the RB24 side, from the RFQ run in August 1995.

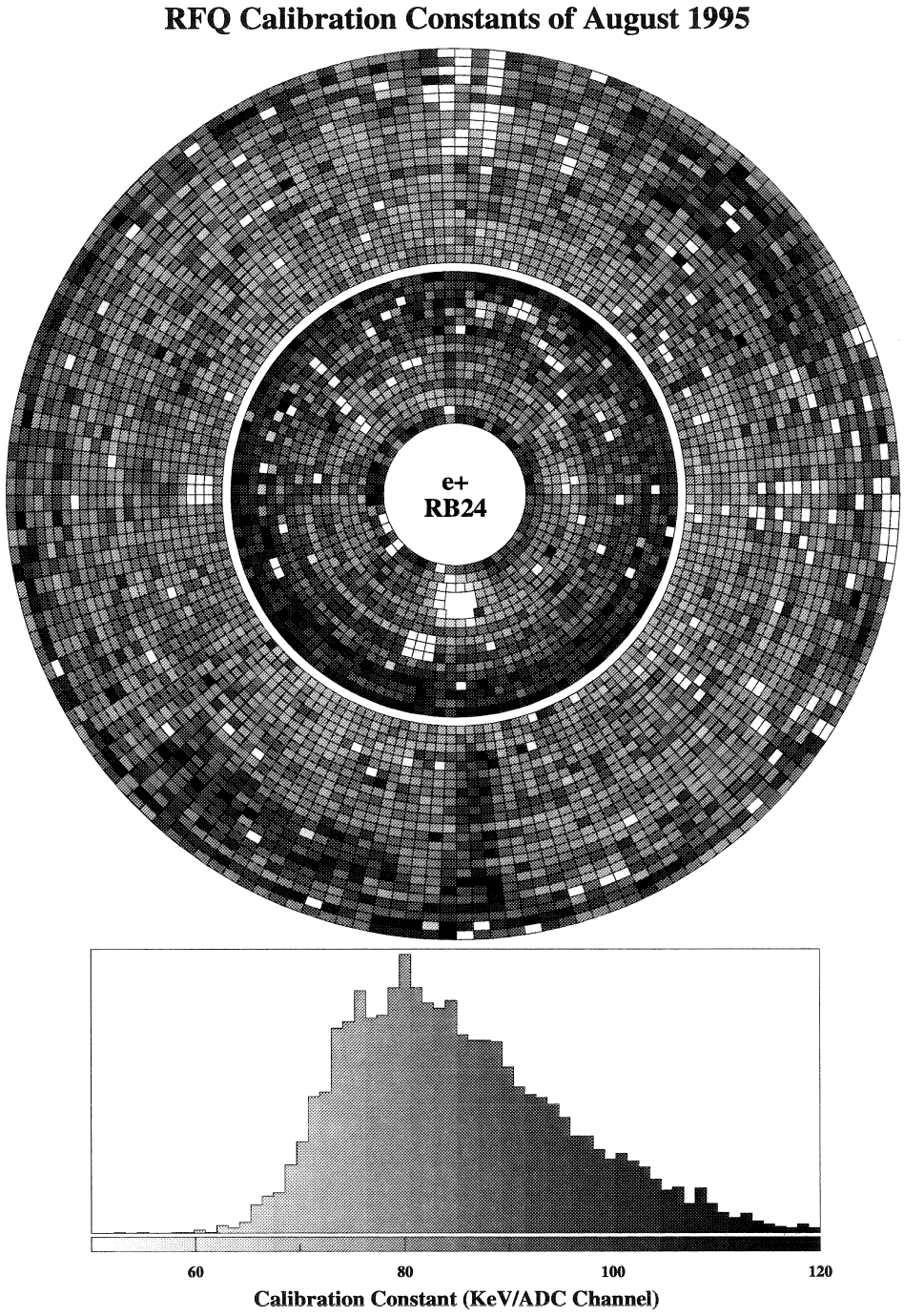

Figure 4.9: RFQ calibration constants for the RB24 side, from the RFQ run in August 1995.

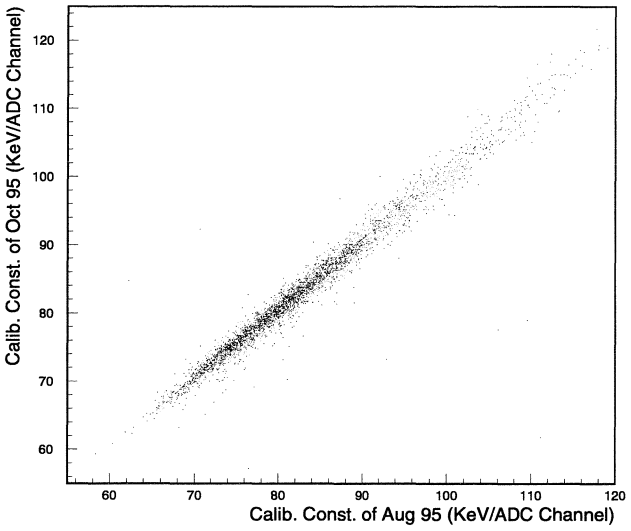

Figure 4.10: Correlation between two sets of calibration constants derived from the August 1995 run and the October 1995 run.

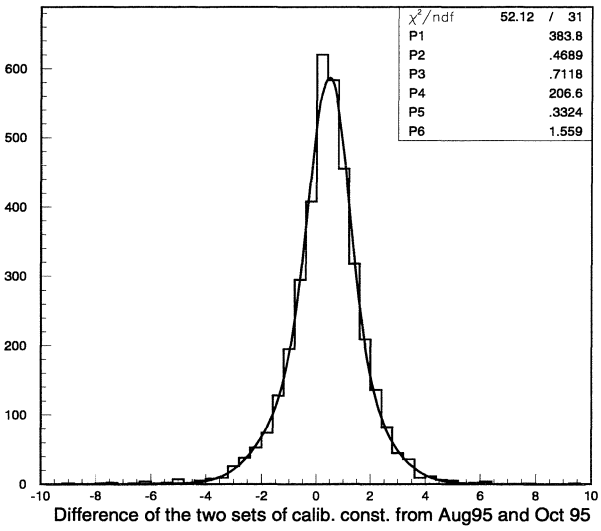

Figure 4.11: Difference between two sets of calibration constants derived from the August 1995 run and the October 1995 run.

worse calibration quality ($\approx$ 1.0%) due to the more complicated geometry effects. For the endcap on the RB24 side, the target is very close causing large glancing angles of incidence and very high occupancy gradient. For the RB26 side, there is the TEC end flange ($\approx$ 5 cm thick aluminium plate) between the target and the detector.

4.3.4 Results

Three sets of calibration constants are derived from the calibration data, which are referred to as "RFQ Only," "RFQ + Bhabha" and "RFQ Corrected."

The "RFQ Only" calibration uses the absolute offset (in ADC channels) of the HH^+ edge from the mean pedestal position as 17.6 MeV. This absolute calibration uses the approximation $E_{HH^+} = 17.6$ MeV. To apply this absolute calibration to the Bhabha electron peak, it also requires an extrapolation from a scale at 17 MeV to energies $\sim$ 45 GeV, thus it suffers from a non-linearity of the calorimeter energy

response over this (very large) range.

We observe that the "RFQ Only" calibration yields a typical energy resolution 2.3% for Bhabha events, which results in 2.1% intrinsic resolution once the radiative correction contribution of 0.8% is subtracted in quadrature. The Bhabha energy resolution without any calibration (*e.g.*, using 100 KeV/ADC Channel) is larger than 8.0% (See Figure 4.12). We also observe that the mean value of the peak is shifted typically by a few percent. This absolute calibration is limited by the geometric effects listed above and the non-linearity of the calorimeter energy response.

An "RFQ+Bhabha" method has been developed to overcome the limitation of the "RFQ Only" calibration. It uses the "RFQ Only" calibration as the relative inter-calibration, and uses Bhabha information to correct the geometric effects. The correction factor is obtained through:

$$\frac{1}{N_{ee}} \sum_{i=1}^{N_{ee}} \frac{E_{beam}}{\sum_{j=1}^{9} ADC_j \times C_j^0},$$

where:

(1) N_{ee} is the number of Bhabha events hitting the crystal;

(2) E_{beam} is the beam energy;

(3) ADC_j and C_j^0 are the ADC value and the calibration constant from the "RFQ Only" method;

(4) j from 1 to 9 refers to the crystal together with its neighboring 8 crystals.

This method results in an improved Bhabha peak resolution of $1.1 - 1.2\%$ resolution (Figure 4.13). After correcting for the radiative contribution of 0.8% to width, the calibration accuracy is determined to be less than 1%.

For 1996, when LEP started to run at energy $\geq$ 80 GeV, there were not enough Bhabha events to do the "RFQ+Bhabha" calibration. A correction tuned from 1995

Bhabha events has been extrapolated based on the fact that most of the geometric effects are time independent. This method is called "RFQ Corrected." An energy resolution of 1.3% for the Bhabha peak at 80 GeV has been obtained with this method (See Figure 4.14). Again after correcting for the radiative contribution 0.8% to width, the calibration accuracy is determined to be $\leq 1\%$. Similar Bhahba energy resolution is achieved for $\sqrt{s} \approx 172$ GeV.

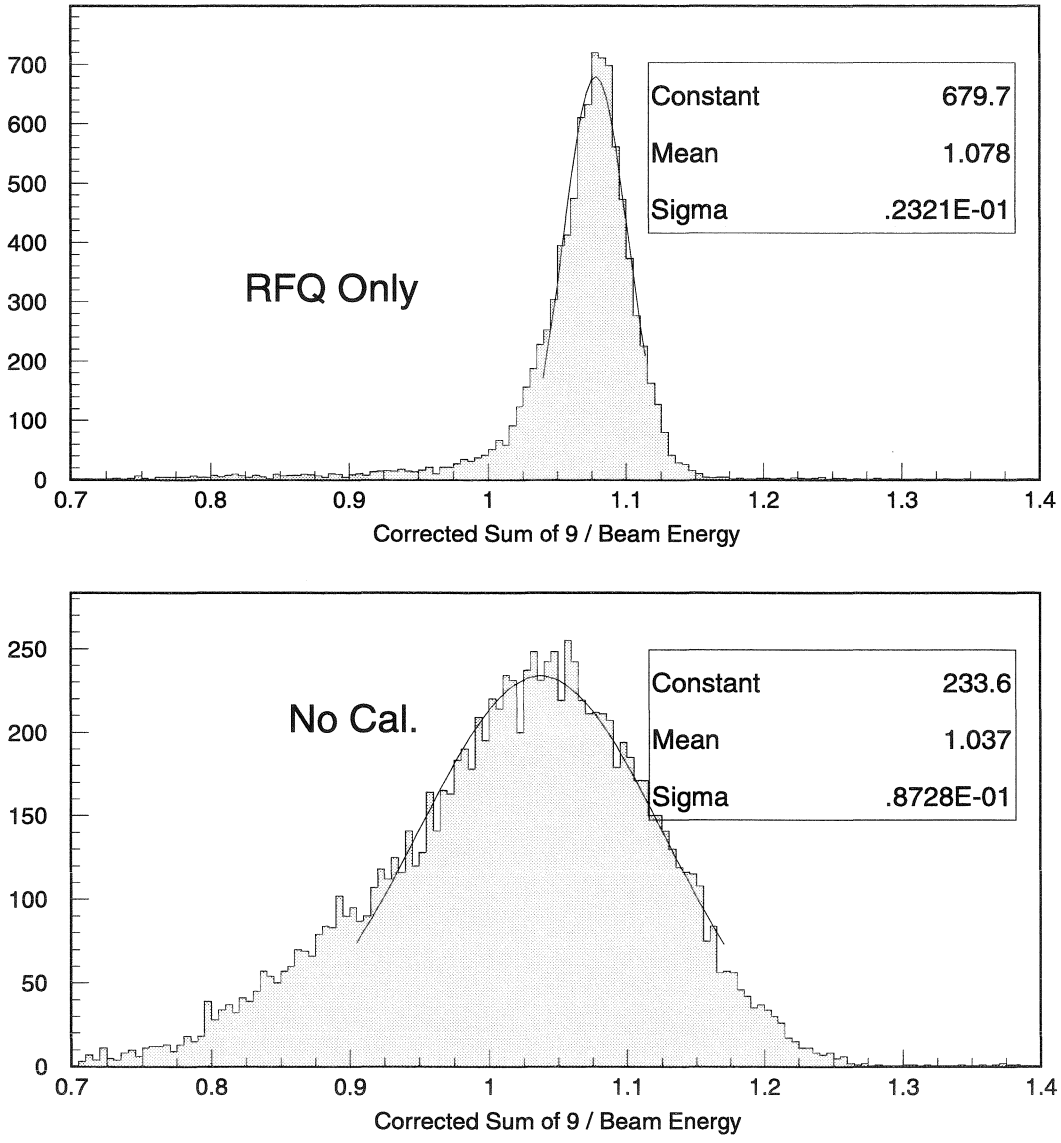

Figure 4.12: Comparison of the Bhabha energy resolution with "RFQ Only" calibration (top) and without any calibration (bottom).

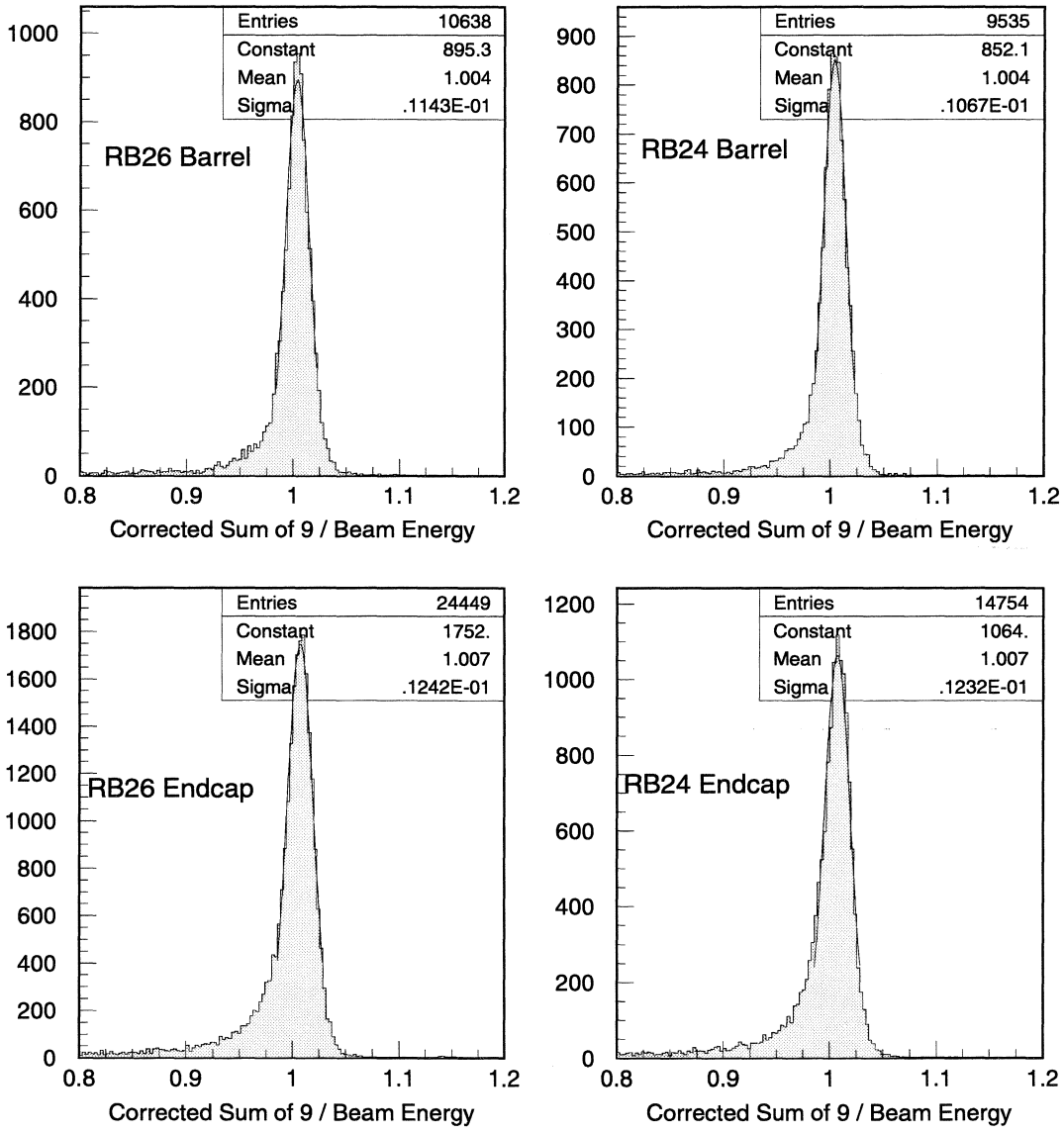

Figure 4.13: Bhabha energy resolution with the "RFQ+Bhabha" calibration.

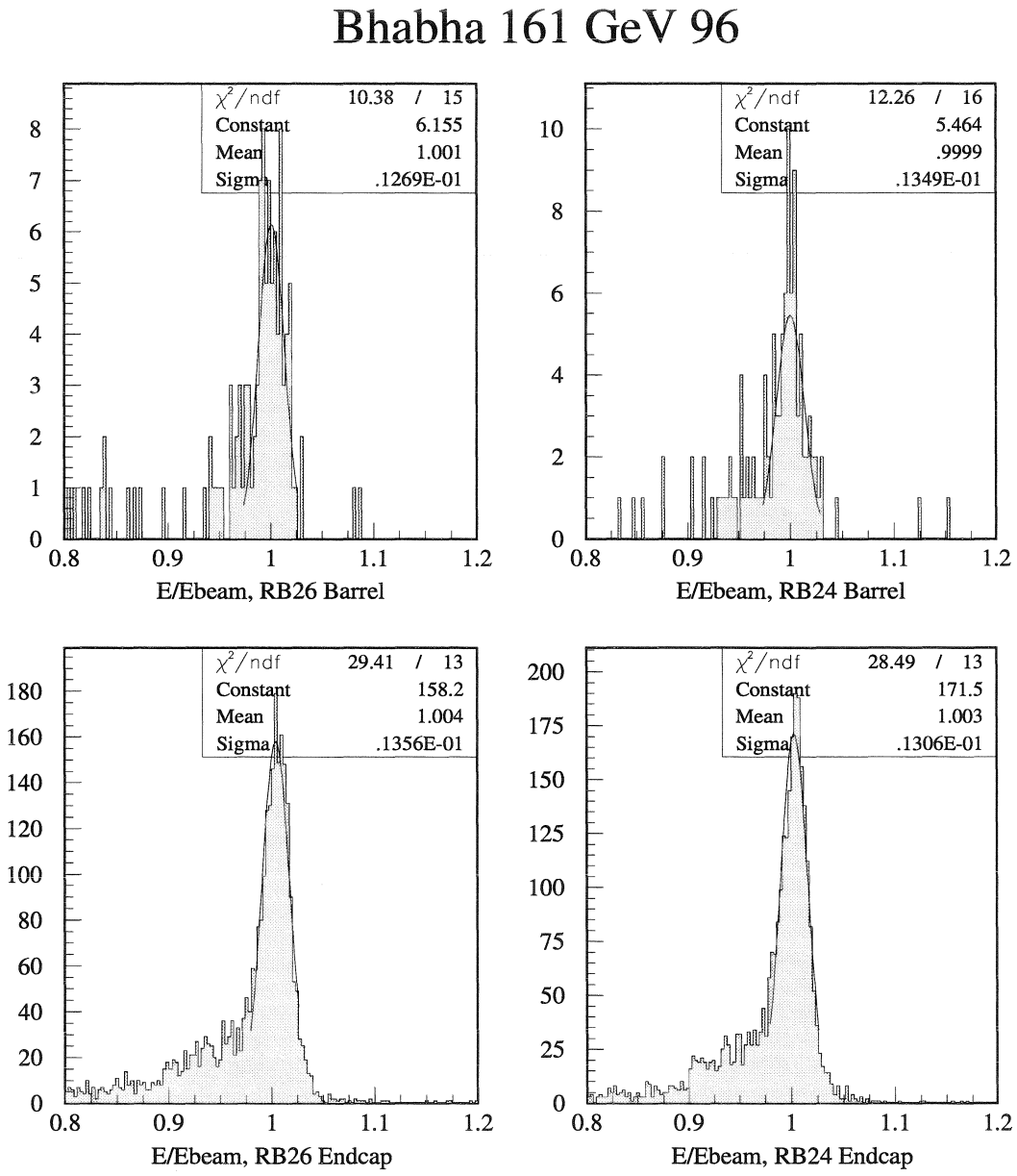

Figure 4.14: Bhabha energy resolution with the "RFQ+corrected" calibration.

Chapter 5

Cross Section and Asymmetry Measurements

In this chapter, I present my data analysis on the cross section and asymmetry measurement for the $e^+e^- \rightarrow e^+e^-(n\gamma)$ process at the Z resonance.

In the first section (Section 5.1), I present in detail the selection of $e^+e^-(n\gamma)$ events based on the information from the tracker (TEC-based selection). Contrary to the previous event selection which was based only on the information from the electromagnetic calorimeter (BGO-based selection), the TEC-based selection has the distinct advantage that it is less dependent on Monte Carlo predictions for radiative multi-photon events that are not well calculated by theory. Detailed studies on events with a certain topology named as *"photon events,"* which initiated the development of this new selection, are shown in Section 5.1.2. The essential ingredient of the TEC-based selection and the measurement of photon events is a very precise determination of the TEC efficiency which has been achieved with a precision of 0.1% and is presented in Section 5.1.3.

The results of the cross section measurement using the TEC-based selection are presented in Section 5.2. The forward-backward asymmetry measurement is presented in Section 5.3.

5.1 Selection of $e^+e^-(\gamma)$ Events

The selection of $e^+e^-(\gamma)$ events is based on the signature of the process $e^+e^- \rightarrow e^+e^-(n\gamma)$: low multiplicity but high energy deposition in the electromagnetic calorimeter, and two tracks in the tracker. A typical $e^+e^- \rightarrow e^+e^-(n\gamma)$ event is shown in Figure 5.1, which is characterized by two back-to-back large showers in the electromagnetic calorimeter, each matching with a track reconstructed in the central tracker (TEC).

5.1.1 BGO-Based Selection

The original $e^+e^-(n\gamma)$ event selection in L3, the so-called *BGO-based selection*, is based on the information on the reconstructed objects (BGO BUMP) in the electromagnetic calorimeter (ECAL). Its main selection criteria are as follows:

Fiducial volume $44^o < \theta_1, \theta_2 < 136^o$.

θ_1, θ_2 are the polar angles of the two most energetic bumps. This is to minimize the contribution from the t-channel and to maximize the sensitivity to the Z contribution. The angles are set to have the reconstructed impact point of the particle at least one crystal away from the BGO barrel edge to ensure the quality of the shower reconstruction.

Acollinearity $\zeta < 25^o$.

ζ is the acollinearity between the two most energetic bumps. This cut is to reduce the sensitivity to radiative corrections.

Energy cut $E_1 > 0.9\ E_{beam}$ and $E_2 > 2$ GeV or $E_{BGO} > 0.7\sqrt{s}$.

E_1 and E_2 are the energies of the two most energetic bumps respectively. E_{BGO} is the sum of the energies of up to four most energetic bumps. This is the most important cut for the selection. Their separation power of the signal from the

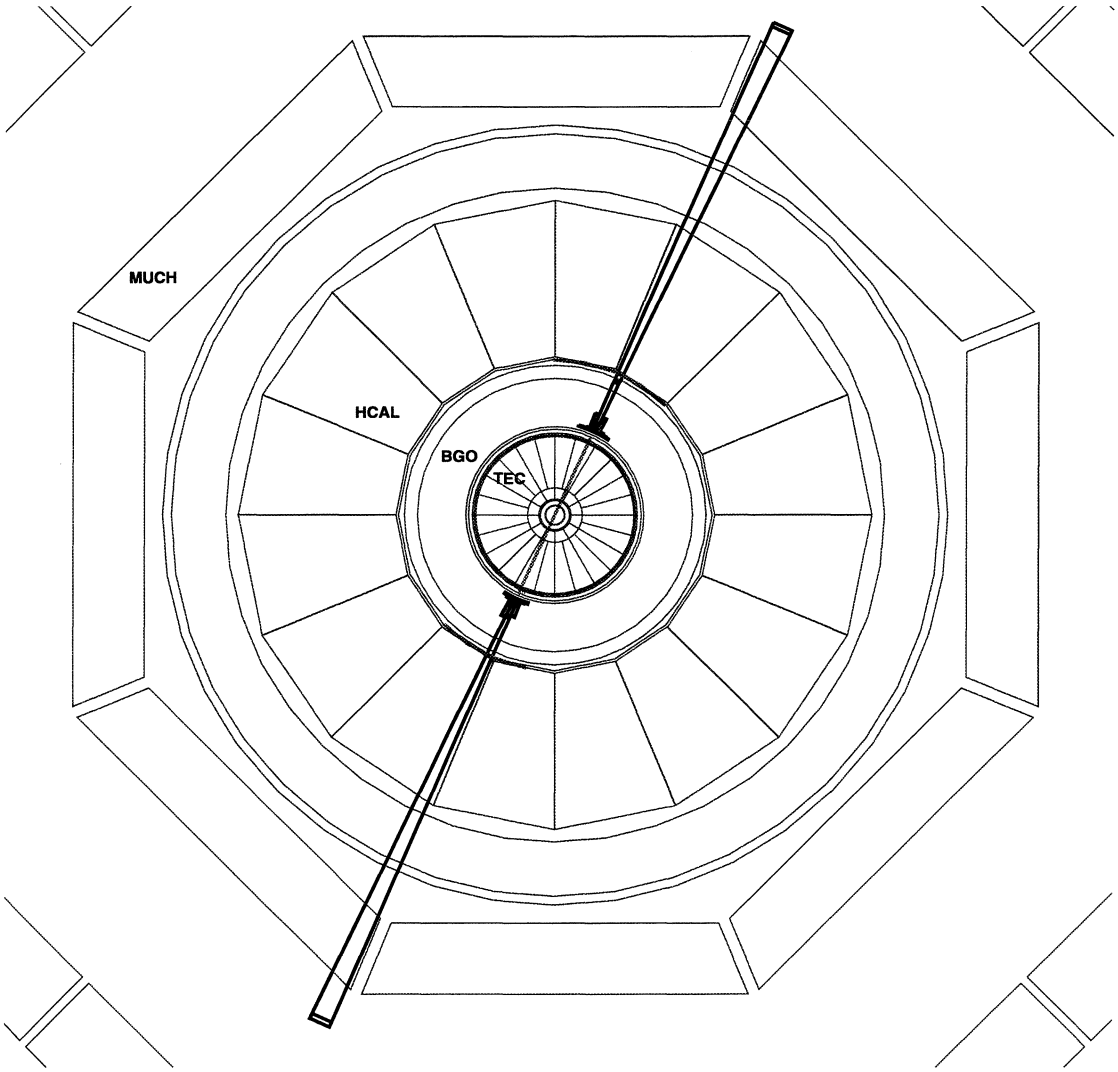

Figure 5.1: End view of a typical Bhabha event recorded by the L3 detector. Two tracks are reconstructed in the TEC, which are matched to the ECAL reconstructed objects (BUMPs). The energy depositions in the ECAL are shown as towers for each crystal, whose heights are proportional to the crystal energy depositions.

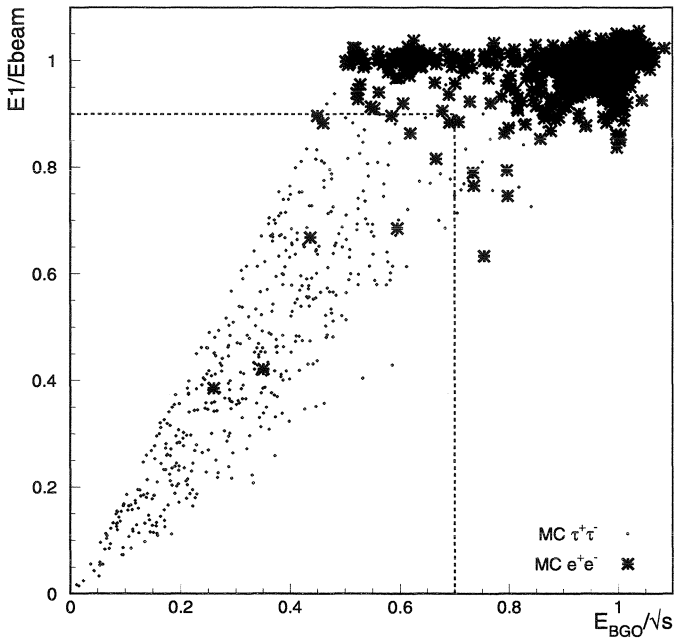

Figure 5.2: The fractional energy of the most energetic bump in the BGO (E_1) versus the sum of energies of the four most energetic bumps in BGO, normalized to the beam energy (E_{EBGO}). The lines correspond to the values of the cuts.

main background $\tau^+\tau^-$ is demonstrated in Figure 5.2. The cut $E_2 > 2$ GeV is to decrease the sensitivity to the dead crystals and BGO support structure.

Multiplicity $N_{bump} < 15$.

N_{bump} is the number of reconstructed objects (BGO BUMP) in the ECAL. This cut suppresses the $q\bar{q}$ background.

With only the BGO information, this BGO-based selection is charge blind. Therefore, there is a potential problem from the *photon events* discussed in the following section.

5.1.2 Photon Events

The problem of *photon events* arises from the fact that the BGO-based selection is charge blind. The assumption embedded in the BGO-based selection is that the

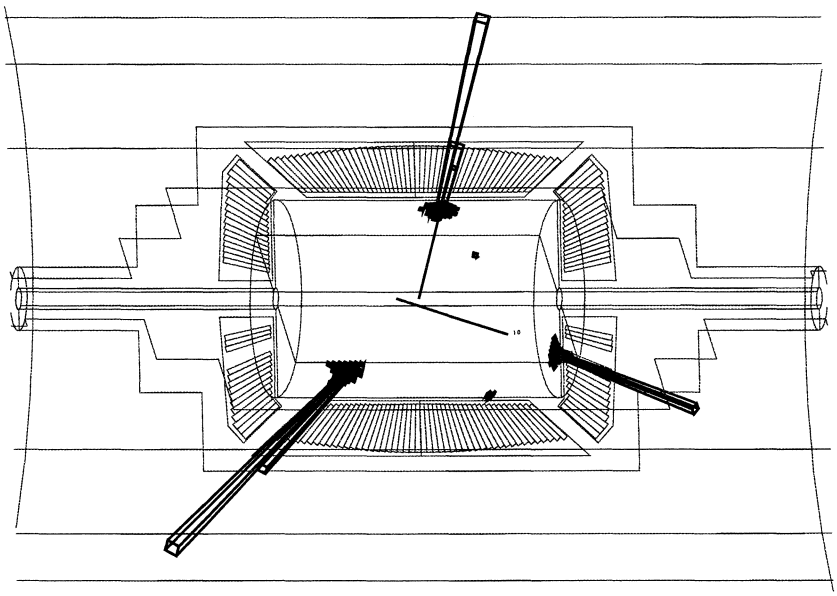

Figure 5.3: A typical photon event which has one of the two electrons in the BGO endcap and an energetic photon in the BGO barrel. This event is not a large angle Bhabha event ($44° < \theta_{e^+e^-} < 136°$) but passes the BGO-based selection.

two most energetic BUMPs are the scattered electrons. Due to its charge blindness, the BGO-based selection would select events with topologies where one of the two most energetic particles is actually a photon, while one of the electrons is outside the fiducial volume ($44° - 136°$). These events are called *photon events*. They are not genuine large angle Bhabha events, which are supposed to have the two electrons inside the fiducial volume. A typical photon event is shown in Figure 5.3.

In principle, these photon events should be well simulated by the Monte Carlo. But the Monte Carlo only generates Bhabha events with the scattered e^+e^- in a certain angular region. The commonly used angular region is $35° < \theta_{e^+e^-} < 145°$ which is only 9° larger than the selected fiducial volume ($44° - 136°$). Therefore, photon events with an electron outside the simulated angular region are not simulated by the Monte Carlo.

Table 5.1 shows the photon event contamination predicted by various generators

for different e^+e^- angular regions. Although for the $35° - 145°$ angular region the various generators have very similar predictions, for $10° - 170°$ their results are very different. BHAGENE [36] and UNIBAB [38] predict 2.43% and 1.36% respectively, which according to the data are obviously wrong. It should be at 10^{-3} level and can't be as large as the percent level, otherwise it would have been noticed much earlier. The prediction from BABAMC [37] is not reliable due to the fact that BABAMC only generates one hard photon. BHWIDE [39] is a new generator, released in the summer of 1996. Fully simulated BHWIDE events at the detector level were not yet available at the time of this analysis. A brief summary of these generators is presented in Appendix D.

$\theta^{gen}_{e^+e^-}$	BABAMC	BHAGENE	UNIBAB	BHWIDE
$40^o - 140^o$	0.08 ± 0.02			
$35^o - 145^o$	0.14 ± 0.02	0.14 ± 0.01	0.13 ± 0.02	0.05 ± 0.03
$10^o - 170^o$	0.18 ± 0.03	2.43 ± 0.11	1.36 ± 0.12	0.21 ± 0.05
$1^o - 179^o$	0.09 ± 0.03			0.11 ± 0.01

Table 5.1: Predictions of the photon event contamination (%) from different generators. $\theta^{gen}_{e^+e^-}$ is the polar angular region of generated electron and positron.

From the generator study shown above, I conclude the following:

(1) The prediction for the rate of photon event contamination from the Monte Carlo is not reliable, and a direct measurement from the data is necessary;

(2) the final solution to this problem from the photon events would be identifying electrons using a TEC-based selection;

(3) the precision of the measurement should be at the level of 10^{-3}, which requires that the knowledge of the TEC inefficiency be determined with a precision of 10^{-3}.

5.1.3 Determination of TEC Inefficiency

The usual method to determine the TEC inefficiency is to use the "golden $\mu^+\mu^-$" data sample. A golden muon is defined to have a well-measured track from the muon chamber. Each muon should also leave a track inside the TEC. By counting the number of muons that have missing tracks in the TEC, one can get an estimate of the TEC inefficiency. Unfortunately there exist gaps between the octants of the muon chamber that are aligned with the anode/cathode regions of the TEC where TEC has the lowest efficiency. So the estimation of the TEC inefficiency using this method is biased, and the method is not suitable for a very high precision measurement.

I developed a new method based on the golden e^+e^- data sample. This golden sample contains events that satisfy the following criteria:

- number of reconstructed objects in the BGO calorimeter $N_{BUMP} = 2$;
- acollinearity of the two bumps $\zeta < 1°$;
- energy of the bumps is at least 30 GeV.

Monte Carlo study shows that with these cuts, the sample obtained is a pure two-electron sample that has no photon event admixture.

The definition of a measured electron is illustrated in Figure 5.4: a measured electron corresponds to the reconstructed object in the BGO (BGO BUMPs) being matched with at least 5 anode wires hit in the TEC within a 3° half-angle cone in the $r\phi$ plane. Considering the fact that the noise in the TEC might induce several hits in a single wire, I do not use the number of hits but the number of wires instead for my electron definition in order to reduce this noise effect. The reason that I do not use the reconstructed TEC track for the definition is because it induces biases at the 1% level, due to the low reconstruction efficiency in the anode/cathode regions. Using the number of wires instead has reduced this bias to 0.1%.

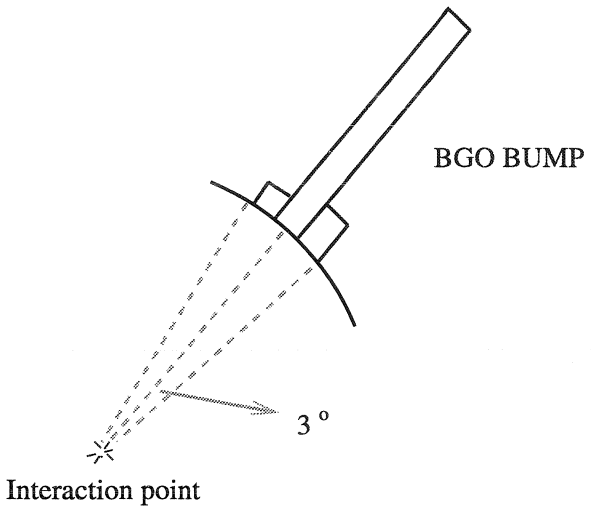

Figure 5.4: Schematic representation of the definition of a measured electron: at least 5 anode wires of the TEC chamber must be hit matching with a BGO BUMP within $\pm 3°$ azimuthal angle.

Applying such a definition to the golden data sample obtained, the TEC inefficiency can be determined from

$$\varepsilon^{ineff} = \frac{N_{single}}{N_{total}}, \tag{5.1}$$

where N_{single} is the number of the single-measured electron events, and N_{total} is the number of the total events in the golden data sample. The TEC inefficiency for a electron to be reconstructed using my electron definition is $\frac{1}{2}\varepsilon^{ineff}$.

Figure 5.5 shows the comparison between data and Monte Carlo, for the distribution of the number of wires that registers hits for a measured-electron defined above. We observe that the Monte Carlo doesn't simulate very well the hit efficiency, which is 97% in data and 92% in Monte Carlo. Since the precision is desired to be at 0.1% level, a simple scaling approach is not a solution. To avoid this imperfection, I measured and then corrected the TEC efficiency for data and Monte Carlo independently.

The measured results from the 93/94 data are listed in the first row of Table 5.2.

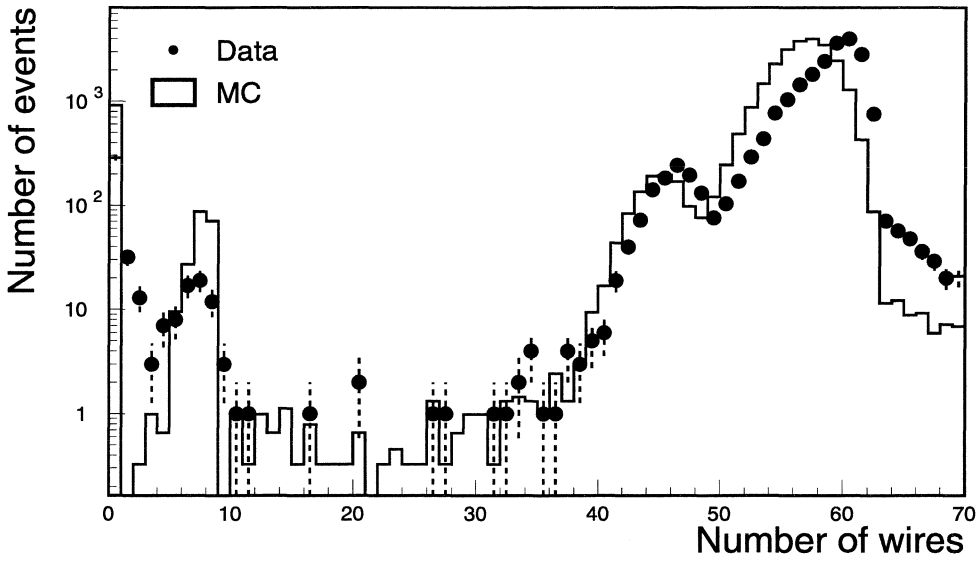

Figure 5.5: Distribution of number of wires that register hits for a measured-electron.

Same method has been applied on the fully simulated Monte Carlo and its results, listed in the second row of Table 5.2, are compared with its real TEC inefficiency retrieved from the generator level information. An agreement at the 0.1% level can be seen in the comparison, which provides strong evidence that my technique for the determination of the TEC inefficiency has reached a precision of 0.1%.

This method has been checked to be free from the $\tau^+\tau^-$ background. But there still exists the background contribution from $\gamma\gamma$ final states from the process $e^+e^- \rightarrow \gamma\gamma$, where γ-conversion happens in the material between the production point and the tracking chamber, and results in fake Bhabha electrons. The γ-conversion probability is found to be 2.5%, which corresponds to a total effect of 0.04-0.09% on the TEC inefficiency ε^{ineff} determination for different energy points. This has been corrected for the results listed in Table 5.2.

$\varepsilon^{ineff}(\%)$	93a	93s	P-2	P+2	94
Data	0.04 ± 0.06	0.01 ± 0.03	0.07 ± 0.08	0.15 ± 0.14	0.06 ± 0.02
MC rel3	0.02 ± 0.00	0.07 ± 0.01	0.05 ± 0.02	0.02 ± 0.01	0.11 ± 0.01
MC gen	0.04 ± 0.00	0.11 ± 0.01	0.09 ± 0.02	0.08 ± 0.01	0.19 ± 0.01

Table 5.2: Results of the TEC inefficiency ε^{ineff} measured from 1993 and 1994 data. The first row lists the results from data; the second row shows the results measured from the fully simulated and reconstructed Monte Carlo (rel3) while the last row shows the results retrieved from the generator information (gen).

5.1.4 Measurement of the Photon Events

I used the counting method to measure the photon events. The photon events are classified in two categories: *single-measured electron* events and *double-measured electron* events. For *single-measured electron* events, the photon-event contamination is estimated from the difference between the total sample and the background (TEC inefficiency, $\tau^+\tau^-$ and $\gamma\gamma$ events). For *double-measured electron* events, the photon event can be recognized from the fact that the polar angle of the measured electron is outside the BGO barrel. In this case, it should be in the BGO endcap since it's detected. The simplest two BUMP case is illustrated in Figure 5.6.

The typical topology for the $\tau^+\tau^-$ background is on one side, the $\tau^\pm$ decays to $e^\pm\nu$ with an energetic electron; on the other side, $\tau^\mp$ decays to $\pi^\mp\pi^0$ and fakes a photon. The background from $\gamma\gamma$ due to the γ-conversion, as discussed in Section 5.1.3, has been taken into account.

The photon event contaminations, $\varepsilon^\gamma(\%)$, are measured for the 93/94 data sample, the fully simulated BHAGENE (BGE) Monte Carlo and the fully simulated $\tau^+\tau^-$ Monte Carlo (KORALZ [40]) sample. Results are listed in Table 5.3.

Since the photon event contamination is a physical quantity which should not be time/detector dependent and also the statistical error for the measurement is very

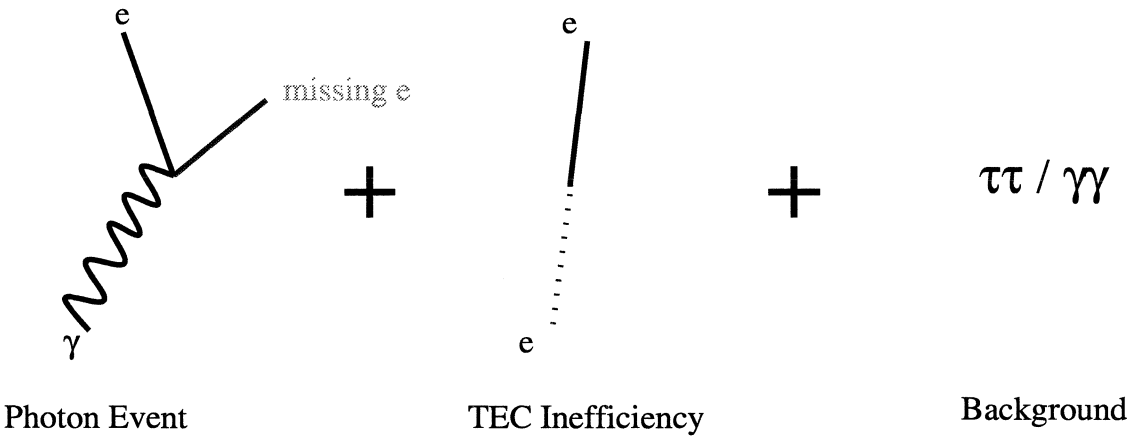

Figure 5.6: The *single-electron* event with only two bump reconstructed in the detector has three kinds of sources: photon event; Tec inefficiency and $\tau^+\tau^-$ background.

large, a meaningful average can be obtained from the five data samples:

$$\begin{aligned}
\overline{\varepsilon}^{\gamma}_{data} &= 0.43 \pm 0.04\ \% \\
\overline{\varepsilon}^{\gamma}_{BGE} &= 0.14 \pm 0.01\ \% \\
\overline{\varepsilon}^{\gamma}_{\tau\tau} &= 0.12 \pm 0.01\ \% \\
\overline{\varepsilon}^{\gamma}_{\gamma\gamma} &= 0.05 \pm 0.00\ \%.
\end{aligned}$$

$\varepsilon^{\gamma}(\%)$	93a	93s	P-2	P+2	94
Data	0.23 ± 0.13	0.49 ± 0.09	0.39 ± 0.17	0.36 ± 0.26	0.43 ± 0.05
BGE MC	0.13 ± 0.02	0.17 ± 0.02	0.14 ± 0.04	0.17 ± 0.03	0.11 ± 0.02
$\tau\tau$	0.15 ± 0.03	0.14 ± 0.03	0.08 ± 0.02	0.20 ± 0.04	0.13 ± 0.05
$\gamma\gamma$	0.04 ± 0.01	0.04 ± 0.01	0.07 ± 0.01	0.09 ± 0.01	0.04 ± 0.01

Table 5.3: Results of the measurement of the contamination of the photon events from 1993 and 1994 data sample, from the BHAGENE Monte Carlo (BGE, $35° - 135°$) and from the $\tau^+\tau^-$ Monte Carlo. Monte Carlo are with full detector simulation.

$\varepsilon^{\gamma}(\%)$	93a	93s	P-2	P+2	94
BGE I rel3	0.13 ± 0.02	0.17 ± 0.02	0.14 ± 0.04	0.17 ± 0.03	0.11 ± 0.02
gen	0.13 ± 0.01	0.13 ± 0.01	0.16 ± 0.03	0.10 ± 0.01	0.12 ± 0.01
BGE II rel3	2.79 ± 0.12	2.79 ± 0.13			
gen	2.69 ± 0.12	2.69 ± 0.12			

Table 5.4: Comparisons of the measurement of the photon event contamination for Monte Carlo BHAGENE at the fully simulated detector level with the prediction at its generator level. BGE I is BHAGENE with $35 < \theta_{e^+e^-} < 145$ and BGE II is BHAGENE with $8 < \theta_{e^+e^-} < 172$. "rel3" refers to the Monte Carlo with full detector simulation. " gen" refers to the Monte Carlo at the generator level.

Therefore, the photon event contanmination measured from the data is

$$\Delta(\overline{\varepsilon}^{\gamma}_{data} - \overline{\varepsilon}^{\gamma}_{\tau\tau} - \overline{\varepsilon}^{\gamma}_{\gamma\gamma}) = 0.26 \pm 0.05(\%)\,,$$

and the difference from the Monte Carlo prediction is

$$\Delta(\overline{\varepsilon}^{\gamma}_{data} - \overline{\varepsilon}^{\gamma}_{\tau\tau} - \overline{\varepsilon}^{\gamma}_{\gamma\gamma} - \overline{\varepsilon}^{\gamma}_{BGE}) = 0.12 \pm 0.05(\%)\,.$$

This tells us that the number of photon events, which originate from the events with e^+e^- outside the Monte Carlo simulated angular region $35° - 145°$, and hence are not simulated, is very small $\approx 0.1\%$, or the underestimation of the Monte Carlo $(35° - 135°)$ using the BGO-based selection is $\approx 0.1\%$.

To check the precision of this method, the results measured using Monte Carlo with full detector simulation are compared with the prediction of its generator level information. As listed in Table 5.4, the agreement is better than 0.1%, which convinces us that the precision of the measurement for the photon event contamination is at the level of 0.1%. One thing that is worthwhile to be pointed out is: a photon event contamination as large as 2.7%, predicted by BHAGENE with $8 < \theta_{e^+e^-} < 172$, can be recovered/measured with my technique.

5.1.5 TEC-Based Selection

With the high precision knowledge of the TEC inefficiency, I have developed a new TEC-based selection for $e^+e^-(n\gamma)$ events. The new selection is motivated by the charge blindness of the BGO-based selection and by the photon event study. Compared with the BGO-based selection, this selection is more natural since it does identify the electrons. It has the advantage that it is independent of the Monte Carlo prediction for the photon event contamination. Besides, the $\gamma\gamma$ background (from $e^+e^- \rightarrow \gamma\gamma$) which is indistinguishable in the BGO-based selection is eliminated by the TEC-based selection.

Data Quality

The distributions of the three main selection variables (acollinearity, E_1 and E_{BGO}) are illustrated in Figure 5.7 where good agreement between data and Monte Carlo is observed.

The excess of data (1.3%) on the high energy end of the E_1 distribution with $E_1/E_{beam} > 1.05$ comes from bad reconstruction around noisy crystals. A distribution of E_2 (Figure 5.8) for these events exhibits a clear BHABHA peak, indicting that these events are real e^+e^- signal events. The excess is diluted in the distribution of E_{BGO} due to the fact that E_{BGO} is the sum of energies of the four most energetic bumps in the BGO. The low energy resolution at low energies (E_3, E_4) washes out the excess.

Gap Events

As mentioned in Chapter 3, there exist gaps between the crystals due to the support structure. The widths of the gaps vary from 200 μm to 900 μm in reality but are fixed to a constant 200 μm in the Monte Carlo simulation. An electron hitting the crystal on its edge will result in a lower energy deposition in the electromagnetic calorimeter and a leakage of the energy to the hadron calorimeter.

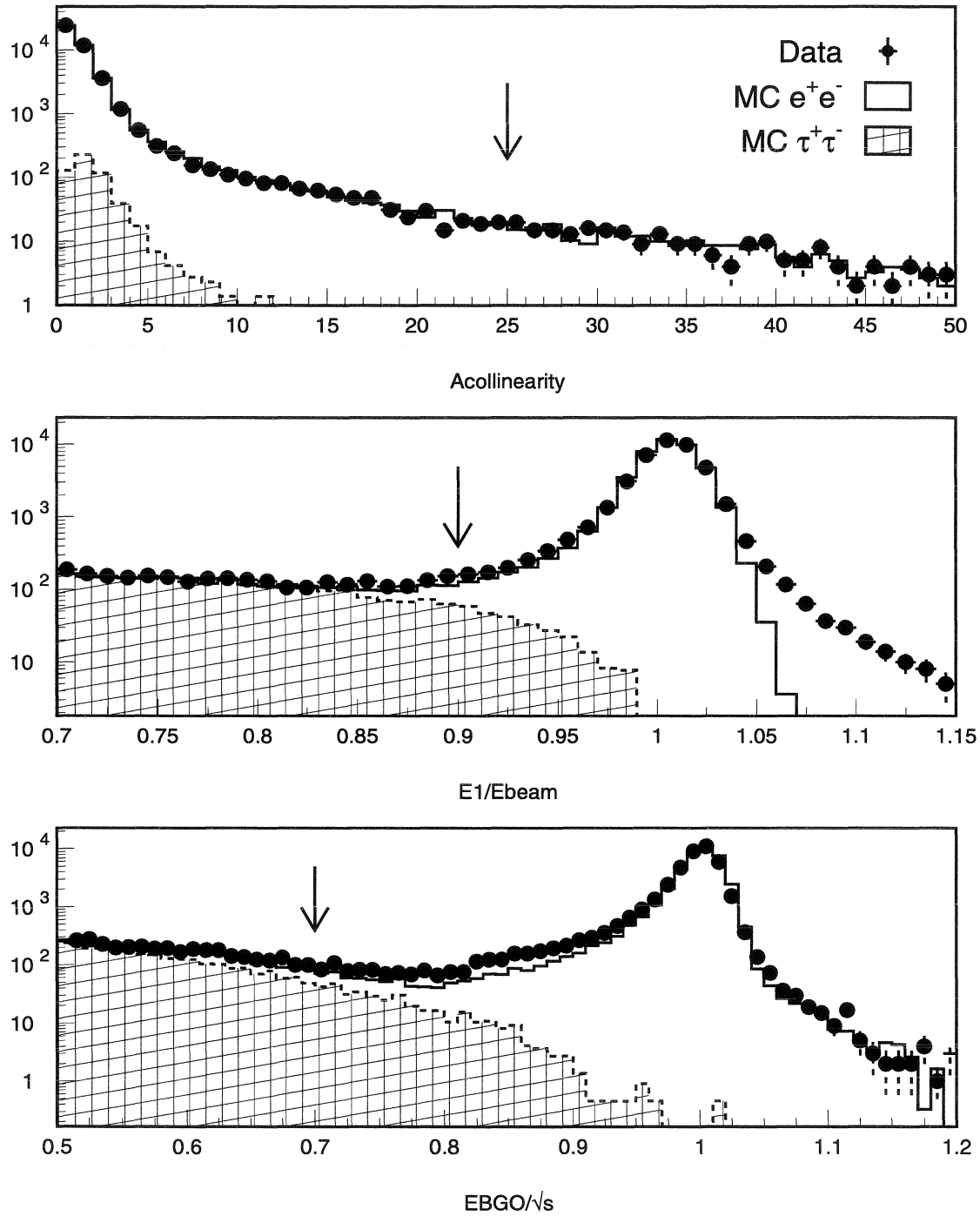

Figure 5.7: Distributions of the main selection variables: acollinearity ζ, the energy of the most energetic BGO BUMP E_1 and E_{BGO}, the sum of the energies of up to four most energetic bumps.

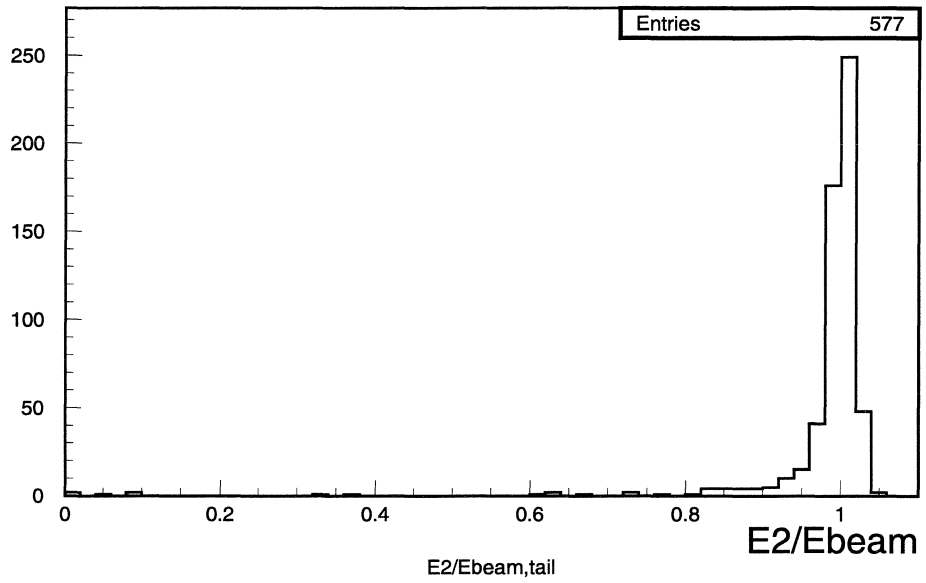

Figure 5.8: The distribution of E_2 for the events with $E_1/E_{beam} > 1.05$.

Events where one of the two electrons deposits about $20\% - 40\%$ lower energy in the electromagnetic calorimeter are populated at $0.8 < E_{BGO} < 0.9$. The imperfection of simulation of the BGO gaps results in a slight discrepancy between data and Monte Carlo prediction at $0.8 < E_{BGO} < 0.9$ in the E_{BGO} plot.

There are about 0.4% of the total events that have substantial leak of energy ($> 95\%$) through the gaps between crystals. The signatures of these events are: on one side there exists one very energetic bump ($E_1 > 0.9E_{beam}$); on the opposite side, there is very little energies deposited in the electromagnetic calorimeter ($E_2 < 2$ GeV) but a large amount of energy deposited in the hadron calorimeter ($E_{HCAL} > 7.5$ GeV). Therefore, these events, named as *mono-bhabha events*, are recovered by the following selection:

- $E_1 > 0.9E_{beam}, E_2 < 2$ GeV and the energy deposit on the opposite side of the most energetic bump in the hadron calorimeter is at least 7.5 GeV.

Figure 5.9 shows the impact point at a crystal surface on the opposite side of the

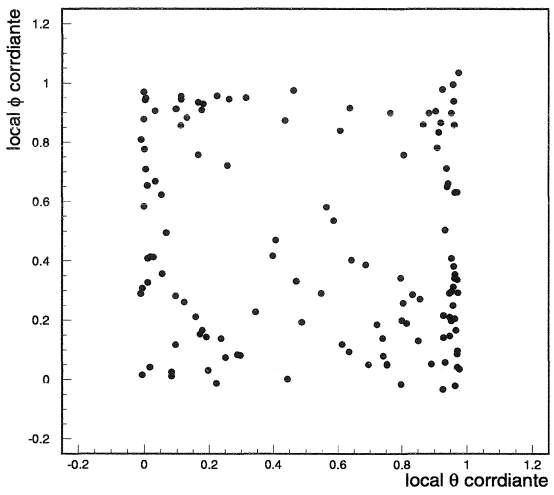

Figure 5.9: Calculated impact points normalized to a crystal surface on the opposite side of the leading bump for the mono-bhabha events.

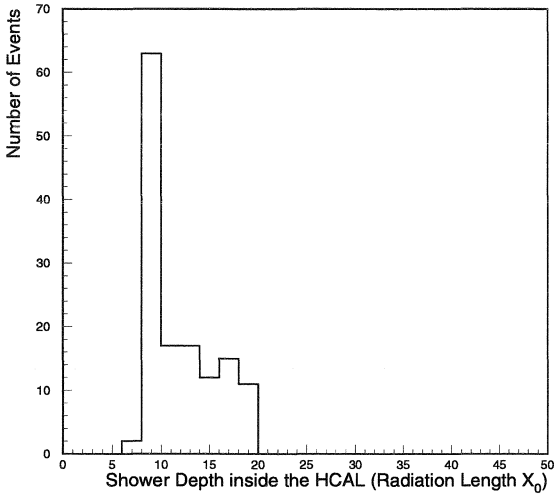

Figure 5.10: The shower depth in the hadron calorimeter for the mono-bhabha events in units of radiation length X_0.

leading bump for the mono-bhabha events. The fact that the population is mostly at the edge of a crystal supports the hypothesis for the mono-bhabha events. Figure 5.10 proves that the energy leaking into the hadron calorimeter has a electromagnetic-like profile in depth. The shower depth is peaked at about 9 radiation lengths (0.35 nuclear interaction lengths) out of the total 99 radiation lengths (3.5 nuclear interaction lengths) for HCAL, which is typical for the electromagnetic energy deposition shape. The shower depth for a hadronic energy deposition is much deeper ($>$ 1 nuclear interaction length.)

5.2 Cross Section Measurement

The cross section for a given type of events (signal) is through the relation

$$\sigma_{signal} = \frac{N_{signal} - N_{bg}}{\varepsilon_{trig}\varepsilon_{signal}\mathcal{L}}, \tag{5.2}$$

where:

N_{signal} is the measured number of events of the signal;

N_{bg} is the measured number of background events;

ε_{trig} is the trigger efficiency;

ε_{signal} is the signal selection efficiency;

$\mathcal{L}$ is the integrated luminosity used for the measurement.

In the case of the measurement for this thesis, the signal is $e^+e^- \rightarrow e^+e^-(n\gamma)$, the main background is $e^+e^- \rightarrow \tau^+\tau^-$. The selection of the BHABHA events, the TEC-based selection, have been presented in detail in the previous section.

5.2.1 Selection Efficiency and Background Estimation

The selection efficiency is estimated using the so-called *real detector simulation.* During event reconstruction for the real detector simulation, a time and date is assigned to a generated event according to the correctly weighted luminosity. The detector status for the time and date are retrieved from the database such that the time-dependent imperfections of the detector response, such as malfunctional BGO crystals/rings or inefficient TEC wires/sectors, are simulated. The real detector simulation has ensured a precise estimate of the selection efficiency.

The Monte Carlo used to study the e^+e^- signal is BHAGENE [36]. $\tau^+\tau^-$ background, typically with a 1.5% contamination, is examined using KORALZ [40]. The typical topology of $\tau^+\tau^-$ background is: both τ leptons ($\tau^\pm$) decay to $e^\pm$, or one of the τ leptons decays to $\pi^\pm\pi^0$. Since the selected data samples only contain 1.5% $\tau^+\tau^-$ background, and the acceptance for $\tau^+\tau^-$ decays is known at the level of 1%, therefore, the systematic error induced by the $\tau^+\tau^-$ background is dominated by the statistics of the Monte Carlo simulations, which can be well controlled to be $< 0.1\%$.

The background from Z decaying to hadrons is well suppressed by the low multiplicity cut: $N_{BUMP} < 15$, since a typical $q\bar{q}$ event has much higher multiplicity

	93a	P-2	93s	P+2	94
Data					
N_{data}	5267	4610	9834	3610	43300
e^+e^-					
N_{gen}	82626	25792	89078	45181	132561
N_{sel}	81412	25114	87060	44340	129875
$\varepsilon_{e^+e^-}$	0.9853	0.9737	0.9773	0.9814	0.9797
$\Delta\varepsilon_{e^+e^-}$	0.0004	0.0010	0.0005	0.0006	0.0004
$\tau^+\tau^-$					
N_{gen}	27906	21519	30094	21378	130572
N_{sel}	286	218	328	204	1219
$\varepsilon_{\tau^+\tau^-}$	0.0102	0.0101	0.0109	0.0095	0.0093
$\Delta\varepsilon_{\tau^+\tau^-}$	0.0006	0.0007	0.0006	0.0007	0.0003

Table 5.5: Results of selection efficiencies and data sample selected with the TEC-based selection.

($N_{BUMP} \gg 20$). The background from two photon process $e^+e^- \rightarrow e^+e^-e^+e^-$ has very low energy deposition in the ECAL barrel, and hence is rejected by the energy cut. The resulting background contaminations from hadronic Z decays and two-photon processes $e^+e^- \rightarrow e^+e^-e^+e^-$ are less than 0.1%; therefore, the systematic errors coming from these backgrounds are negligible.

The selection efficiency ε is in general

$$\varepsilon = \frac{N_{sel}}{N_{gen}}, \tag{5.3}$$

where N_{gen} is the number of events generated, and N_{sel} is the number of events selected with the criteria described above. In the case of e^+e^-, N_{gen} is the number of events generated with $44° < \theta_{e^+e^-} < 136°$ and $\zeta < 25°$.

The statistical error on the efficiency $\Delta\varepsilon$ can be calculated using binomial statis-

	93a	93s	P-2	P+2	94
C_{corr}	1.0002	0.9994	1.0002	1.0013	0.9995
ΔC_{corr}	0.0006	0.0003	0.0008	0.0014	0.0002

Table 5.6: Results of the correction factor C_{corr} with its error ΔC_{corr}.

tics:

$$\Delta\varepsilon = \sqrt{\frac{\varepsilon(1-\varepsilon)}{N_{gen}}}. \tag{5.4}$$

Table 5.5 shows the selection efficiency together with the number of selected events in the data sample using the TEC-based selection described above.

Due to the fact that the TEC inefficiency (ε_{ineff}) is not perfectly simulated in the Monte Carlo, a correction factor to compensate the difference of the TEC inefficiency between the data and the Monte Carlo is introduced as follows:

$$\sigma_{signal} = \frac{N_{signal}/(1-\varepsilon_{data}^{ineff}) - N_{bg}/(1-\varepsilon_{mc}^{ineff})}{\varepsilon_{trig}\varepsilon_{signal}/(1-\varepsilon_{mc}^{ineff})\mathcal{L}} \tag{5.5}$$

$$= \frac{N_{signal}\cdot\ C_{corr} - N_{bg}}{\varepsilon_{trig}\varepsilon_{signal}\mathcal{L}} \tag{5.6}$$

$$C_{corr} = \frac{1-\varepsilon_{mc}^{ineff}}{1-\varepsilon_{data}^{ineff}}. \tag{5.7}$$

Table 5.6 lists the correction factors evaluated from the TEC inefficiency measurements in Table 5.2, which have an average value of 0.9996 ± 0.0001.

5.2.2 Trigger

The large angle BHABHA events are triggered by the logic OR of the energy trigger and the TEC trigger. Assuming that both triggers are statistically independent of each other and using

(%)	93a	P-2	93s	P+2	94
$\varepsilon_{trig}^{energy}$	99.745 ± 0.071	99.751 ± 0.075	99.700 ± 0.057	99.620 ± 0.105	99.939 ± 0.012
ε_{trig}^{TEC}	97.358 ± 0.220	96.480 ± 0.272	95.668 ± 0.206	95.569 ± 0.345	96.022 ± 0.094
$\varepsilon_{trig}^{comb.}$	99.993 ± 0.011	99.991 ± 0.014	99.987 ± 0.012	99.983 ± 0.022	99.998 ± 0.002

Table 5.7: Results of the trigger efficiencies.

N_{both} : the number of events triggered by both triggers

N_{energy} : the number of events triggered only by the energy trigger

N_{TEC} : the number of events triggered only by the TEC trigger

one can estimate the trigger efficiency through:

$$\varepsilon_{trig}^{energy} = \frac{N_{both}}{N_{TEC}} \tag{5.8}$$

$$\varepsilon_{trig}^{TEC} = \frac{N_{both}}{N_{energy}} \tag{5.9}$$

$$\varepsilon_{trig}^{comb} = \varepsilon_{trig}^{energy} + \varepsilon_{trig}^{TEC} - \varepsilon_{trig}^{energy} \cdot \varepsilon_{trig}^{TEC}, \tag{5.10}$$

where:

$\varepsilon_{trig}^{energy}$: the energy trigger efficiency

ε_{trig}^{TEC} : the TEC trigger efficiency

$\varepsilon_{trig}^{comb.}$: the total trigger efficiency for the combination of the two triggers.

Results of the measured trigger efficiencies are shown in Table 5.7, indicating that the bias due to the trigger inefficiency on the cross section measurement is at the level of 10^{-4}.

5.2.3 Systematic Errors

The main sources of systematic errors on the cross section measurement for $e^+e^- \rightarrow e^+e^-(n\gamma)$ process are:

Selection criteria The systematic errors introduced by the selection criteria are due to imperfect modeling in the simulation and can be estimated by varying the selection cuts around their nominal values. Figure 5.11 shows the influence on the cross section measurement (94 data) arising from variation of the cuts around their nominal value with the estimated systematic error listed.

Selection efficiency estimation The selection efficiencies are estimated using Monte Carlo simulation where a finite number of events generated causes a statistical uncertainty on the determination of the selection efficiencies and increases the systematic uncertainties in the cross section measurement.

Background subtraction The main background $\tau^+\tau^-$ events are modeled by the KORALZ generator. Again, the finite number of the events generated introduces a statistical uncertainty on the determination of the background contamination and induces the systematic uncertainties on the cross section measurement (0.04% - 0.09%). Other background contributions from hadronic Z decays and two-photon processes $e^+e^- \rightarrow e^+e^-e^+e^-$ are negligible, as discussed in Section 5.2.1.

Monte Carlo generator The Monte Carlo generator used for the $e^+e^- \rightarrow e^+e^-(n\gamma)$ modeling is BHAGENE. Comparison of the selection efficiency estimated using BHAGENE with another generator BABAMC gives an estimate of the systematic error (0.1%) due to the modeling in the generator.

TEC inefficiency determination As shown in Figure 5.5, the TEC hit efficiency is not perfectly simulated in the Monte Carlo. To be less dependent on this im-

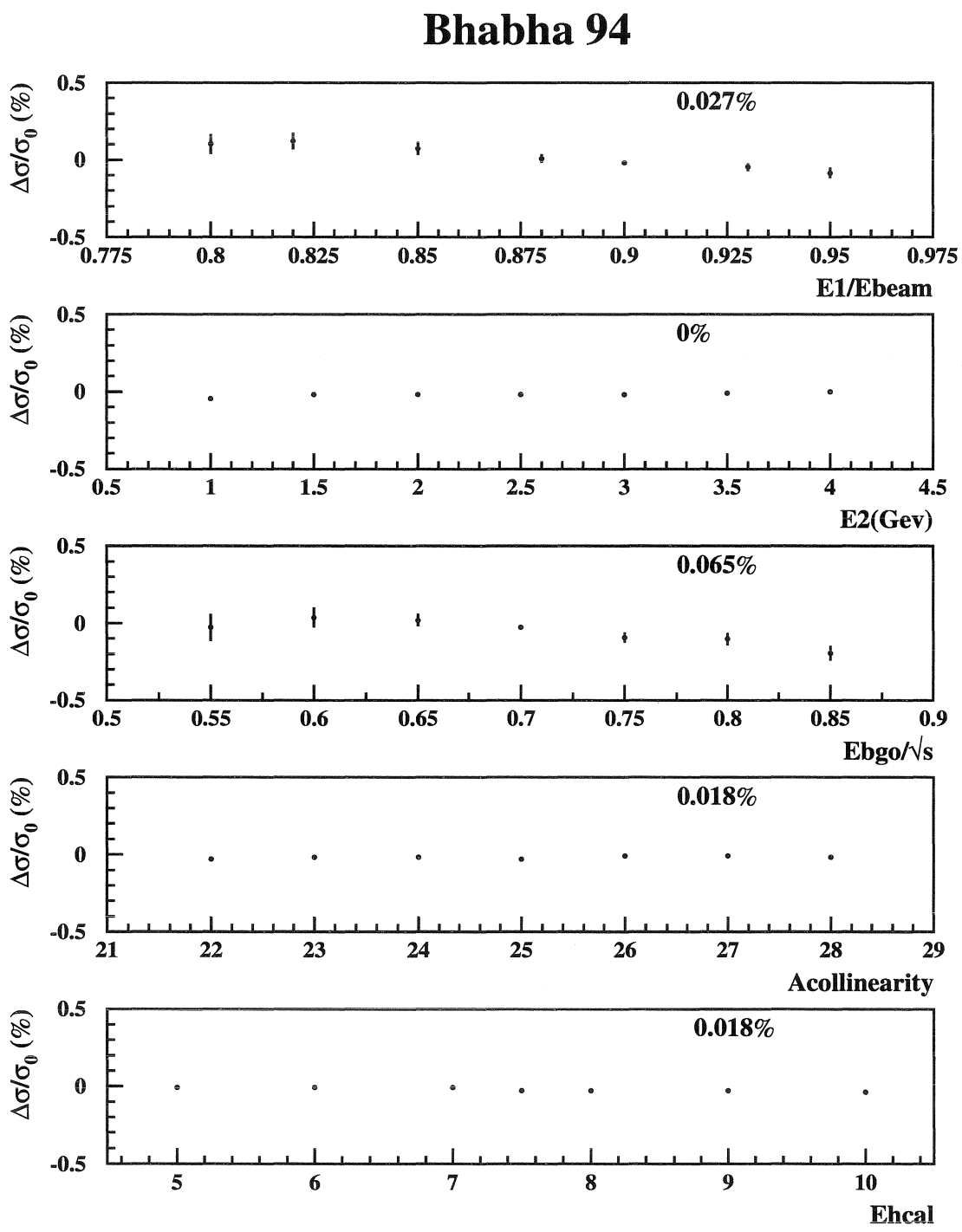

Figure 5.11: The change of the results of the cross section measurement (1994 data) from the variation of the cuts around their nominal value with the estimated systematic error listed.

perfection of Monte Carlo, I measured and then corrected the TEC efficiency for data and Monte Carlo independently. In the previous sections (Section 5.1.3), I have demonstrated that I have determined the TEC inefficiency to the precision of 0.1%, which ensures that the systematic uncertainty on the cross section measurement due to the determination of the TEC inefficiency is at the level of 0.1%.

Geometry The difference in the definition of the polar angle between data and Monte Carlo is less than 0.1°, translating to a systematic error of 0.05% on the cross section measurement.

Beam Spot To check the uncertainty due to the difference in the beam offsets and beam spot shape between data and Monte Carlo, I use two asymmetric data samples. The highest energy cluster has a polar angular region $44° < \theta < 90°$ in the first sample and $90° < \theta < 136°$ in the second sample. The average cross section of the two samples is less sensitive to beam offsets and beam spot size effects. It agrees with the result from the data sample of a symmetric fiducial volume $44° < \theta < 136°$ within 0.05%.

Table 5.8 summarizes the systematic errors from each contribution described above.

5.2.4 Results of the Cross Section Measurement

The results of the cross section measurements are listed in Table 5.9, while the comparisons with the predictions from analytical calculations using ALIBABA program are shown in Figure 5.12 where good agreement can be observed. A brief summary of ALIBABA can be found in Appendix D.

$\delta\sigma/\sigma$ (%)	93a	P-2	93s	P+2	94
Selection criteria	0.24	0.18	0.16	0.27	0.08
Selection efficiency	0.04	0.10	0.05	0.06	0.04
Background subtraction	0.09	0.07	0.09	0.10	0.04
TEC inefficiency	0.1	0.1	0.1	0.1	0.1
Generator	0.1	0.1	0.1	0.1	0.1
z vertex	0.05	0.05	0.05	0.05	0.05
Geometry	0.05	0.05	0.05	0.05	0.05
Total	0.30	0.27	0.24	0.33	0.19

Table 5.8: Summary of the systematic errors on the cross section measurement.

	$\mathcal{L}$ (nb^{-1})	$\sqrt{s}$ (GeV)	$N_{e^+e^-}$	σ (nb)
93a	5192.48	91.321	5267	1.014 ± 0.014
P-2	8288.29	89.450	4610	0.566 ± 0.008
93s	9245.53	91.206	9834	1.072 ± 0.011
P+2	8405.32	93.036	3610	0.431 ± 0.007
94	40695.03	91.220	43300	1.072 ± 0.005

Table 5.9: Results of the cross section measurement.

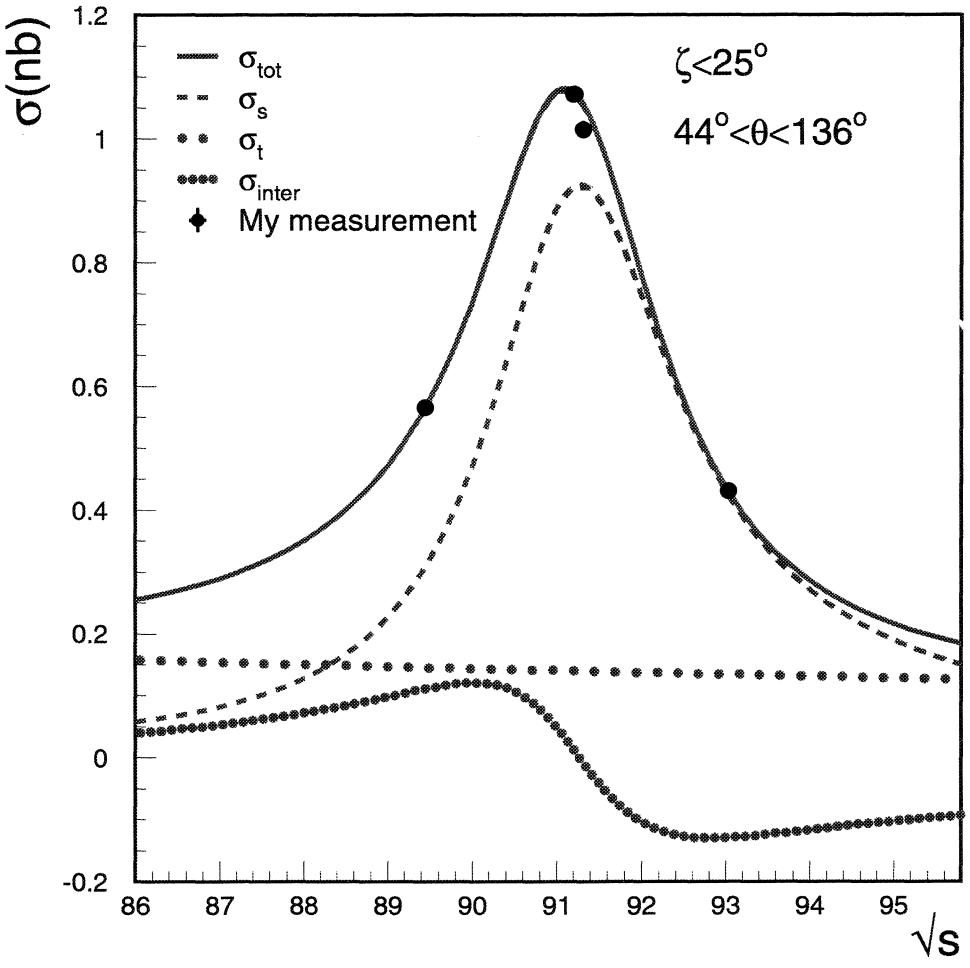

Figure 5.12: Results of the cross section measurements, compared with the predictions from analytical calculation ALIBABA. Good agreement is observed.

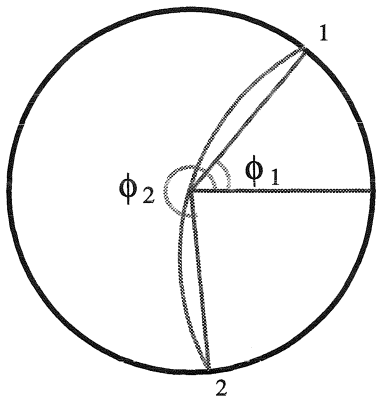

Figure 5.15: Definition of $\Delta\phi$.

$\Delta\phi$ is illustrated in Figure 5.15. Φ is the azimuthal angle of a straight line fit of the track. It also has a correction factor for the $\Delta\phi$'s dependence on the polar angle. In the absence of the magnetic field and radiative photons, $\Delta\Phi$ should be zero. With the magnetic field and the detector geometry in L3, $\Delta\Phi$ is split with two separated peaks, at $\pm$ 1.9 mrad. Again the positive and negative peaks stand for the case (particle 1: e^+, particle 2: e^-) and (particle 1: e^-, particle 2: e^+) respectively.

Figure 5.16 show the $\Delta\Phi$ distribution for the 1994 bc data. More details of the peak value $\overline{\Delta\Phi}$, width $\sigma_{\Delta\Phi}$ and the separation power ($2\overline{\Delta\Phi}/\sigma_{\Delta\Phi}$) for different periods of data taken in 1993 and 1994 are shown in Table 5.11.

		93	94a	94bc
Mean	$\overline{\Delta\Phi}$ $(mrad)$	1.91	1.91	1.91
Width	$\sigma_{\Delta\Phi}$ $(mrad)$	0.70	0.42	0.36
Separation	$2\overline{\Delta\Phi}/\sigma_{\Delta\Phi}$	5.5	9.1	10.6

Table 5.11: The quality of the separator $\Delta\Phi$ for the 1993 and 1994 data.

Typically, both $\Delta\rho$ and $\Delta\Phi$ from 94 data have better separation power than that of the 1993 data as a result of the successful implement of the SMD. The difference

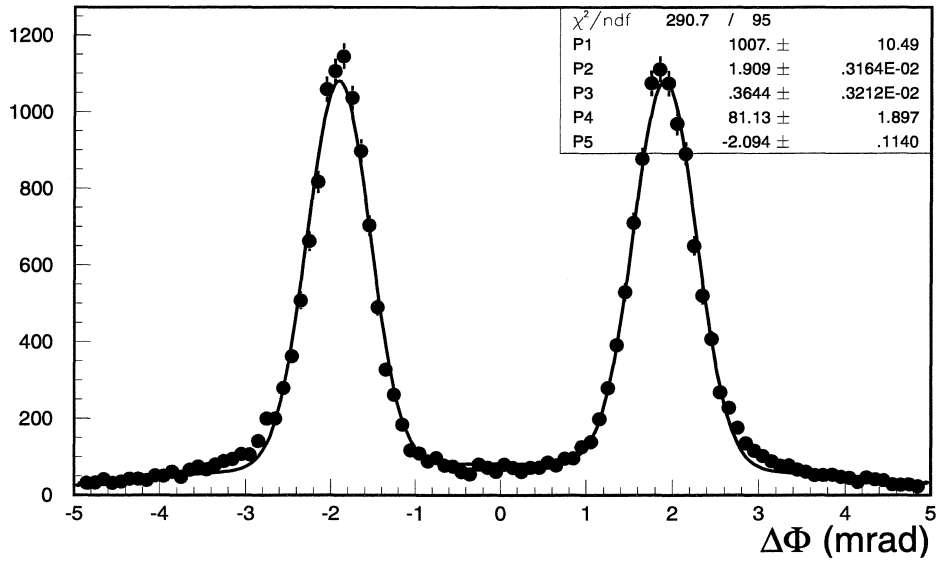

Figure 5.16: Distribution of $\Delta\Phi$ for the 94bc period data sample. The data is fit to a symmetric double gaussian function (P1: normalization, P2: mean value, P3: width) plus a parabolic function $P4 + P5(\Delta\Phi)^2$.

between the 1994a data and the 1994bc data is also observable since the SMD had better efficiency in the 1994bc period.

Due to the excellent angular resolution but relatively low momentum resolution of the tracker, $\Delta\Phi$ has much better separation power than $\Delta\rho$. But the $\Delta\rho$ separator is applied in hard photon radiative events, while the $\Delta\Phi$ separator cannot be used in this case.

Pseudoprobability : $\mathcal{P}$

In order to fully exploit the excellent angular resolution of the tracker while minimizing the sensitivity to photon emission, a method which combines the $\Delta\rho$ and $\Delta\Phi$ separators has been developed, and is employed to determine the electron and positron charge for my forward-backward asymmetry measurement.

As shown in Figure 5.17, events are clustered about two centers $(\frac{\overline{\Delta\rho}}{\sigma_{\Delta\rho}}, \frac{\overline{\Delta\Phi}}{\sigma_{\Delta\Phi}})$ and

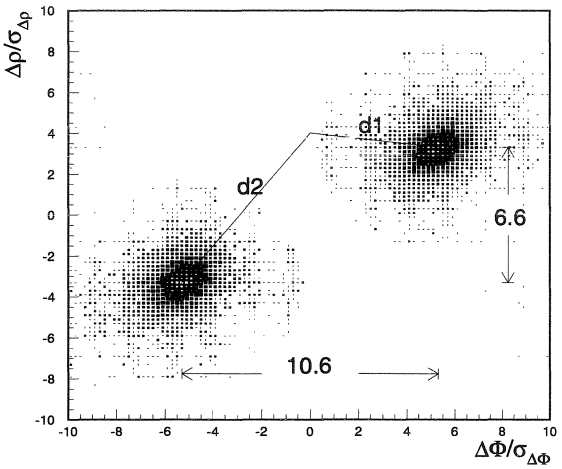

Figure 5.17: Clustering of events from the 1994 bc period in the $\frac{\overline{\Delta\rho}}{\sigma_{\Delta\rho}}$ vs. $\frac{\overline{\Delta\Phi}}{\sigma_{\Delta\Phi}}$ plane. The separation power for $\Delta\rho$ and $\Delta\Phi$ is 6.6σ and 10.6σ respectively.

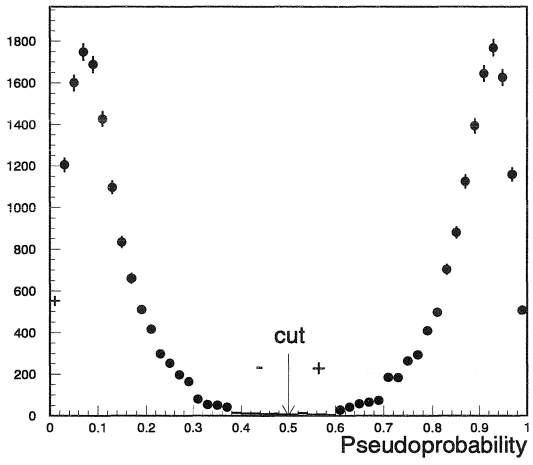

Figure 5.18: Distribution of *Pseudo-probability* $\mathcal{P}$ for the data from the 1994 bc period.

$(-\frac{\overline{\Delta\rho}}{\sigma_{\Delta\rho}}, -\frac{\overline{\Delta\Phi}}{\sigma_{\Delta\Phi}})$. We define d_1 and d_2 as the distance to the two centers:

$$d_1 = \sqrt{(\frac{\Delta\Phi - \overline{\Delta\Phi}}{\sigma_{\Delta\Phi}})^2 + (\frac{\Delta\rho - \overline{\Delta\rho}}{\sigma_{\Delta\rho}})^2} \tag{5.16}$$

$$d_2 = \sqrt{(\frac{\Delta\Phi + \overline{\Delta\Phi}}{\sigma_{\Delta\Phi}})^2 + (\frac{\Delta\rho + \overline{\Delta\rho}}{\sigma_{\Delta\rho}})^2}. \tag{5.17}$$

In the case of radiative photon events, selected by using the criterion $|\Delta\phi| > 3.5$ mrad (for the 1993 data, $|\Delta\phi| > 4$ mrad), only the $\Delta\rho$ separator is used:

$$d_1 = \frac{\Delta\rho - \overline{\Delta\rho}}{\sigma_{\Delta\rho}} \tag{5.18}$$

$$d_2 = \frac{\Delta\rho + \overline{\Delta\rho}}{\sigma_{\Delta\rho}}. \tag{5.19}$$

Events with $d_1 > 5$ and $d_2 > 5$ are rejected to ensure the quality of the charge

determination.

A new parameter *Pseudoprobability* $\mathcal{P}$ is introduced as follows:

$$\mathcal{P} = \frac{d_1}{d_1 + d_2}. \tag{5.20}$$

The distribution of $\mathcal{P}$ is shown in Figure 5.18. Two peaks are clearly separated with $\mathcal{P} > 0.5$ for the case (particle 1: e^+, particle 2: e^-) and $\mathcal{P} < 0.5$ for the case (particle 1: e^-, particle 2: e^+) respectively.

Charge confusion

Charge confusion, the probability to measure the charge incorrectly, can be determined by applying the same charge determination techniques to the $\mu^+\mu^-$ sample, using the fact that the charge of a muon is well measured by the muon chamber. The $\mu^+\mu^-$ sample used for this analysis is selected in a fashion similar to the TEC-selection for the e^+e^- events. The momenta of the muon tracks are substituted for the energies of BGO bumps. An additional requirement that at least one track has three P (precision) segments in the muon chamber is imposed to ensure the good determination of the muon charges.

Table 5.12 shows results on the charge confusion determined from the selected $\mu^+\mu^-$ sample with the $\mathcal{P}$ separator. Again, 1994 data, especially the 1994 bc data,

		93	94a	94bc
full sample	$N_{\mu^+\mu^-}$	11229	3817	12405
full sample	$\mathcal{C}$ (%)	4.64 ± 0.20	1.94 ± 0.22	0.96 ± 0.07
clean sample	$N_{\mu^+\mu^-}$	10276	3541	15501
clean sample	$\mathcal{C}$ (%)	2.77 ± 0.16	0.93 ± 0.16	0.42 ± 0.05

Table 5.12: Charge confusion determined from $\mu^+\mu^-$ samples using *Pseudo-probabilty* technique.

shows a much lower charge confusion than the 1993 data, profiting from the implementation of the SMD. As expected, the clean sample has less charge confusion than the full sample since the clean sample is obtained with an additional cut that rejects events in the anode/cathode region of the TEC.

The charge confusion measured is used as a correction for the determination of the forward-backward asymmetry $A_{\rm FB}$ shown in Section 5.3.3.

5.3.3 Determination of Forward-Backward Asymmetry

To determine the forward-backward asymmetry, the following aspects need to be taken into account:

Scattering Angle

After the charge is determined, we need to choose the convention for the scattering angle. We have three options:

- the scattering angle of the e^- with respect to the electron beam axis: θ_{e^-};
- the scattering angle of the e^+ with respect to the positron beam axis: θ_{e^+};
- $\theta^\star$ which uses information of both θ_{e^-} and θ_{e^+}:

$$\cos\theta^\star = \frac{\sin(\theta_{e^-} + \theta_{e^+})}{\sin\theta_{e^-} + \sin\theta_{e^+}}. \tag{5.21}$$

$\theta^\star$ is the scattering angle in the reduced center-of-mass-energy frame.

The θ_e angle is determined by the polar angle for the center of gravity of the BGO BUMP that matches with the charged tracks of e^- and e^+.

In theory, the first two options are equivalent and the third option is a good approximation to the first two; but experimentally, these three options introduce different systematic errors.

Two approaches have been used to determine $A_{\rm FB}$:

- $A^{\pm}_{\rm FB}$: Take an average of $A^{e^-}_{\rm FB}$ and $A^{e^+}_{\rm FB}$ where $A^{e^-}_{\rm FB}$ uses $\cos\theta_{e^-}$ and $A^{e^+}_{\rm FB}$ uses $\cos\theta_{e^+}$ as the scattering angle. This method reduces the sensitivity to the beam spot size and offset. Assuming that due to the beam spot size and offset, there are ΔN events which are wrongly assigned to the forward/backward region:

$$\begin{aligned} N_F^{\pm} &= N_F^{real} \pm \Delta N \\ N_B^{\pm} &= N_B^{real} \mp \Delta N \\ A^{\pm}_{\rm FB} &= \frac{N_F^{\pm} - N_B^{\pm}}{N_F^{\pm} + N_B^{\pm}} \\ &= A^{real}_{\rm FB} \pm \frac{2\Delta N}{N_F^{real} + N_B^{real}} \\ A^{real}_{\rm FB} &= \frac{A^{+}_{\rm FB} + A^{-}_{\rm FB}}{2}. \end{aligned}$$

- $A^{\star}_{\rm FB}$: Use $\cos\theta^{\star}$ as the scattering angle which minimizes the sensitivity to photon emission.

The difference between the two approaches are due to radiative corrections, which has been checked with Monte carlo and is found to be less than 0.0005. Both approaches have been used to measure the asymmetry $A_{\rm FB}$, and the comparison of their results provides an estimate of the systematic error for the measurements.

Charge Confusion

For an ideal detector without charge confusion, the asymmetry determination is straightforward:

$$A^{real}_{\rm FB} = \frac{N_F - N_B}{N_F + N_B}. \tag{5.22}$$

Due to the existence of charge confusion, $\mathcal{C}$,

$$N_F^{observed} = N_F(1-\mathcal{C}) + N_B\mathcal{C} \tag{5.23}$$

$$N_B^{observed} = N_B(1-\mathcal{C}) + N_F\mathcal{C}; \tag{5.24}$$

therefore,

$$A_{\rm FB}^{observed} = \frac{N_F^{observed} - N_B^{observed}}{N_F^{observed} + N_B^{observed}} \tag{5.25}$$

$$= A_{\rm FB}^{real}(1-2\mathcal{C})\,. \tag{5.26}$$

Hence the correction to the observed asymmetry due to the charge confusion is:

$$A_{\rm FB}^{real} = \frac{A_{\rm FB}^{observed}}{1-2\mathcal{C}}\,. \tag{5.27}$$

This correction leads to an error on $A_{\rm FB}$

$$\delta A_{\rm FB} = \frac{2\delta\mathcal{C}\cdot A_{\rm FB}^{observed}}{1-2\mathcal{C}}\,. \tag{5.28}$$

Background

After the selection for $A_{\rm FB}$ measurement, the main background is from the process of $e^+e^- \to \tau^+\tau^-$. The correction to $A_{\rm FB}$ coming from the $\tau^+\tau^-$ background can be derived as follows:

$$N_F^{observed} = N_F - N_F^{\tau} \tag{5.29}$$

$$N_B^{observed} = N_B - N_B^{\tau} \tag{5.30}$$

$$A_{\rm FB}^{observed} = \frac{(N_F - N_F^{\tau}) - (N_B - N_B^{\tau})}{(N_F - N_F^{\tau}) + (N_B - N_B^{\tau})} \tag{5.31}$$

$$= \frac{A_{\rm FB}^{real} - \varepsilon_\tau A_{\rm FB}^{\tau}}{1-\varepsilon_\tau}. \tag{5.32}$$

Here ε_τ is the selection efficiency for the $\tau^+\tau^-$ background with a typical value of 0.47% for the BGO-based selection plus the two charged track requirements. $A^\tau_{\rm FB}$ is the forward-backward asymmetry for the process of $e^+e^- \to \tau^+\tau^-$. The correction $\Delta A_{\rm FB}$ is found to be:

$$\Delta A_{\rm FB} = A^{observed}_{\rm FB} - A^{real}_{\rm FB} \quad (5.33)$$

$$= \frac{(A^{real}_{\rm FB} - A^{\tau}_{\rm FB})\varepsilon_\tau}{1-\varepsilon_\tau} \quad (5.34)$$

$$\approx (A^{observed}_{\rm FB} - A^{\tau}_{\rm FB})\varepsilon_\tau. \quad (5.35)$$

This correction is small ($< 0.1\%$) for $\sqrt{s} \geq M_Z$, but relatively large for the off-peak point $\sqrt{s} = 88.9$ GeV, where $A^\tau_{\rm FB}$ is negative and the difference between $A^e_{\rm FB}$ and $A^\tau_{\rm FB}$ is large. It results in a correction of 0.002 for $A_{\rm FB}$ at $\sqrt{s} = 88.9$ GeV.

Track efficiency

The track efficiency is determined using the very collinear BHABHA events with acollinearity less than 1° and the energy of the most two energetic bumps at least 30 GeV. The typical track efficiency is 86% for 1993 and 1994.

One can observe that the track efficiency is lower around $\theta = 90°$. This is due to the fact that at $\theta = 90°$, the tracks have maximal transverse momenta P_T or smallest curvatures, which corresponds to the worst P_T resolution.

Results shown in Figure 5.19 are fitted with $P1 + P2 \cdot \cos\theta$, where P2 has a value of -0.00005, indicating that asymmetry of the track efficiency in $\cos\theta$ is negligible for the $A_{\rm FB}$ measurement.

Results

After the corrections for the charge confusion and $\tau^+\tau^-$ background are applied, four sets of results (Table 5.13) for the $A_{\rm FB}$ measurement from 93/94 data have been

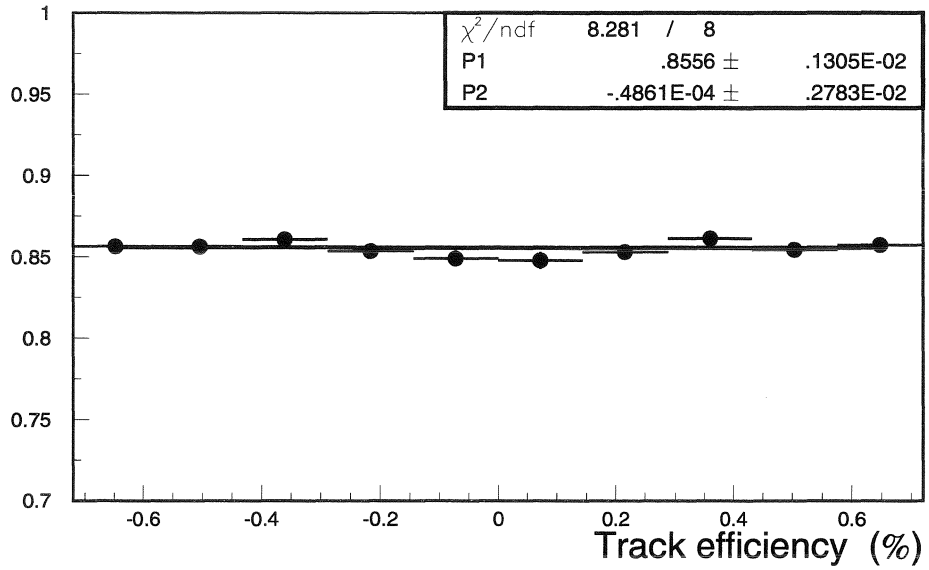

Figure 5.19: θ distribution of track efficiency for data taken in the 1994 b and c periods. A fit to $P1 + P2 \cdot \cos\theta$ indicates that the track efficiency is symmetric in θ.

obtained using two approaches ($A^{\star}_{\rm FB}$ and $A^{\pm}_{\rm FB}$) each of which has been applied to two data samples (full sample and clean sample).

	full sample			clean sample		
	$N_{e^+e^-}$	$A^{\star}_{\rm FB}$	$A^{\pm}_{\rm FB}$	$N_{e^+e^-}$	$A^{\star}_{\rm FB}$	$A^{\pm}_{\rm FB}$
93a	4009	0.083 ± 0.016	0.085 ± 0.016	3763	0.083 ± 0.017	0.085 ± 0.017
$P-2$	3434	0.311 ± 0.016	0.309 ± 0.016	3224	0.311 ± 0.016	0.310 ± 0.016
93s	7330	0.111 ± 0.012	0.112 ± 0.012	6894	0.114 ± 0.012	0.115 ± 0.012
$p+2$	2679	0.101 ± 0.019	0.099 ± 0.019	2521	0.098 ± 0.020	0.096 ± 0.020
94	31636	0.122 ± 0.006	0.120 ± 0.006	28828	0.119 ± 0.006	0.118 ± 0.006

Table 5.13: Results of the $A_{\rm FB}$ measurements.

The charge confusion $\mathcal{C}$ introduces a systematic error on the $A_{\rm FB}$ measurement from both the statistical and systematic uncertainties on the $\mathcal{C}$ determination. The contributions from the statistical uncertainties of $\mathcal{C}$ has been derived as Eq. 5.28 and are typically 0.0005 (0.001 for the P-2 point). The contributions from the systematic

uncertainties of $\mathcal{C}$ are estimated to be 0.0015, from the comparison of the results from full sample and clean sample. A total error of 0.002 from the charge confusion is assigned conservatively combining both effects.

$A_{\rm FB}^{\star}$ and $A_{\rm FB}^{\pm}$ have different sensitivities to the beam spot (size and offset) and the emission of the radiative photons. A comparison of $A_{\rm FB}^{\star}$ and $A_{\rm FB}^{\pm}$ provides a conservative estimate of 0.0015 as the systematic uncertainty on the $A_{\rm FB}$ measurement caused by these effects.

$\tau^+\tau^-$ background leads to a systematic error of 0.0005 on the $A_{\rm FB}$ measurement.

A summary of the systematic errors for the $A_{\rm FB}$ measurement with 93/94 data are presented in Table 5.14. The systematic errors are small compared to the statistical errors for this measurement.

	δA_{FB}
charge confusion	0.002
$\tau^+\tau^-$ background	0.0005
z vertex width	0.0015
total	0.0025

Table 5.14: Systematic errors of the $A_{\rm FB}$ measurements from 93/94 data.

5.3.4 The Differential Cross Section

Using the charge determination described in the previous sections, I have also measured the differential cross section for the process $e^+e^- \to e^+e^-(n\gamma)$.

The fiducial volume $-0.72 < \cos\theta < 0.72$ is divided into 20 bins. For each bin, the cross section is determined with the track efficiency corrected bin-by-bin. The result is shown in Figure 5.20 together with predictions from ALIBABA. A good agreement between data and ALIBABA prediction is observed. The χ^2 is estimated to be 1.0 - 1.6 for different curves.

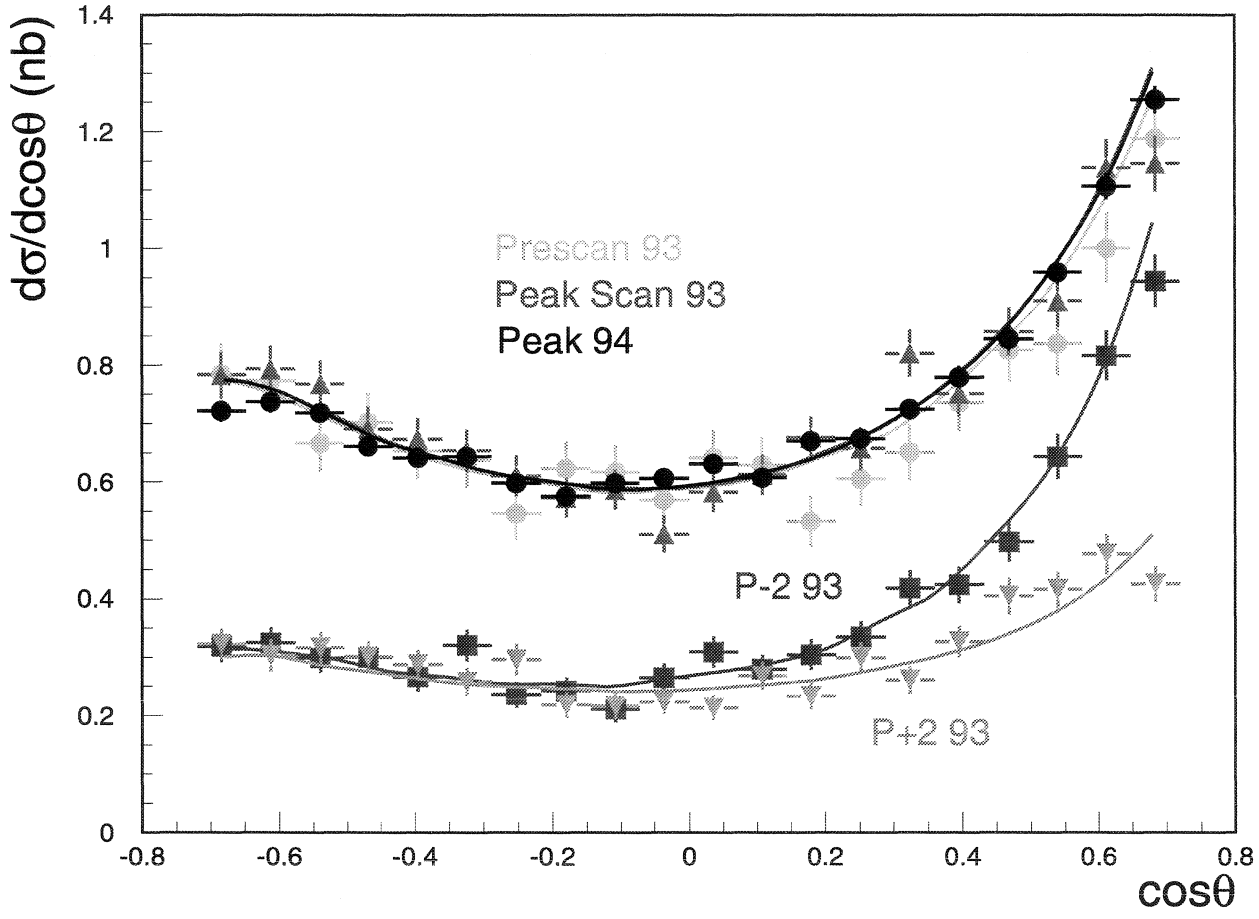

Figure 5.20: Distribution of the differential cross sections.

Chapter 6

Standard Model Parameters and Limits on New Physics

The measurements of the cross section and forward-backward asymmetry for the process $e^+e^- \rightarrow e^+e^-$, presented in Chapter 5, are used in combination with the results from measurements from other $f\bar{f}$ pair productions to evaluate the electroweak parameters, and to provide a global test of the Standard Model.

A short summary of the L3 measurements from all $f\bar{f}$ pair productions is presented in Section 6.1. A special procedure is performed to retrieve the s-channel information from the Bhabha channel such that the results can be compared and combined with that from other channels (Section 6.1.1).

To extract the electroweak parameters, three approaches have been developed which can be classified in two different frameworks:

- **Model Independent Framework** The first two approaches belong to this category which makes a minimum of assumptions about any underlying theory, for example the SM.

  (1) The first approach uses only the total cross section data to determine the properties of the Z boson: the mass M_Z, total decay width Γ_Z and the partial decay width to fermion pairs ($f\bar{f}$), Γ_f (Section 7.3).

  (2) The second approach includes also the measurements on the forward-backward asymmetry, which allows the determination of the coupling constants of the neutral weak current (Section 7.4).

- **Standard Model Framework**

  (3) The third approach evaluates all the data within the framework of the SM to infer valuable information about its fundamental parameters such as the masses of the top quark and the Higgs boson (Section 7.5).

The program ZFITTER [41] is used to calculate the theoretical predictions with the following input parameters [44, 48, 50, 51]:

$$\begin{aligned} M_Z &= 91188.3 \pm 2.9 \text{ MeV} \\ M_t &= 175.6 \pm 5.5 \text{ GeV} \\ M_H &= 300^{+700}_{-240} \text{ GeV} \\ 1/\alpha(M_Z) &= 128.896 \pm 0.090 \\ \alpha_s &= 0.123 \pm 0.006. \end{aligned} \tag{6.1}$$

Electroweak parameters are determined in a χ^2 fit using the MINUIT [45] program. The χ^2 is constructed from the measurements, their errors including the correlations and the analytical calculation. The uncertainties on the luminosity measurement (Appendix A) and the LEP energy determination (Appendix B) are taken into account.

6.1 Fermion Pair Production at the Z Resonance

L3 has measured fermion pair production, $e^+e^- \rightarrow f\bar{f}(\gamma)$, at the Z resonance in the following channels:

$$\begin{aligned} e^+e^- &\rightarrow \text{hadrons}(\gamma) & e^+e^- &\rightarrow e^+e^-(\gamma) \\ e^+e^- &\rightarrow \tau^+\tau^-(\gamma) & e^+e^- &\rightarrow \mu^+\mu^-(\gamma), \end{aligned}$$

where the (γ) indicates the presence of radiative photons.

Table 6.1 is a summary of the data sample, the systematic errors on the luminosity measurement, the systematic errors on the cross section and leptonic forward-backward asymmetry measurements for the data taken at the Z resonance. The electroweak parameters shown in this chapter are determined from the published Z pole data collected up to 1992 [46], the improved measurement of the 1993 and 1994 data and preliminary measurements of the Z resonance scan performed in 1995. The measurements are compared to the fit to all cross section and asymmetry measurements assuming lepton universality in Figure 6.1 and Figure 6.2. Good agreement between the data and the fitting results are observed.

	1990	1991	1992	1993	1994	1995
Data type	7 point scan		Peak only	3 point scan	Peak only	3 point scan
L $[pb^{-1}]$	18.4		22.4	31.7	43.2	19.4
$q\bar{q}$	416 K		678 K	646 K	1307K	311 K
e^+e^-	16 K		22 K	23 K	43 K	12 K
$\mu^+\mu^-$	14 K		21 K	21 K	42 K	9 K
$\tau^+\tau^-$	10 K		15 K	20 K	42 K	7 K
$\delta\mathcal{L}$ [%]	0.6	0.6	0.6	0.15	0.14	0.17
$\delta\sigma$ (had) [%]	0.3	0.15	0.15	0.05	0.05	0.1
$\delta\sigma$ (e) [%]	0.4	0.3	0.3	0.24-0.33	0.19	1.0
$\delta\sigma$ (μ) [%]	0.8	0.5	0.5	0.31-0.32	0.31	1.0
$\delta\sigma$ (τ) [%]	0.9	0.7	0.7	0.64-0.71	0.65	0.6
δA_{FB} (e)	0.004	0.004	0.002	0.0025	0.0025	0.01
δA_{FB} (μ)	0.005	0.002	0.002	0.0008	0.0008	0.005
δA_{FB} (τ)	0.005	0.005	0.003	0.003	0.003	0.003

Table 6.1: Data sample and systematic errors for the luminosity, total cross section and forward-backward asymmetry measurement.

6.1.1 Special Treatment of $e^+e^- \rightarrow e^+e^-(n\gamma)$

As described in Chapter 2, the process $e^+e^- \rightarrow e^+e^-(n\gamma)$ has contributions from s-channel, t-channel and their interference, and is therefore different from other pure s-channel $f\bar{f}$ production. Due to the existence of the t-channel process, the Bhabha

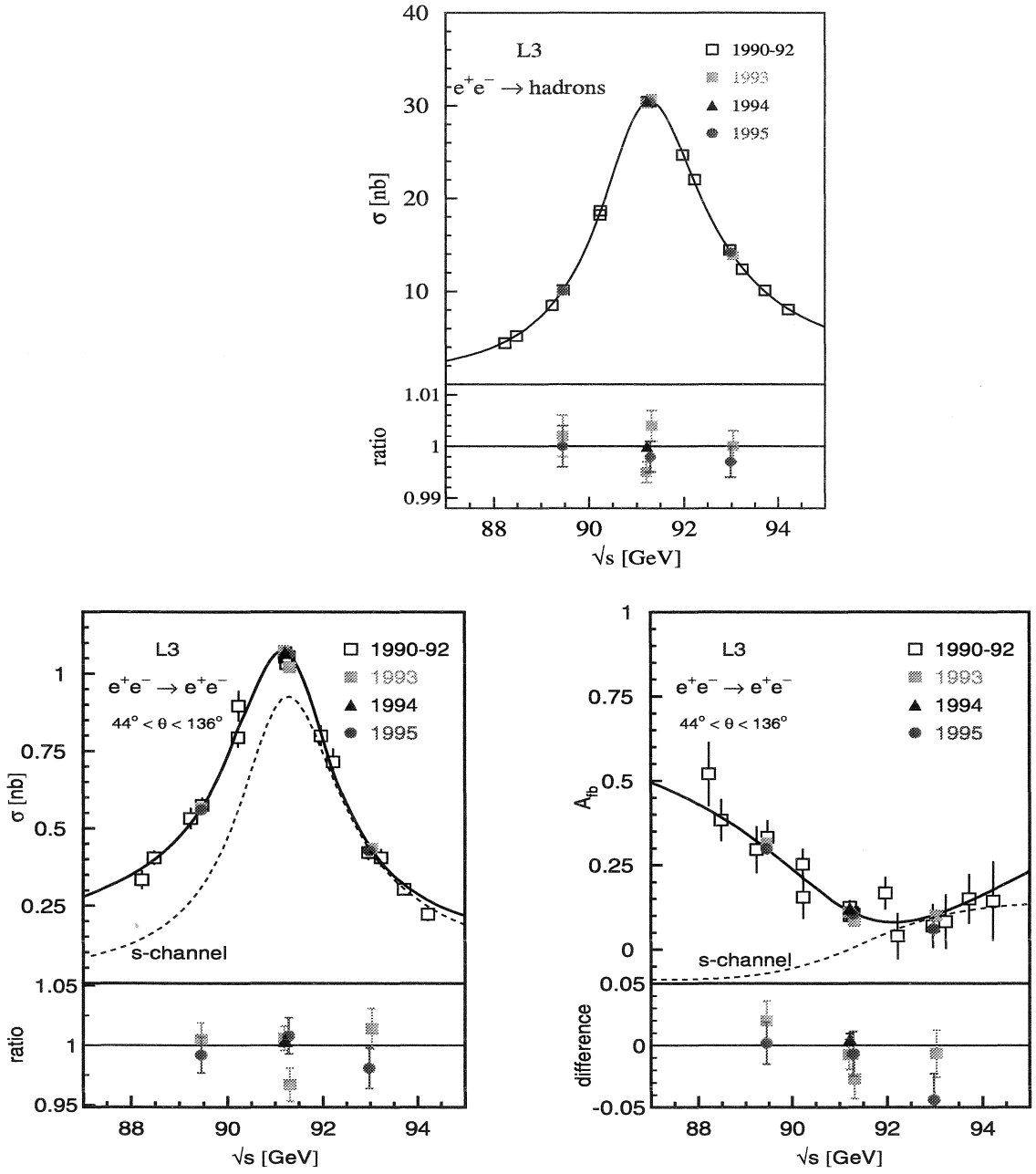

Figure 6.1: The measured cross section and asymmetry as a function of the $\sqrt{s}$. The solid line shows the results of the fit assuming lepton universality. The ratios of the measured cross section and the fit result or the difference between the measured asymmetry and the fit result for the data collected in 1993–95 are shown.

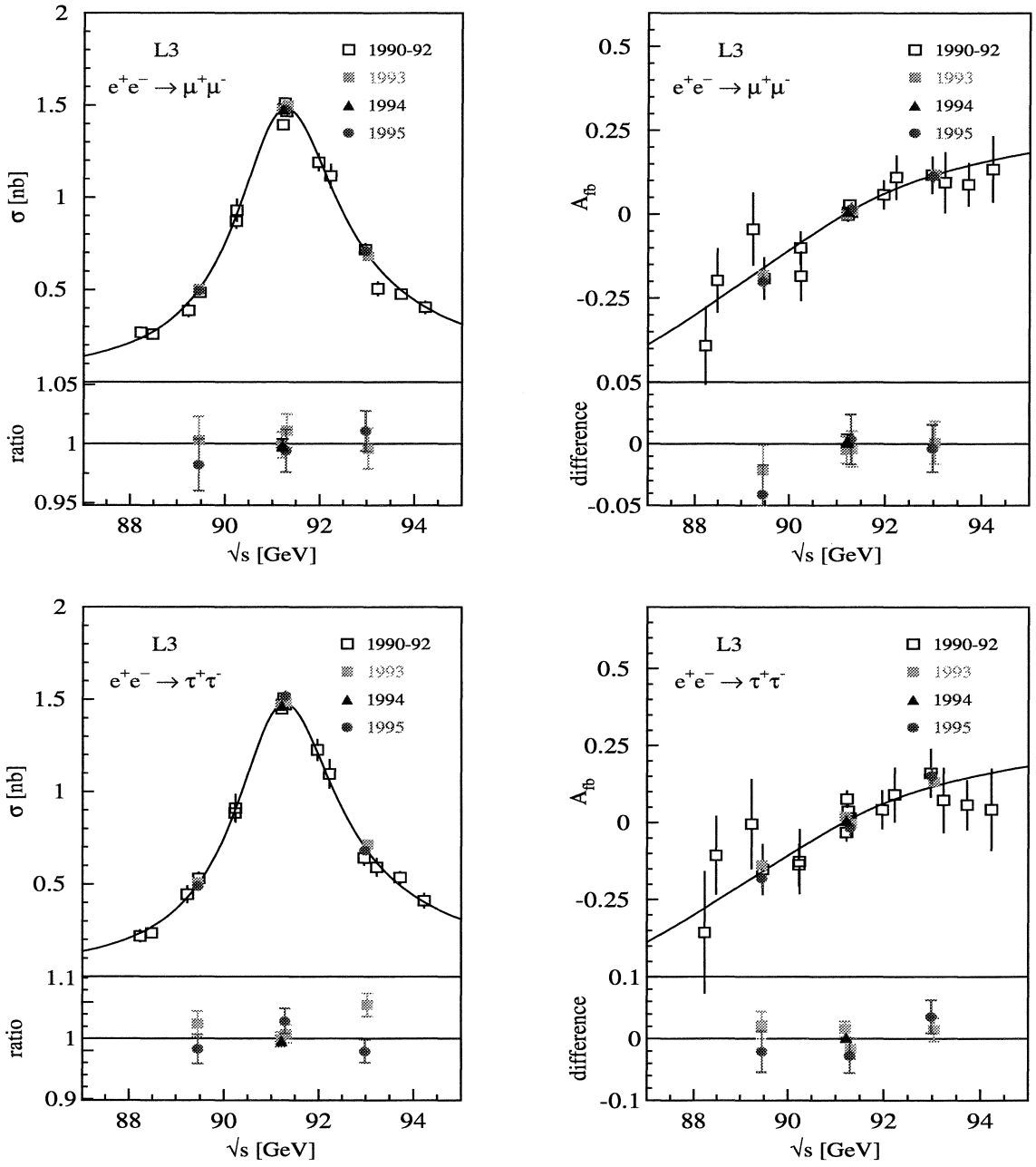

Figure 6.2: The measured cross section and asymmetry as a function of the $\sqrt{s}$. The solid line shows the results of the fit assuming lepton universality. The ratios of the measured cross section and the fit result or the difference between the measured asymmetry and the fit result for the data collected in 1993–95 are shown.

cross section diverges as $\theta \to 0$. This makes it inevitable that the Bhabha cross section needs to be measured within a certain angular region. The angular region adopted by L3 for the Bhabha channel is $44° < \theta_{e^+e^-} < 136°$. The choice of this large angle is to maximize the sensitivity to the Z contribution. To be compared and combined with results from other pure s-channel $f\bar{f}$ production, the results from Bhabha scattering need to have the t-channel and the s/t interference terms subtracted (*t-channel subtraction*), and then to be extrapolated to the full solid angle. This is the theoretical reason that the Bhabha channel needs special treatment.

A technical necessity for this special treatment arises from the fact that the ZFITTER package used for fitting only calculates the s-channel contribution; ALIBABA [42] calculates all the contributions, but is very time consuming and therefore is impractical to be used for fitting.

The procedure to retrieve the s-channel contribution consists of the following steps: first the t-channel + interference ($t + i$) contribution is calculated using ALIBABA and then subtracted from the measured cross section, resulting in an s-channel cross section ($44° < \theta_{e^+e^-} < 136°$). A small detail has to be taken care of that ALIBABA allows angular constraints on both electrons while ZFITTER only allows constraints on one. This is included in the ratio defined as:

$$\mathcal{R} = \frac{\sigma_s^{ALIB}(44° < \theta_{e^+e^-} < 136°)}{\sigma_s^{ZF}(44° < \theta_e < 136°)}. \tag{6.2}$$

ALIB and ZF correspond to the prediction from ALIBABA and ZFITTER respectively. Due to the acollinearity cut, the correction is small. The s-channel cross section can be obtained and further extrapolated to the full solid angle through:

$$\begin{aligned} \sigma_s(44° < \theta_e < 136°) &= (\sigma_{meas} - \sigma_{t+i}^{ALIB})\frac{1}{\mathcal{R}} \\ \sigma_s(4\pi) &= \sigma_s(44° < \theta_e < 136°)\frac{\sigma_s^{ZF}(4\pi)}{\sigma_s^{ZF}(44° < \theta_e < 136°)}. \end{aligned} \tag{6.3}$$

In the same manner, the measured forward-backward can be formulated as:

$$A_{FB} = \frac{(\sigma^{t+i}_{ALIB})_F - (\sigma^{t+i}_{ALIB})_B}{\sigma^s_{ZF}(\mathcal{R} + \frac{\sigma^{t+i}_{ALIB}}{\sigma^s_{ZF}})} + \frac{\mathcal{R}_F(\sigma^s_{ZF})_B - \mathcal{R}_B(\sigma^s_{ZF})_F}{\sigma^s_{ZF}(\mathcal{R} + \frac{\sigma^{t+i}_{ALIB}}{\sigma^s_{ZF}})} + \frac{\mathcal{R}_F + \mathcal{R}_B}{\mathcal{R} + \frac{\sigma^{t+i}_{ALIB}}{\sigma^s_{ZF}}}(A^s_{FB})_{ZF}, \quad (6.4)$$

where

$$\begin{aligned} \mathcal{R}_F &= \frac{\sigma^s_{ALIB}(44^\circ < \theta_{e^-} < 90^\circ, 44^\circ < \theta_{e^+} < 136^\circ)}{\sigma^s_{ALIB}(44^\circ < \theta_{e^-} < 90^\circ, 0^\circ < \theta_{e^+} < 180^\circ)} \\ \mathcal{R}_B &= \frac{\sigma^s_{ALIB}(90^\circ < \theta_{e^-} < 180^\circ, 44^\circ < \theta_{e^+} < 136^\circ)}{\sigma^s_{ALIB}(90^\circ < \theta_{e^-} < 180^\circ, 0^\circ < \theta_{e^+} < 180^\circ)}. \end{aligned} \quad (6.5)$$

Additional systematic errors introduced by this procedure due to ALIBABA's precision, 0.2% for the cross section and 0.002 for the asymmetry, are taken into account in the fit to extract the electroweak parameters.

6.2 Standard Model Parameters

6.2.1 Properties of the Z

The properties of the Z, the mass M_Z, the total decay width Γ_Z and the partial decay width to fermion pairs $f\bar{f}$, Γ_f are determined from a fit to the measured total cross sections. The results are summarized in Table 6.2. Two fits are performed with and without assuming lepton universality, where in the first one a common leptonic partial width Γ_l is defined as the decay width of the Z into a pair of massless charged leptons.

The mass M_Z and total width Γ_Z

The mass M_Z and the total width Γ_Z are mainly determined by the result on the hadronic cross section since the hadron channel has ≈ 10 times the statistics of all

Parameters [MeV]	Treatment of Charged Leptons		Standard Model
	Non-Universality	Universality	
M_Z	91188.3 ± 2.9	91188.3 ± 2.9	—
Γ_Z	2499.8 ± 4.3	2499.8 ± 4.3	2495.9
Γ_{had}	1745.2 ± 5.5	1745.6 ± 4.2	1742.9
Γ_e	83.99 ± 0.26	—	
Γ_μ	83.78 ± 0.47	—	
Γ_τ	84.10 ± 0.62	—	
Γ_l	—	83.98 ± 0.19	83.92
Γ_{inv}	—	502.5 ± 3.4	501.4
N_ν	—	3.001 ± 0.017	3

Table 6.2: Results on the mass and total and partial widths of the Z boson derived from the cross section data. The SM predicition are calculated using input parameters listed in Eq. 6.1.

the lepton channels combined:

$$\begin{aligned} M_Z &= 91188.3 \pm 2.9 \text{ MeV} \\ \Gamma_Z &= 2499.8 \pm 4.3 \text{ MeV} . \end{aligned} \tag{6.6}$$

The error contains both the experimental errors and the uncertainty of the LEP energy calibration. The latter contributions to the total errors on mass and the total width are estimated to be [43]:

$$\begin{aligned} \Delta M_Z(LEP) &= 1.5 \text{ MeV} \\ \Delta \Gamma_Z(LEP) &= 1.4 \text{ MeV}. \end{aligned} \tag{6.7}$$

Leptonic partial width Γ_l

The leptonic partial widths Γ_e, Γ_μ, and Γ_τ obtained are in good agreement with one another, supporting the hypothesis of lepton universality of the neutral weak current. As LEP is an e^+e^- collider, the measured $f\bar{f}$ cross section is proportional to $\Gamma_e\Gamma_f$. Γ_e affects the production of each channel. Therefore, the obtained error on Γ_μ, Γ_τ or Γ_{had} is much larger than that on Γ_e.

Invisible width Γ_{inv} and Number of Neutrinos N_ν

From the cross section data, the invisible width Γ_{inv} is derived as follows:

$$\Gamma_{inv} = \Gamma_Z - \Gamma_{had} - 3\Gamma_l = 502.5 \pm 3.4 \text{ MeV}. \tag{6.8}$$

In the SM, the invisible width is exclusively given by Z decays into neutrinos. Therefore, the number of SM neutrino generations N_ν can be derived as follows:

$$N_\nu = \frac{\Gamma_{inv}}{\Gamma_l}\left(\frac{\Gamma_l}{\Gamma_\nu}\right)^{SM} = 3.001 \pm 0.017. \tag{6.9}$$

Here the SM prediction for the ratio of the Z decay width to the charged leptons and neutrinos $\Gamma_l/\Gamma_{inv} = 0.5022^{+0.0005}_{-0.0004}$ is used where most of the higher order corrections involving M_t and M_H cancel out.

The above results have been verified by the direct measurement of single photon ($e^+e^- \to \nu\nu\gamma$) events. The preliminary results using the L3 data through 1994 is [47]:

$$N_\nu = 2.98 \pm 0.07 \text{ (stat.)} \pm 0.07 \text{ (sys.)}.$$

6.2.2 Electroweak Couplings

In the second approach, the lepton forward-backward asymmetry data are included in addition to the cross section data. Together with τ polarization measurements [52],

the electroweak couplings are determined through the following correlations:

- the partial width of Z decaying to a pair of lepton $l\bar{l}$: $\Gamma_l \propto (\overline{g}^l_{\rm V})^2 + (\overline{g}^l_{\rm A})^2$,
- the lowest order leptonic pole asymmetry : $A^{0,l}_{\rm FB} = \frac{3}{4} A_e A_l$ with $A_l = \frac{2\overline{g}^l_{\rm V}\overline{g}^l_{\rm A}}{(\overline{g}^l_{\rm V})^2+(\overline{g}^l_{\rm A})^2}$,
- τ polarization: $\mathcal{P}_\tau(M_Z{}^2) = -A_\tau$,
- forward-backward τ polarization asymmetry : $\mathcal{P}^{FB}_\tau(M_Z{}^2) = -\frac{3}{4}A_e$.

Using the results from neutrino-electron scattering and the low energy $A_{\rm FB}$ measurements that the axial-vector coupling constant of the electron is negative, the electroweak couplings are determined unambiguously as summarized in Table 6.3. The average vector and axial-vector coupling constants of charged leptons are found to be:

$$\overline{g}^l_{\rm V} = -0.0398^{+0.0027}_{-0.0029}, \qquad \overline{g}^l_{\rm A} = -0.5010 \pm 0.0006. \tag{6.10}$$

Parameter	Treatment of Charged Leptons		Standard
	Non-Universality	Universality	Model
$\overline{g}^e_{\rm A}$	-0.5011 ± 0.0008	—	
$\overline{g}^\mu_{\rm A}$	-0.5006 ± 0.0015	—	
$\overline{g}^\tau_{\rm A}$	-0.5015 ± 0.0019	—	
$\overline{g}^l_{\rm A}$	—	-0.5010 ± 0.0006	-0.5012
$\overline{g}^e_{\rm V}$	-0.0396 ± 0.0034	—	
$\overline{g}^\mu_{\rm V}$	$-0.0374^{+0.0085}_{-0.0079}$	—	
$\overline{g}^\tau_{\rm V}$	-0.0394 ± 0.0032	—	
$\overline{g}^l_{\rm V}$	—	$-0.0398^{+0.0027}_{-0.0029}$	-0.0361

Table 6.3: Results on the effective coupling constants, $\overline{g}^l_{\rm V}$ and $\overline{g}^l_{\rm A}$, derived from the tau polarization, forward-backward asymmetry and cross section data. The SM predicition are calculated using input parameters listed in Eq. 6.1.

Since the lepton forward-backward asymmetry measures the product of $A_e A_l$, the errors on $\overline{g}^l_{\rm V}$ and $\overline{g}^l_{\rm A}$ are the smallest for the e^+e^- channel. The error on $\overline{g}_{\rm A}$ is mainly determined by $\Gamma_{\rm l}$. So the error on $\overline{g}^\tau_{\rm A}$ is still worse than that of $\overline{g}^\mu_{\rm A}$. The error on $\overline{g}^\tau_{\rm V}$ is smaller than that on $\overline{g}^\mu_{\rm V}$, and is due to the contribution of the $\mathcal{P}_\tau$ measurement which measures A_τ. A_τ is much more sensitive to $\overline{g}_{\rm V}$ than to $\overline{g}_{\rm A}$. Therefore, the $\mathcal{P}_\tau$ measurement affects mainly the error on $\overline{g}^\tau_{\rm V}$ and not the error on $\overline{g}^\tau_{\rm A}$.

In Figure 6.3, the 68% C.L. contours show the correlated results on the measured vector and axial-vector coupling constants for charged leptons. The measured vector and axial-vector coupling constants agree among the different types of charged leptons (e, μ, and τ). This supports the hypothesis of lepton universality of the weak neutral current.

Electroweak Mixing Angle

The results on A_l from the measurements of lepton forward-backward asymmetry and of τ polarization are indeed only on the ratios of $\overline{g}_{\rm V}/\overline{g}_{\rm A}$, which can be parameterized through the effective electroweak mixing angle $\sin^2\bar{\theta}_{\rm W}$:

$$\sin^2\bar{\theta}_{\rm W} = \frac{1}{4|{\rm Q_f}|}(1-\frac{\overline{g}_{\rm V}}{\overline{g}_{\rm A}}). \tag{6.11}$$

The results from the cross section and the leptonic asymmetries, the tau-polarization measurements [52] together with the result from the $b\overline{b}$ asymmetry measurement [53] are listed in Table 6.4. The average value of $\sin^2\bar{\theta}_{\rm W}$ is found to be:

$$\sin^2\bar{\theta}_{\rm W} = 0.2304 \pm 0.0009. \tag{6.12}$$

The consistency of the values of $\sin^2\bar{\theta}_{\rm W}$ derived independently from A^{ll}_{FB}, $A^b_{\rm FB}$ [53] and the tau polarization $\mathcal{P}_\tau$ [52] provides an important test of the Standard Model.

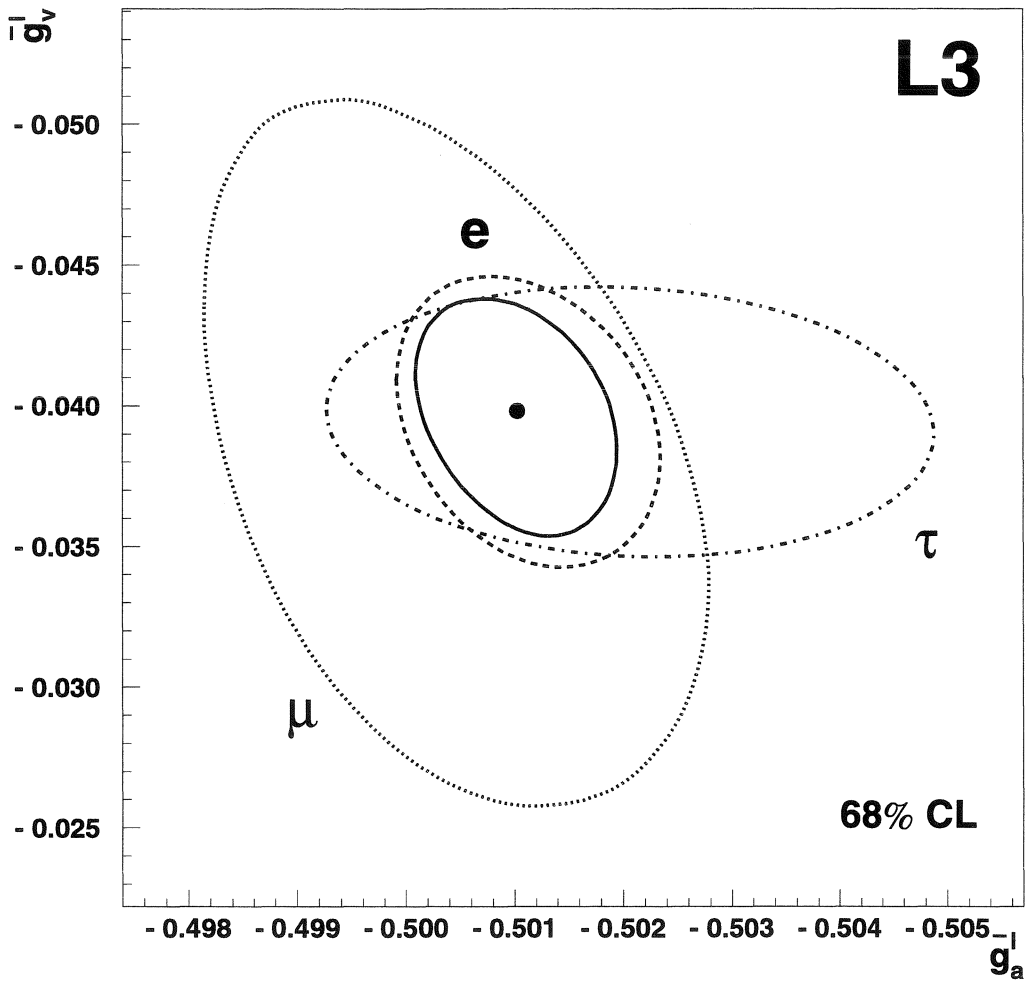

Figure 6.3: Correlation between the effective coupling constants of the neutral weak current, $\overline{g}_{\mathrm{V}}$ and $\overline{g}_{\mathrm{A}}$, for charged leptons. The 68% confidence level contours for the two parameters are shown, for each lepton species separately (dotted contours), and under the assumption of lepton universality (solid contour).

Input Data	$\sin^2\bar{\theta}_W$
A_{FB}^l	0.2301 ± 0.0014
A_e and A_τ	0.2307 ± 0.0013
A_{FB}^b	0.2304 ± 0.0020
Average	0.2304 ± 0.0009

Table 6.4: $\sin^2\bar{\theta}_W$ derived from the leptonic asymmetry, the tau-polarization, and the $b\bar{b}$ asymmetry measurements. The SM prediction is $\sin^2\bar{\theta}_W = 0.2320$.

6.2.3 Constraints on the Standard Model

The precise electroweak measurements performed at L3 have been used to check the validity of the Standard Model, and to infer information about its basic parameters such as M_Z, M_t, M_H and α_s. The fits to these parameters have been carried out in the framework of the Minimal SM, using the complete set of electroweak measurements listed in Table 6.5.

As the precision of the measurements has reached previously unforeseen levels, the theoretical uncertainties in the parameters that determine the "Standard Model predictions" have become increasingly important. One significant theoretical error is in the value of $\alpha(M_Z)$, and is due to an uncertainty in the contribution of light quarks to the hadronic vacuum-polarization in the photon propagator. The $\alpha(M_Z)$ value, $1/(128.896 \pm 0.090)$ [48], is used and the error is propagated in the fits, resulting in an uncertainty of 0.00023 on the Standard Model prediction of $\sin^2\bar{\theta}_W$ and an error of 4 GeV on the fitted value of M_t. Further improvement in the theoretical $\alpha(M_Z)$ predictions requires more precise measurements of e^+e^- cross sections at center of mass energies below 12 GeV in future experiments.

The combined data have been fitted for three fixed values of M_H (60, 300 and

Input Data	Value
cross sections and lepton asymmetries:	
M_Z [GeV]	$91\,188.3 \pm 2.9$
Γ_Z [GeV]	$2\,499.6 \pm 4.3$
σ°_{had} [nb]	41.411 ± 0.074
$\mathcal{R}_l$	20.788 ± 0.066
$A^{0,l}_{FB}$	0.0187 ± 0.0026
τ-polarization [52]:	
A_e	0.156 ± 0.017
A_τ	0.152 ± 0.013
b quark results:	
$R_b(=\frac{\Gamma_b}{\Gamma_Z})$ [56]	0.2185 ± 0.0043
$A^{0,b}_{FB}$ [53]	0.0975 ± 0.0076
$q\bar{q}$ charge asymmetry [54]:	
$\sin^2\bar{\theta}_W(< Q_{FB} >)$	0.2336 ± 0.0019
W boson mass [57] :	
M_W [GeV]	80.87 ± 0.28

Table 6.5: Experimental data used as input for the fit in the Standard Model framework.

1000 GeV), leaving M_t and α_s free to be determined by the data. The results are:

$$\begin{aligned} \alpha_s &= 0.126 \pm 0.006 \pm 0.002 \text{ (Higgs)} \\ M_t &= 187^{+13}_{-14} \pm 16 \text{ (Higgs) GeV}, \end{aligned} \tag{6.13}$$

where the second error expresses the shift in the central values of α_s and M_t for a variation in the mass of the Higgs boson, M_H, from 60 to 1000 GeV around the central value of 300 GeV.

The independent determination of α_s using L3 hadronic event topology and tau decay width data yields $\alpha_s = 0.123 \pm 0.006$ [49]. To obtain the best precision on M_t,

this value of α_s has been used as a constraint in the fit, resulting in a top quark mass:

$$M_t = 189^{+12}_{-13} \pm 17 \text{ (Higgs) GeV.} \quad (6.14)$$

This is in very good agreement with the direct measurements [50, 51]:

$$\begin{aligned} M_t &= 175.7 \pm 5.7 \text{ (stat)} \pm 7.4 \text{ (syst) GeV } (CDF) \\ M_t &= 170 \pm 15 \text{ (stat)} \pm 22 \text{ (syst) GeV } (D0). \end{aligned} \quad (6.15)$$

This agreement supports the prediction of the SM that the bulk of the weak radiative corrections to the electroweak observables is indeed due to the top quark.

From this result, the value of the electroweak radiative corrections Δr (See Eq. 2.237), the mass of the W boson, the on-shell ($\sin^2\theta_W$) and the effective ($\sin^2\bar{\theta}_W$) weak mixing angle are obtained:

$$\begin{aligned} \Delta r &= 0.0338^{+0.0050+0.0005}_{-0.0050-0.0008} \\ M_W &= 80.406^{+0.083+0.012}_{-0.085-0.008} \\ \sin^2\theta_W &= 0.2225 \pm 0.0016 \pm 0.0002 \\ \sin^2\bar{\theta}_W &= 0.23152 \pm 0.00044^{+0.00008}_{-0.00024}. \end{aligned} \quad (6.16)$$

The derived M_W is consistent with the direct measurement at Tevatron [58] and at LEP 200 [57].

Constraining the top mass to the combined value from the direct measurements of D0 and CDF, $M_t = 175.6 \pm 5.5$ GeV, we can use our measurements to derive an estimate and an upper limit of the mass of the SM Higgs boson. Since the main dependence on M_H is logarithmic, the constraints on M_H are still weak with the data sample analyzed. Figure 6.4 shows the 68% C.L. contour in the $M_t - M_H$ plane. The limit on M_H is:

$$\begin{aligned} M_H &= 91^{+230}_{-81}\ \text{GeV} \\ &< 645\ \text{GeV} \qquad 95\%\ C.L. \end{aligned} \tag{6.17}$$

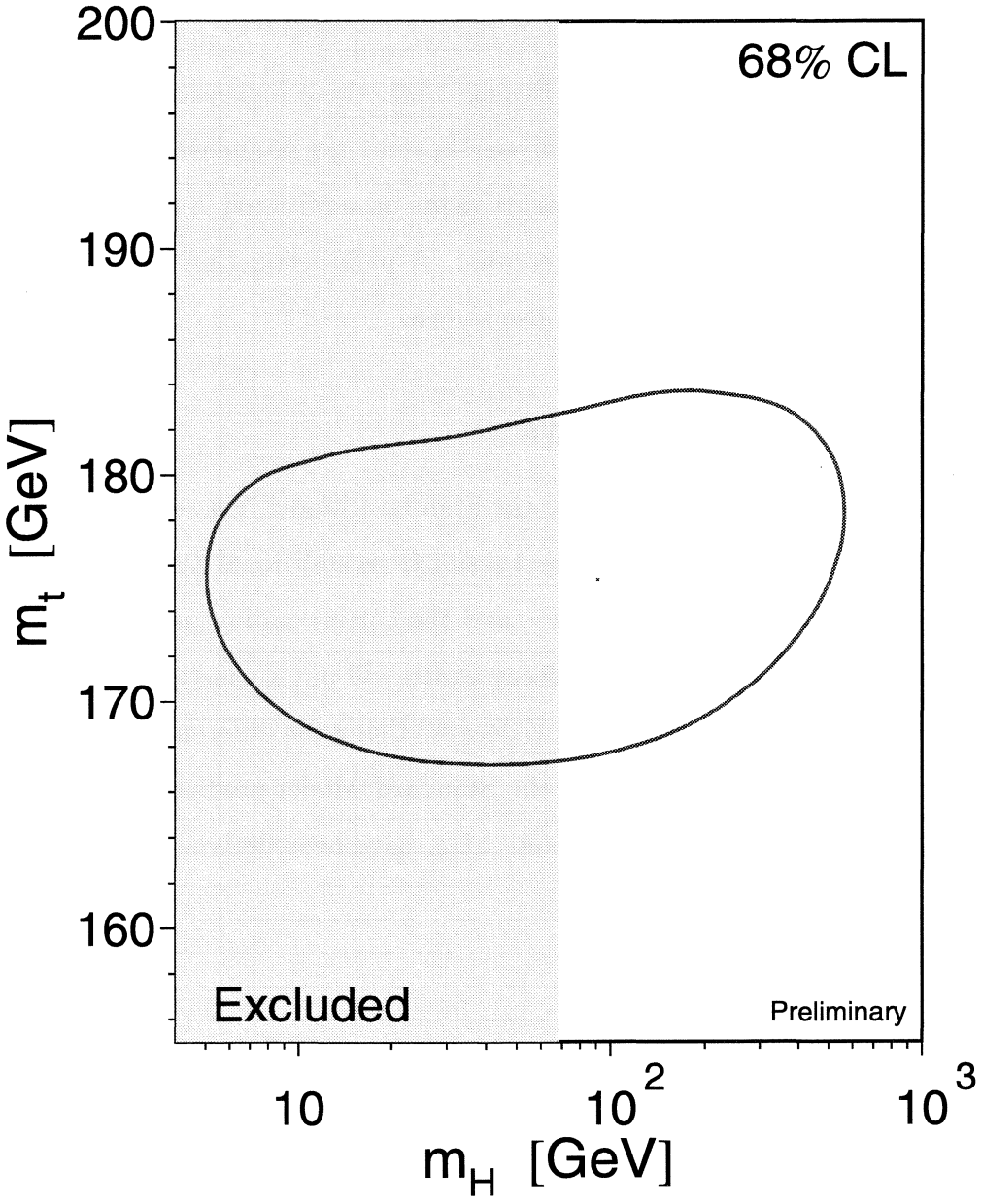

Figure 6.4: Contour in $M_t - M_H$ plane obtained from the SM fit.

6.3 Limits on New Physics

As shown in the previous sections, LEP1 has provided high precision measurements of electroweak parameters and has tested the validity of the Standard Model including higher order radiative corrections. Besides that, these high precision measurements also result in constraints on new physics beyond the Standard Model. In the following, limits from electroweak measurements on additional Z decays and existence of additional Z′ gauge boson are presented. A parametrization of the effects of new physics in the electroweak sector is also shown.

6.3.1 Additional Z Decays

Many models of new physics beyond the Standard Model, *e.g.*, supersymmetry, have predicted additional Z decays. A direct result from additional Z decays is the increase of the total width of the Z boson, Γ_Z and the corresponding partial width Γ_l, Γ_{had}, or Γ_{inv}. A limit on the increased Z decay width will put a constraint on any model of new physics that predicts additional Z decays. Using the difference between the fitted results, shown in Section. 6.2, and the Standard Model prediction, upper limits on additional width contribution $\Delta\Gamma_Z$ and $\Delta\Gamma_{inv}$ have been derived at a 95% confidence level:

$$\begin{aligned} \Delta\Gamma_Z &< 11.3 \text{ MeV} \\ \Delta\Gamma_{inv} &< 7.4 \text{ MeV}. \end{aligned} \tag{6.18}$$

Although the limits from the constraints (6.18) are weaker than those from direct searches, especially those from the direct search at LEP2, the constraints from $\Delta\Gamma_Z$ and $\Delta\Gamma_{inv}$ still serve as an independent check for any model of new physics.

6.3.2 Existence of Z′

Another common feature of many extensions of the Standard Model is the existence of new gauge bosons, such as an additional neutral gauge boson Z′. Two models which are often considered are either based on the superstring inspired broken E6 group as a gauge group, or on a left-right symmetric extension of the Standard Model. In both of these models, the mass eigenstates Z_1 and Z_2 are mixtures of the symmetry eigenstates Z of $SU(2)_L \otimes U(1)_Y$ and Z′ of the additional U(1) (E6 Model) or $SU(2)_R$ groups (Left-Right Model). The mixing is described by a matrix using the mixing angle θ_M:

$$\begin{pmatrix} Z_1 \\ Z_2 \end{pmatrix} = \begin{pmatrix} \cos\theta_M & \sin\theta_M \\ -\sin\theta_M & \cos\theta_M \end{pmatrix} \begin{pmatrix} Z \\ Z' \end{pmatrix}. \tag{6.19}$$

The gauge boson masses m_Z and $m_{Z'}$ are related by the Z-Z′ mixing angle:

$$\tan^2\theta_M = \frac{m_0^2 - m_Z^2}{m_{Z'}^2 - m_0^2}. \tag{6.20}$$

In the absence of mixing, m_0 is the mass of the Z boson in the Standard Model. The resonance observed at LEP1 has mass m_Z (= m_0 in the absence of mixing).

The quantitative consequences of Z-Z′ mixing are:

(1) modifications of the couplings of the Standard Model Z boson,

(2) shift of the mass of the Standard Model Z boson.

The experimental observables such as cross sections and asymmetries will be modified due to the existence of the Z′ gauge boson. By examining these measured quantities in the framework of Z′ models such as the E6 or LR model mentioned above, one can put constraints on the mixing angle θ_M and $m_{Z'}$.

In L3 [60], this is done by using the ZFITTER 4.9 [41] and ZEFIT 4.2 [59] in the framework of the E6 model or LR model. The data inputs are the combined results

from hadronic and leptonic cross sections, leptonic forward-backward asymmetries, τ-polarization, the b-quark forward-backward asymmetry and the partial decay width of the Z boson to b-quarks. No indication for Z′ gauge boson production is seen. The fitted Z-Z′ mixing angle θ_M is compatible with zero for all models considered. Allowed values for θ_M are typically between -0.005 and 0.003 at the 95% C.L. for different models. A Z′ boson with a mass less than $\approx$ 200 GeV is excluded at 95% C.L. for most of the models.

6.3.3 Parametrization of New Physics

The aim for parametrization of new physics is to disentangle new physics from the relatively large correction originating from the masses of the top quark and Higgs boson. One popular parametrization uses the so-called ϵ parameters [61]:

$$\epsilon_1 = \Delta\rho = \frac{3\,G_F m_t^2}{8\,\pi\,\sqrt{2}} - \frac{3\,G_F m_W^2}{4\,\pi^2\sqrt{2}} \tan^2\theta_w \ln(\frac{m_H}{m_Z}) \quad (6.21)$$

$$\epsilon_3 = \frac{G_F\, m_W^2}{12\,\pi^2\sqrt{2}} \ln(\frac{m_H}{m_Z}) - \frac{G_F\, m_W^2}{6\,\pi^2\sqrt{2}} \ln(\frac{m_t}{m_Z}). \quad (6.22)$$

The first parameter ϵ_1 is identical to the deviation of the ρ parameter from unity (See Eq. 2.4.1) which keeps the leading quadratic m_t dependence of weak radiative corrections. The other parameter ϵ_3 is arranged to contain the other effect from m_H and only mild dependence on m_t. Therefore, the effects from m_t and m_H are separated in ϵ_1 and ϵ_3 respectively.

The result of the analysis of the L3 data (Γ_l and $\sin^2\bar{\theta}_W$) in terms of the parameters ϵ_1 and ϵ_3 is shown in Figure 6.5. The central values are:

$$\epsilon_1 = 0.0046 \pm 0.0023 \quad (6.23)$$

$$\epsilon_3 = 0.0017 \pm 0.0031. \quad (6.24)$$

No significant deviation from the Standard Model is observed.

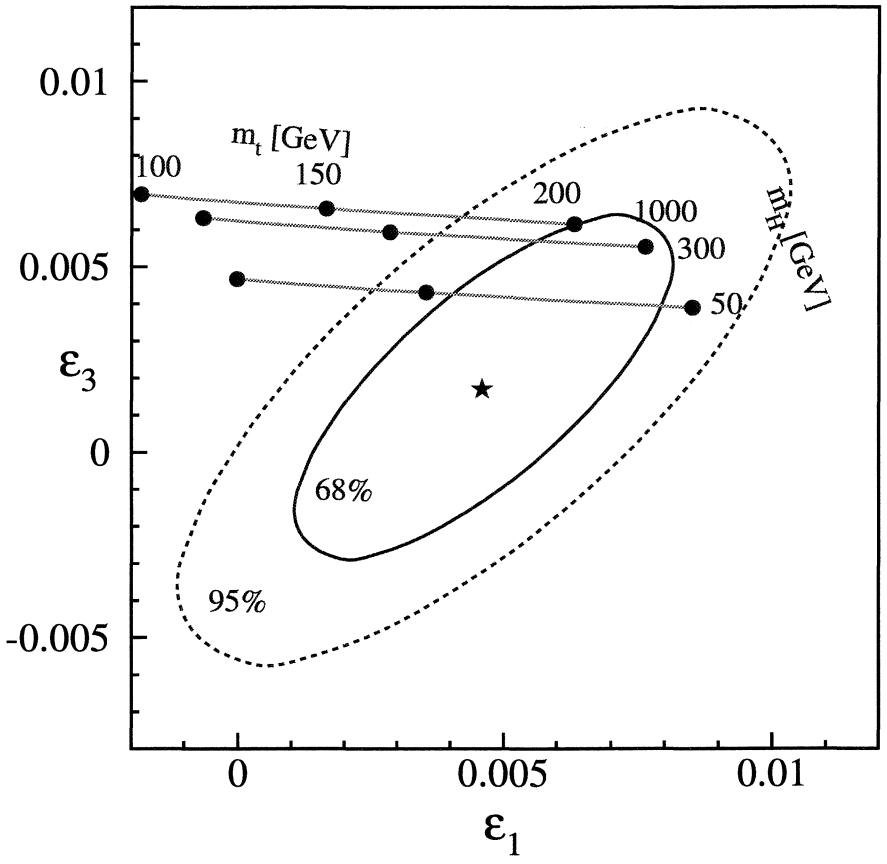

Figure 6.5: Correlation between the ϵ_1 and ϵ_3 parameters. The star indicates the central value of the fit. The solid line shows the 68% C.L. contour, the broken line, the 95% C.L. contour. The horizontal lines show the Standard Model predictions for different top quark masses and Higgs masses.

Chapter 7

Summary and Conclusion

In this thesis, I have studied Bhabha scattering at the Z resonance using the L3 detector at LEP. Detailed analysis on the cross section and forward-backward asymmetry measurements in L3 for the process $e^+e^- \rightarrow e^+e^-(n\gamma)$ have been presented.

The data sample analyzed in this thesis was collected during 1993 and 1994, which corresponds to $\approx 66,000$ e^+e^- pairs. The 1993 data was taken at three energy points (P-2, Peak, P+2), and the 1994 data was taken on the Z peak only.

The results on the cross section and forward-backward asymmetry measurements have been presented in Chapter 5. Here are the results from 1994 data on the peak:

$$\begin{aligned} \sigma &= 1.072 \pm 0.005\ (stat.) \pm 0.002\ (sys.)\ \text{nb} \\ A_{\text{FB}} &= 0.122 \pm 0.006\ (stat.) \pm 0.003\ (sys.). \end{aligned}$$

I have found that the radiative $e^+e^-(n\gamma)$ events with a certain topology, "*photon events*" (Section 5.1), are not well predicted by the Monte Carlo. To avoid this problem, I have developed a new TEC-based selection. I have been able to determine the TEC inefficiency to a precision of 0.1%, which makes it possible to control the systematic error on the cross section measurement to be $0.2 - 0.3\%$. The main contribution to the systematic error for the cross section measurement comes from selection criteria. For the forward-backward asymmetry measurement, it is from the charge determination for the scattered electron and positron. Both measurements on the Bhabha cross section and forward-backward asymmetry are dominated by

statistical errors.

The results of my cross section and forward-backward asymmetry measurements for the process $e^+e^- \rightarrow e^+e^-$ are combined with the results from other measurements (cross sections and leptonic forward-backward asymmetries for $e^+e^- \rightarrow f\bar{f}$, the $b\bar{b}$ forward-backward charge asymmetry, the partial width of Z decaying to b-quark, the quark charge asymmetry, the τ polarization, and the W mass) to determine the electroweak parameters and to check the consistency of the Standard Model. The main results are summarized as follows:

(1) The mass and the total and partial widths of the Z have been precisely measured:

$$\begin{aligned} M_Z &= 91188.3 \pm 2.9 \text{ MeV} \\ \Gamma_Z &= 2499.8 \pm 4.3 \text{ MeV} \\ \Gamma_e &= 83.99 \pm 0.26 \text{ MeV} \\ \Gamma_l &= 83.98 \pm 0.19 \text{ MeV}. \end{aligned}$$

These measurements allowed us to determine the number of light neutrino families from the width into unobserved final states:

$$N_\nu = 3.001 \pm 0.017.$$

The results on Γ_e and Γ_l are dominated by my measurement on the e^+e^- channel.

(2) The Z electroweak coupling constants to fermions are determined. No deviation from lepton universality is observed. All data are well-described by the Standard Model relations among the coupling constants

$$\overline{g}_V^l = -0.0398^{+0.0027}_{-0.0029}$$

$$\overline{g}^{l}_{\mathrm{A}} = -0.5010 \pm 0.0006.$$

The value of the effective weak mixing angle obtained by combining measurements ($A^{0,l}_{fb}$, τ polarization, $A^{0,b}_{fb}$) is:

$$\sin^2 \bar{\theta}_{\mathrm{W}} = 0.2304 \pm 0.0009.$$

(3) Taking account of measurements listed above, a combined fit in the framework of the Minimal Standard Model to the parameters M_Z, α_s, and M_t yields

$$\begin{aligned} M_t &= 189^{+12}_{-13} \pm 17 \text{ GeV} \\ M_H &= 91^{+230}_{-81} \text{ GeV} \\ &< 645 \text{ GeV} \quad 95\% \, C.L. \end{aligned}$$

(4) No indication of a deviation from the Standard Model prediction is found from the L3 electroweak data.

- Additional Z decays are constrained by:

$$\begin{aligned} \Delta\Gamma_Z &< 11.3 \text{ MeV} \\ \Delta\Gamma_{\mathrm{inv}} &< 7.4 \text{ MeV}. \end{aligned}$$

- No hint for the existence of an additional Z′ gauge boson is observed.

Further improvements on the electroweak parameters at the Z resonance are still expected from L3. At the moment, the lineshape analysis on 1995 data is still preliminary. The LEP energy is not yet finalized for 1993-1995 data. Much effort is

being put to reduce the theoretical uncertainty on the luminosity measurement to the level of 0.05%. Measurements on the partial width of Z decaying to b-quark, the quark charge asymmetry, and the τ polarization are expected to be updated with full LEP1 statistics. The mass of W boson is expected to be measured at LEP2 with an accuracy of 50 MeV, which will provide an additional precision test of the Standard Model. A crucial test of the Standard Model is the existence of the Higgs boson. The search for this last missing particle for the minimal Standard Model will cover up to $M_H \approx 95$ GeV mass region at LEP2 and to the entire mass range up to $M_H = 1$ TeV at LHC.

Appendix A

Calibration of the LEP Beam Energy

An important aspect in the determination of the mass and the total width of the Z is the precise knowledge of the LEP beam energy. The influence of the errors on the energy calibration can be seen through the correlation between the errors of the LEP energy on the off-peak points (P±2), and the errors on the Z mass and Z total width Γ_Z:

$$\Delta M_Z \approx 0.5\Delta(E_{+2} + E_{-2}) \tag{A.1}$$

$$\Delta\Gamma_Z \approx \frac{\Gamma_Z}{(E_{+2} - E_{-2})}\Delta(E_{+2} - E_{-2}), \tag{A.2}$$

where E_{+2} and E_{-2} are the luminosity-weighted center of mass energies at the two off-peak points. To match the statistical precision of the lineshape measurements, the values of E_{+2} and E_{-2} have to be known with an error of 0.002% or better. To achieve this goal, several techniques have been developed and are listed below. Emphasis is put on the resonant depolarization technique which is the most precise technique available.

The Field Display

The Field Display uses a rotating coil to provide a continuous measurement of the magnetic field in a reference dipole powered in series with the main ring magnets. The reference dipole does not contain mortar, unlike the LEP concrete-iron dipoles, and it

sits in a different temperature and humidity environment. The energy measured with the field display system, E_{FD}, is found to be related to the center-of-mass energy in the LEP ring as $E_{CM} = 2E_{FD} - 68$ MeV. Measurements were performed regularly and are used as a reference value for the energy of each individual fill of the machine. The reproducibility of the field display measurements is about $\pm 2.5 \times 10^{-5}$ [66].

The Flux-Loop

The flux loop system consists of closed electrical loops, each threading all the dipoles in one octant of the machine; the integrated induced voltage when altering the dipole currents is a direct measure of the magnetic field generated by the main ring dipoles. Absolute calibrations of the flux loop with a relative precision of about $\pm 10^{-4}$ were performed prior to installation of the magnets. However, the flux loop method is insensitive to constant fields and does not take into account additional bending by the quadrupole and sextupoles in the non-central orbits [65, 66].

Proton Calibration

This technique measures the particle momentum at 20 GeV in the central orbit. The length of the central orbit $\mathcal{C}$ is measured by injecting a 20 GeV positron beam into the ring:

$$\mathcal{C} = \frac{h_{e^+} \beta_{e^+} c}{f_{RF}}, \tag{A.3}$$

where $\beta_{e^+} = 1$. f_{RF} is the RF frequency and h_e is the harmonic number of the RF setting. The 20 GeV proton beam is injected into the LEP ring with the same magnetic lattice setting. Since the proton at 20 GeV is non-relativistic, the velocity of the proton can be evaluated from:

$$\beta_p = \frac{h_{e^+} f^p_{RF}}{h_p f^{e^+}_{RF}}. \tag{A.4}$$

Therefore, the particle momentum corresponding to the central orbit at LEP with 20 GeV beam energy setting is determined with an accuracy of $\pm 10^{-4}$. But the determination of the beam energy at 45 GeV depends on extrapolations of the magnetic field with flux-loop measurements, and hence leads to a degradation of precision to $\pm 2 \times 10^{-4}$ [64].

The Resonant Depolarization

The resonant depolarization technique [66] determines the beam energy by inducing a controlled spin-depolarizing resonance on a transversely polarized beam. A frequency-controlled radial RF magnetic field makes the particle spin direction precess away from the vertical axis. An artificial depolarizing resonance occurs when the radial magnetic field oscillates at the spin precession frequency, $\omega_{dep} \equiv \omega_s = 2\pi\nu_s f_{rev}$. The spin tune ν_s (number of spin precessions per revolution) is related to the beam energy via:

$$\nu_s \equiv a_e\gamma = \frac{E}{M_e c^2/a_e} = N_s + \delta\nu_s, \tag{A.5}$$

where $a_e \equiv (g-2)/2 = 1.159652188 \times 10^{-3}$ is the $e^{\pm}$ gyromagnetic anomaly known to a precision of some 10^{-9} and N_s is the integer part of the tune. A measurement of the depolarization frequency at the resonance $f_{dep}^{res} = \delta\nu_s \times f_{rev}$ gives the non-integer part, $\delta\nu_s$, of the spin tune and defines the beam energy in the arcs:

$$E_{beam} = \frac{m_e c^2}{a_e}\nu_s = 0.4406486(N_s + \frac{f_{dep}^{res}}{f_{rev}}). \tag{A.6}$$

The integer part of the spin tune is $N_s = 103$ for $E_{beam} = 45.6$ GeV.

These measurements, taken at conditions close to the physics condition, give the average beam energy at the calibration time with an error below 1 MeV. Since the resonant depolarization calibration cannot be performed during the physics run, their results need to be extrapolated to the beam energy at different interaction points for

each individual physics fill. The typical time variations of the LEP energy is of the order of 1 MeV per hour. Extensive monitoring of the magnetic field and the orbit are provided by the field-display system, the flux-loop system, the NMR probe(s) and the Beam Online Monitor (BOM) system. The energy of LEP is calculated in 15 minute intervals for each interaction point for every physics fill, based on a model that describes the variations of the magnetic field and orbit the particles encounter along their orbit in the ring.

With such careful monitoring, several systematic effects leading to the variation of the energy of the beam have been identified and are summarized as follows.

RF effect

The difference of the beam energy at different interaction points, *RF effects* [65, 66], arise from the alignment error of the RF units, placed left and right of the interaction point 2 (IP2 L3) and 6 (IP6, OPAL) to compensate for the loss of the beam energy due to synchrotron radiation. The beam energy at the L3 and OPAL interaction points are higher by about 10 MeV than the average energy in the LEP arc. An energy correction, taking into account the operating status of the RF units and their alignment, has been applied to correct the IP-dependent RF effect.

Tidal effect

The tidal forces from the moon, and to a smaller extent, from the sun, distort the spheroidal shape of the earth. The attraction of these objects produces two symmetric bulges on the surface of the earth. The inclination of the rotational axis of the earth with respect to the plane of the moon's orbit introduces an asymmetry in the two daily tides. The local change of the earth's radius induces a small expansion of the solid surfaces of the earth's crust. The 4.24 km radius of LEP is changed by 0.15 mm, which corresponds to an energy change of about 8 MeV from low to high tide [67].

Train effect

Variations of the LEP beam energy during a physics fill have been observed and traced back to changes in the bending field experienced by the beams as monitored by the NMR probes since 1995. It was discovered that the LEP magnetic bending field and hence the beam energy is changed by a current flow over the vacuum pipe. The current is created by the DC powered trains traveling between the Geneva main station and destinations in France. The rail current leaks to earth and returns to the power station via the LEP tunnel where the vacuum pipe is one of the conductors. Train leakage currents penetrate LEP at the injection lines from the SPS close to IP1 and leave near IP6. The observed changes in B field cause a beam energy increase of several MeV over a fill. Many careful investigations are in progress, but the current status doesn't allow a final quantitative statement [68].

Beam offset effect

In 1995, LEP was operated in the bunch-train mode. In this mode of operation, vertical dispersion of the beam causes a shift in the center of mass energy. Vertical dispersions are produced due to the effect of the electrostatic separators which are used to avoid unwanted collisions. Particles moving in a non-central orbit with a displacement relative to the nominal orbit plane have energy differences ΔE relative to the nominal beam energy. If the vertical displacements of electron and positron beams are different at the interaction point, the shift in the center of mass energy is given by:

$$\Delta E_{CM} = -\frac{1}{2}\frac{\delta y}{\sigma_y^2}\Delta D_y, \tag{A.7}$$

where δy is the collision offset, and ΔD_y, the vertical dispersion difference between the colliding beams. E and σ_E are the beam energy and the energy spread. The beam offset effect causes a shift of center of mass energy by several MeV at the interaction

point [69].

Beam Spread

The energy distribution of the particles in the LEP beams has a finite width due to synchrotron oscillations. From the observed bunch lengths, an effective spread of the center-of-mass energy around the nominal value is deduced to be 55 MeV with an error of 1 MeV. Therefore, the experiments observe a convolution of cross sections at energies spreading around a central value. The correction from the beam spread effect is the largest for the cross sections at the Z peak (0.16%). The uncertainty on the beam spread translates to ± 0.2 MeV additional error on Γ_Z [70, 71].

Status of LEP Energy Calibration at LEP1

Table A.1 summarizes the status of LEP energy calibration at LEP1. Results for the 1993-1995 period are still preliminary [71].

Period	ΔE_b [MeV]	Center-of-mass energy
1990	29	M_Z, $M_Z \pm 1, 2, 3$ GeV
1991 Prescan	20	M_Z
1991 Scan	5.7	M_Z, $M_Z \pm 1, 2, 3$ GeV
1992	20	M_Z
1993 Prescan	18	M_Z
1993 Scan	3.5	$M_Z - 2$ GeV
1993 Scan	6.7	M_Z
1993 Scan	3.0	$M_Z + 2$ GeV
1994	3.7	M_Z
1995 Prescan	10	M_Z
1995 Scan	1.8	$M_Z - 2$ GeV
1995 Scan	5.4	M_Z
1995 Scan	1.7	$M_Z + 2$ GeV

Table A.1: Status for the LEP energy calibration for 1990-1995. Results on 1993-1995 are still preliminary.

Appendix B

Luminosity Measurement at L3

The luminosity measurement plays a crucial role in the precise determination of cross sections since the integrated luminosity serves as an absolute normalization for the event rates recorded in the detectors. A measurement with precision of 10^{-3} is realized in L3 [62] with a luminosity monitor consisting of a BGO calorimeter and a silicon tracker (SLUM) (See Section 3.2.7). The luminosity is determined using the large rate of small angle Bhabha scattering (See Chapter 2.2.1) through:

$$\mathcal{L} = \frac{N_{event}}{\sigma}, \tag{B.1}$$

where N_{event} is the number of events from small angle Bhabha scattering, and σ is the cross section for this QED process which is peaked in the forward region with a typical value of $\sigma \approx 88.5$ nb for the acceptance of the L3 LUMI monitor. $\mathcal{L}$ is known theoretically with a precision of 0.11% [63].

B.1 Event Selection

The Bhabha event selections are based on the energies of the electrons deposited in the BGO LUMI and the direction of the electrons reconstructed using the hits in the silicon tracker. The selection criteria are listed below:

- $max(E_1, E_2) > 0.8\ (0.95) \cdot E_{beam}$ and $min(E_1, E_2) > 0.4\ (0.2) \cdot E_{beam}$; E_1 and E_2 are the reconstructed energies of the two electrons; the asymmetry cut is chosen

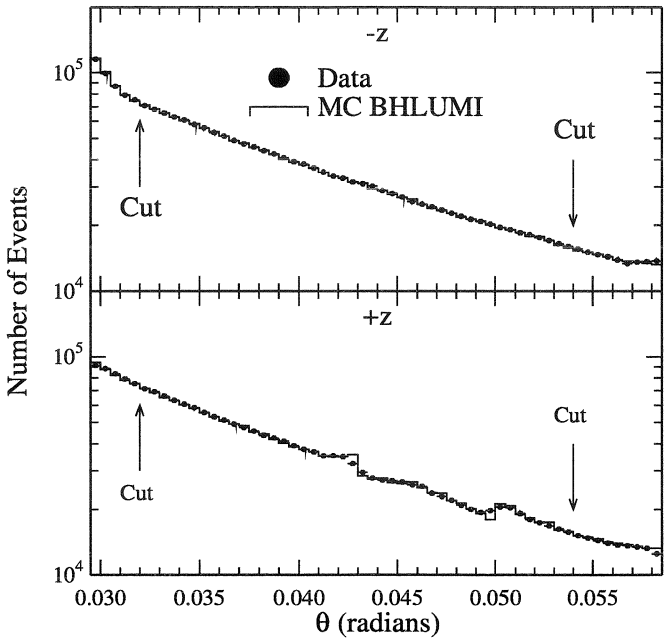

Figure B.1: The polar angle distribution of the reconstructed Bhabha events for the -z and +z sides from the data and the Monte Carlo. The difference between the -z and +z sides is due to the different shape of the LEP beam pipe of the two sides.

to be insensitive to the radiative events and to the energy leakage through the gaps between the crystals.

- The acoplanarity $|180^0 - \Delta\phi|$ should be less than 10^0, where $\Delta\phi$ is the difference between the azimuthal angles of the two electrons.

- The fiducial volume is defined by asymmetry requirements with a *tight* cut on one side of the detector and a *loose* cut on the other side in order to minimize the sensitivity to the offsets of the detectors with respect to the beam axis:

  - *Tight* $32 < \theta < 54$ *mrad*, $|\phi - 90^0| < 11.25^0$ and $|\phi - 270^0| < 11.25^0$,
  - *Loose* $27 < \theta < 65$ *mrad*, $|\phi - 90^0| > 3.75^0$ and $|\phi - 270^0| < 3.75^0$,

where θ and ϕ are the polar angle and the azimuthal angle for the reconstructed electrons.

Figure B.1 shows the good agreement between the LUMI data collected (with the SLUM installed) and the prediction of the BHLUMI Monte-Carlo program for the polar angle distribution of the reconstructed Bhabha events.

B.2 Systematic Error

The systematic errors on the luminosity determination are summarized in Table B.1. With the precise knowledge of the geometry using the silicon tracker, the experimental error on the luminosity measurement has been improved since 1993 by a factor of 6. The total systematic error is dominated by the theoretical uncertainty on the small angle Bhabha cross section.

Source	Contribution to $\Delta\mathcal{L}/\mathcal{L}$ (%)		
	BGO Analysis	BGO+Silicon Analysis	
		1993	1994
Trigger	Negligible	Negligible	Negligible
Event Selection	0.3	0.04	0.05
Background	Negligible	Negligible	Negligible
Geometry	0.4	0.06	0.03
Total Experimental	0.5	0.08	0.05
Monte Carlo Statistics	0.06	0.06	
Theory	0.11	0.11	
Total	0.6	0.15	0.14

Table B.1: Systematic uncertainties on the luminosity measurement.

Theoretical Uncertainty

The theoretical uncertainty, 0.11%, is realized through a second order Monte Carlo calculation by Jadach *et al.* [63], which includes numerically integrated terms through

order $\alpha^2 L^2$ (L is the familiar "leading logarithmic" factor $(\alpha/\pi) ln(\mid t \mid /m_e^2)$ and t is the usual squared four-momentum transfer). The leading theoretical systematic errors remaining are the dominant $\alpha^2 L$ photonic QED contribution (0.10%) and the uncertainty in hadronic vacuum polarization (0.04%). This calculation has been made available to experimentalists through a complete Monte Carlo program: BHLUMI 4.0.4 [63].

Appendix C

$f\bar{f}$ Productions at $\sqrt{s} \gg M_Z$

After having delivered 4 million Z particles for each experiment, LEP began a series of energy upgrades. After a brief run of 27 days in November 1995 (LEP 1.5) with 130 GeV $< \sqrt{s} <$ 140 GeV, LEP entered its second phase LEP 2 and started to run above the WW pair production threshold in 1996. Table C.1 lists the luminosity the L3 detector recorded in 1996 [73] and in the LEP 1.5 [72] [1].

Since the typical s-channel cross sections at these high energies are 10^{-2} of those at the Z peak, the precisions of the cross section measurements at these high energies are at the $1 - 10\%$ level. These high energy data provide us with a check for the Standard Model at $\sqrt{s} \gg M_Z$ and their sensitivity to the γZ interference allows us to determine the γZ interference term in the S-matrix formalism [74].

	LEP 1.5			LEP 2		
$\sqrt{s}$ [GeV]	130.3	136.3	140.2	161.3	170.3	172.3
$\mathcal{L}$ [pb^{-}1]	2.74	2.25	0.05	10.0	1.0	8.5

Table C.1: Luminosity recorded by the L3 detector in LEP1.5 and in LEP 2 of 1996.

[1] On July 31, 1997, LEP started to run at an energy of 183 GeV. Up until September 1, L3 has recorded a luminosity of 12.3 pb^{-1} at this high energy.

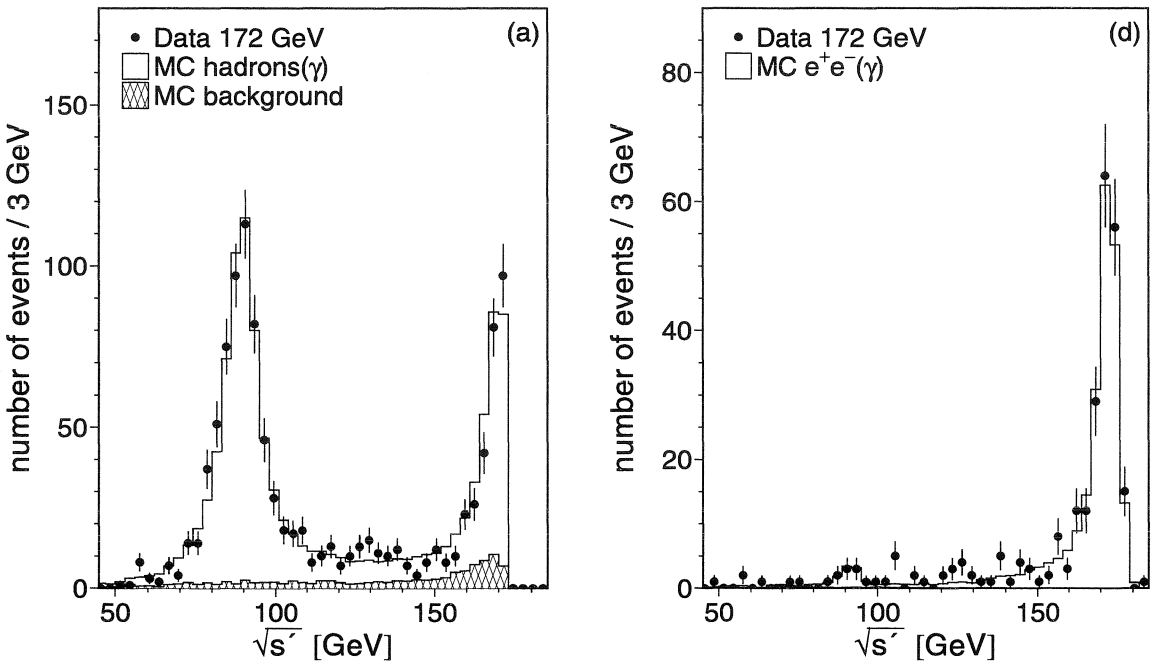

Figure C.1: $\sqrt{s'}$ distribution of $q\bar{q}$ and e^+e^- events at 172 GeV.

C.1 Characteristics of the High Energy Data

The special feature for the events of the high energy runs is that a large fraction of the events ($\approx$ 70% for $q\bar{q}$ events) have hard initial state radiation (ISR) such that the effective-center-mass-of energy $\sqrt{s'}$ is lowered to be at the Z resonance. These "radiative Z return" events undergo the same physical decay processes as the Z events at LEP 1. A cut on $\sqrt{s'}$ allows a separation between the events at high effective center-of-mass energies, "genuine high energy events," and the "radiative Z return events."

The $e^+e^- \rightarrow e^+e^-(n\gamma)$ process is dominated by the t-channel contribution at high energies; therefore, its fraction of "radiative Z return events" is much smaller ($\approx$ 15%).

$\sqrt{s'}$ is determined in the following ways: if the ISR γ is detected, $s' = s - 2E_\gamma\sqrt{s}$; otherwise, kinematic constraints are used to derive $\sqrt{s'}$ with the assumption that the

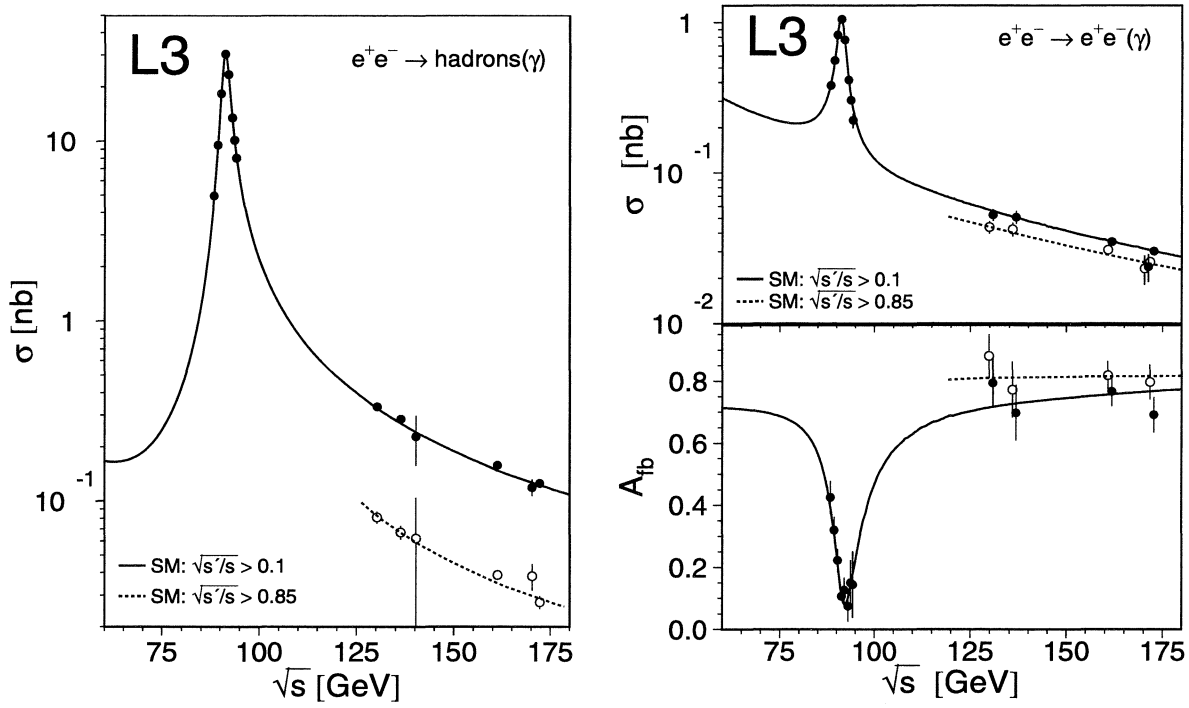

Figure C.2: Left: cross sections of the process $e^+e^- \to$ hadrons(γ); Right: cross section and forward-backward asymmetry of the process $e^+e^- \to e^+e^-(\gamma)$. Solid (open) dots for the total (genuine high energy) sample. The SM predictions are shown as a solid line for the total sample and as a dashed line for the high energy sample. Measurements at the Z resonance are also included.

ISR γ is along the beam pipe. Figure C.1 shows distribution of $\sqrt{s'}$ from L3: the double-peak structure is from the "genuine high energy events" and the "radiative Z return events." The "radiative Z return event " peak of the e^+e^- events is apparently much less prominent than that of the $q\bar{q}$ events. A cut of $\sqrt{s'} > 0.85\sqrt{s}$ is used to separate the "genuine high energy events" from the "radiative Z return events."

C.2 Production Results at High Energies

The cross section and forward-backward asymmetry measurements have been applied to two samples: the inclusive total event sample and the exclusive "genuine high

energy" event sample. Examples of the results [73] are illustrated in Figure C.2. The results from the high energy runs agree with Standard Model predictions.

C.3 Interpretation of the Results

In the S-Matrix formalism [74], the hadronic γZ interference term is scaled by the parameter j_{had}, which was fixed to the SM value 0.22 in the lineshape fits to the LEP 1 data [44]. The error on M_Z increase sizably if j_{had} is left free in the fits due to the strong anticorrelation between j_{had} and M_Z (Figure C.3). Inclusion of the measurements from $\sqrt{s} \gg M_Z$, which are very sensitive to the γZ interference term, allows a simultaneous determination of j_{had} and M_Z. The results of j_{had} and M_Z [44] are as follows:

$$\begin{aligned} j_{had} &= 0.34 \pm 0.28 \\ M_Z &= 91185.5 \pm 5.6. \end{aligned}$$

Comparing the results for M_Z obtained with fixed j_{had} and the results of the S-matrix approach, we find that the experimental uncertainty on j_{had} adds an uncertainty of about ± 4.8 MeV to M_Z.

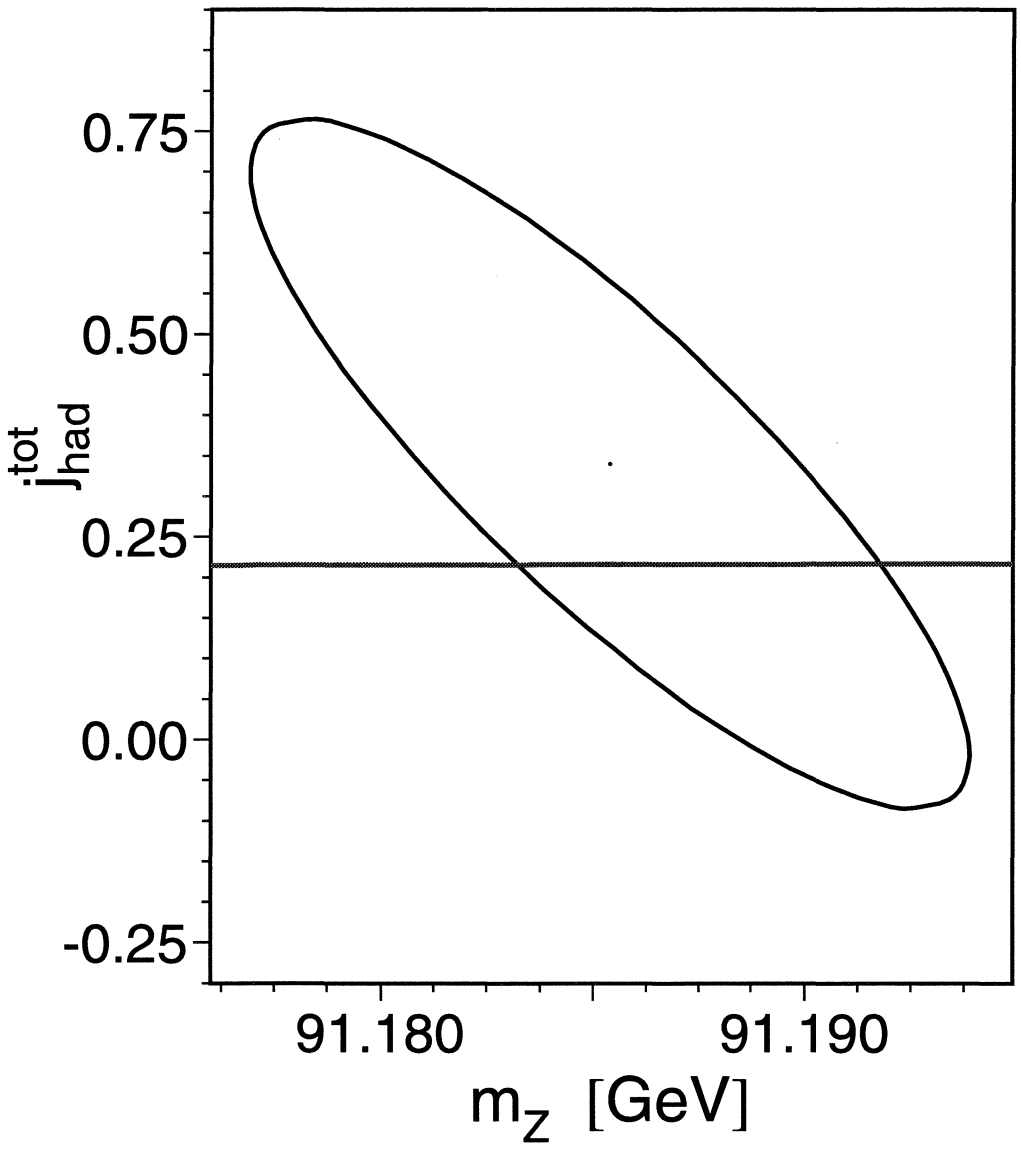

Figure C.3: The 68% C.L. contour of j_{had} and $\mathrm{M_Z}$.

Appendix D

Theoretical Calculations on Large Angle Bhabha Scattering

This appendix is devoted to a summary of theoretical calculations on large angle Bhabha scattering. To compare the experimental data with theory with a desired level of accuracy, the theoretical calculations are usually expressed through two kinds of programs: semi-analytical calculations and Monte Carlo generators. *Semi-analytical* refers to the fact that the analytical computation has at least one integration performed numerically. The two approaches have distinct different features.

- Monte Carlo calculations are more readily adapted to experiments, compared to semi-analytical calculations:
  - semi-analytical calculations give inclusive results such as the total cross section or forward-backward asymmetry while Monte Carlo generators are able to provide much more exclusive results;
  - semi-analytical calculations allow some cuts on the variables while Monte Carlo generators allow many more cuts.
- Semi-analytical calculations have their advantages over the Monte Carlo generators that they can be used to check the Monte Carlo calculations and to study tiny effects due to changes of parameters such as M_t or M_H. These advantages arise from the following facts:

- semi-analytical calculations are usually much faster compared to the Monte Carlo calculations;
- semi-analytical calculations are usually free of statistical errors while for Monte Carlo calculations there always exist statistical errors with a scale of $N^{-1/2}$, where N is the number of events generated.

A brief review of the programs currently available is provided below.

D.1 Semi-Analytical Calculations

ALIBABA

The name ALIBABA stands for "A (semi) analytical leading log improved Bhabha scattering calculation" [42]. The program calculates the cross section and forward-backward asymmetry with implementation of exact $\mathcal{O}(\alpha)$ QED and weak corrections. The higher order QED corrections consists of leading log $\mathcal{O}(\alpha^2)$ corrections plus soft-photon exponentiation.

ALIBABA is able to incorporate realistic experimental cuts: minimum and maximum scattering angles for both electron and positrons; minimum energies of the electron and positron in the final state and the maximum acollinearity between the final state leptons. Since ALIBABA is intended especially for large angle Bhabha scattering, the minimal scattering angle should be larger than 10°.

The accuracy of ALIBABA is 0.5%. It has served as the benchmark for theoretical calculations on large angle Bhabha scattering. Since it is rather time consuming in computation, ALIBABA is not used directly in the fitting for the Z parameters. It is used to calculate the t-channel and s-t interference contribution in the special procedure, *t-channel subtraction*, described in Section 7.1.1.

TOPAZ0

The program TOPAZ0 [75] is designed for computing Z parameters, de-convoluted and QED-dressed cross sections and forward-backward asymmetries of e^+e^- annihilation into fermion pairs and of Bhabha scattering around the Z peak.

Compared to ALIBABA whose electroweak library is not updated, TOPAZ0 includes the state-of-the-art weak and QCD corrections according to Ref. [76]. The QED corrections are exactly treated at $\mathcal{O}(\alpha)$ for s-channel processes (leptonic and hadronic), at the leading logarithmic level for pure t-channel and s-t interference contribution in the Bhabha case. Higher order QED corrections are taken into account using the structure function approach.

As ALIBABA, TOPAZ0 is able to incorporate the realistic experimental cuts as well. But the angular acceptance of the scattered antifermion in TOPAZ0 is assumed to be larger than the one of the scattered fermion. Its prediction for Bhabha scattering is also limited to the large angular region ($\theta > 10°$).

For TOPAZ0, particular care has been devoted to computing efficiency and speed, both for s-channel fermion productions and Bhabha channel. Therefore, TOPAZ0 can serve as a fitting package and it can avoid the t-channel subtraction for the Bhabha channel.

D.2 Monte Carlo Programs

BABAMC

The generator BABAMC [37] is one of the first attempts at describing Bhabha scattering to the percent level of precision. It includes first order radiative QED corrections such that it can simulate events with up to one photon in the final state. A complete lowest-order electroweak treatment is implemented.

BABAMC can be used for both large angle Bhabha scattering where the s-channel

with Z exchange dominates, and small angle Bhabha scattering where the t-channel γ exchange dominates.

BHAGENE3

The Monte Carlo generator, BHAGENE3 [36], is a generalization of BABAMC. The program includes one-loop and the most important two-loop electroweak as well as QED corrections. $\mathcal{O}(\alpha)$ QED corrections are treated exactly, retaining all lepton mass terms, as in BABAMC. Higher order QED corrections are included in an improved soft photon approximation with exponentiation of initial state radiation. Up to three hard final state photons are generated. The minimum scattering angle for percent level cross section accuracy is 10°. The program was designed for the Z peak region but has been checked to be valid for the LEP2 energies.

UNIBAB

UNIBAB [38] is a full Monte Carlo generator designed originally for large angle Bhabha scattering at LEP1 and SLC energies. The QED radiative corrections are calculated through a photon shower algorithm and are implemented in a fully factorized form in the structure function approach. The electroweak library is based on ALIBABA.

UNIBAB assumes s-channel dominance and does not include the QED initial-final interference corrections. Therefore, the program should be only used in the vicinity of the Z peak and only for not too large or too small scattering angles ($10° < \theta < 170°$).

BHWIDE

BHWIDE [39] is a new multiple photon Monte Carlo event generator for large angle Bhabha scattering. In many aspects, BHWIDE is very similar to BHLUMI [63] and can be considered as its extension to large angles. Using the framework of $\mathcal{O}(\alpha)$ YFS

exponentiation as BHLUMI, BHWIDE includes the effects of the Z exchange graphs and the effects of the pure weak one-loop corrections. The $\mathcal{O}(\alpha)$ virtual (both weak and QED) corrections are taken from ALIBABA or BABAMC - an option for the user. The program provides the full event in terms of particle flavors and their four-momenta with an arbitrary number of radiative photons. A precision of 0.3%(0.5%) in the LEP1/SLC regime within $\pm$ 100 MeV (+2.75/-2.5 GeV) of the Z peak is claimed for the cross section. For LEP2, the corresponding precision is currently estimated to be 1.5%.

References

[1] S. Glashow, Nucl. Phys. 22.(1961) 579;
S. Weinberg, Phys. Rev. Lett 19 (1967) 1264;
A. Salam, in Elementary Particle Theory, ed.: N. Svarthold, Almqvist and Wiksell, Stockholm (1968) 367.

[2] E. Fermi, *Versuch einer Theorie der β -Strahlen*, Z. Phys. 88 (1934) 161.

[3] M. Gell-Mann and R. Feynman, Phys. Rev. 109 (1958) 193.

[4] C. Yang and R. Mills, Phys. Rev. 96 (1954) 191.

[5] P. Higgs, Phys. Lett. 12 (1964) 132; 13(1964) 508; 145 (1966) 1156.

[6] G. t'Hooft, Nucl. Phys. B 33 (1971) 173, B 35 (1971) 167.

[7] J. Goldstone, Nuovo Cim. 19 (1961) 154.

[8] E. R. Cohen and B. N. Taylor, Rev. Mod. Phys. 59(1987) 1121;
E. R. Cohen and B. N. Taylor, Inst. Stand. Technol. 95 (1990) 497.

[9] Particle Data Group, *Review of Particle Properties* , Phys. Rev. D 50 (1994) 1171.

[10] R. E. Behrends, R. J. Finkelstein, A. Sirlin, Phys. Rev. 101(1956) 866.

[11] The L3 Collaboration, M. Acciarri *et al.*, *Search for the Standard Model Higgs Boson in* e^+e^- *interactions at* $161 < \sqrt{s} < 172$ GeV,
July 1997, CERN preprint CERN-PPE/97-81, Phys. Lett.B accepted.

[12] Particle Data Group, *Review of Particle Properties*, Phys. Rev. D 54 (241).

[13] M. Caffo, E. Remiddi and F. Semeria, *Z Physics at LEP 1*, eds. G. Altarelli *et al.*, CERN-89-08, Vol 1 (1989) 171.

[14] M. Consoli and W. Hollik, *Z Physics at LEP 1*, eds. G. Altarelli *et al.*, CERN-89-08, Vol 1 (1989) 7.

[15] F. A. Berends, *Z Physics at LEP 1*, eds. G. Altarelli *et al.*, CERN-89-08, Vol 1 (1989) 89.

[16] G. Burfers *et al.*, *Z Physics at LEP 1*, eds. G. Altarelli *et al.*, CERN-89-08, Vol 1 (1989).

[17] L. Camilleri *et al.*, *Physics with Very High Energy* e^+e^- *Colliding Beams*, Preprint CERN/76-18, CERN, 1976.

[18] European Committee for Future Accelerators, General meeting on LEP, Villars-sur-Ollon, ECFA 81054, 1981.

[19] ALEPH Collab., D. Decamp *et al.*, Nucl. Inst. Meth. A 294 (1990) 121.

[20] DELPHI Collab., P. Aarnio *et al.*, Nucl. Inst. Meth. A 303 (1990) 233.

[21] L3 Collab., B. Adeva *et al.*, Nucl. Inst. Meth. A 289 (1990) 35.

[22] OPAL Collab., K. Ahmet *et al.*, Nucl. Inst. Meth. A 305 (1991) 275.

[23] High-Luminosity Options for LEP, ed. J. M. Jowett, CERN 91-02, CERN 1991.

[24] Proceedings of the 3^{rd} Workshop on LEP performance, ef. J. Poole, CERN-SL/93-19, CERN, 1993.

[25] E. Keil, CERN-SL/92-55(AP);
E. Keil, Proceedings of the third workshop on LEP performance,

CERN-SL/93-16 (1993) 459;
W. Herr, Proceedings of the fourth workshop on LEP performance,
CERN-SL/94-06 (1994) 323.

[26] T. Camporesi *et al.*, *Reports from the Bunch Train Working Group*, CERN-LEPC/94-13 (1994).

[27] M. Acciari *et al.*, Nucl. Inst. Meth. A 351 (1994) 300.

[28] L3 note 1712, *Calibration of the L3 Electromagnetic Calorimeter in an Electron Beam*, 1995.

[29] L3 note 1319, *Results on the calibration of the L3 BGO calorimeter with cosmic rays*, CERN-PPE/93-184, 1993.

[30] A. Bay *et al.*, *The Xenon monitor of the L3 electromagnetic calorimeter*, Nucl. Inst. Meth. A321 (1992) 119-128.

[31] K. N. Leung *et al.*, Rev. Sci. Instrum. 62 (1991) 100.

[32] J. Patrick Rymer, G. A. Engeman, R. W. Hamm, and J. M. Potter, *A Compact RF Driven H- Ion Source for Linac Injection*, Proc. 1991 IEEE Particle Accelerator Conference, IEEE Cat. No. 91CH3038-7,1910-1912(1991).

[33] AccSys Technology Inc., 1177 Quarry Ln., Pleasanton, CA 94566, USA.

[34] H. Ma, H. Newman, R. Y. Zhu, and R. Hamm,
Nucl. Instr. Meth. A281 (1989) 467;
H. Ma, *et al.*, Nucl. Instr. Meth. A274 (1989) 113.

[35] Private communication with H. Newman.

[36] J. H. Field, Phys. Lett. B323, 432 (1994);
J. H. Field and T. Riemann, report UGVA-DPNC 1995/6-166, DESY 95-100, to be published.

[37] M. Böhm, A. Denner and W. Hollik, Nucl. Phys. B304 (1988) 687;
F. A. Berends, R. Kleiss and W. Hollik, Nucl. Phys. B304 (1988) 712.

[38] H. Anlauf *et al.*, Comput. Phys. Commun. 79, 466 (1994).

[39] S. Jadach, W. Placzek, and B. F.K.Ward, preprint UTHEP-95-1001.

[40] S. Jadach *et al.*, in *Z Physics at LEP 1* , ed. G. Altarelli *et al.*, CERN/89-08, Vol 3 (1989) 69;
S. Jadach and B. F. L. Ward, Phys. Lett. B274 (1992) 470.

[41] ZFITTER 4.9, D. Bardin, *et al.*, Preprint CERN-TH/6443/92.

[42] ALIBABA, W. Beenakker, F. Berends and S. van der Marck, Nucl. Phys. B 349 (1991) 323.

[43] The Working Group on LEP Energy, *LEP Energy Calibration in 1993, 1994 and 1995*, Internal Note. LEP Energy Group/96-05, July 1996.

[44] L3 note 2065, *Preliminary L3 Results on Electroweak Parameters from 1990-96 Data*, 1997.

[45] F. James, CERN Program Library Long Writeup D506 MINUIT, CERN 1993.

[46] L3 Collab., M. Acciarri *et al.*, Z. Phys. C 62 (1994) 551.
Measurement of Cross Sections and Leptonic Forward-Backward Asymmetries at the Z Pole and Determination of Electroweak Parameters.

[47] C. Luci, talk given at ASPEN Winter Conference on Particle Physics, January 23 1997.

[48] S. Eidelmann and F. Jegerlehner, *Hadronic contribution to (g-2) of the leptons and to the effective fine structure constant* α_Z PSI-PR-95-1, BUDKERINP 95-5, January 1995.

[49] L3 Collab., M. Acciarri *et al.*, *Results from the L3 Experiment at LEP*, Physics Reports. 236 (1993) 1.

[50] CDF Collaboration, J. Lys, presented at ICHEP96, Waraw, 25-31 July 1996.

[51] D0 Collaboration, S. Protopopescu, presented at ICHEP96, Waraw, 25-31 July 1996.

[52] L3 note 1793, *A Preliminary Measurement of* A_e *and* A_τ, 1995.

[53] L3 note 2072, *L3* A_{FB}^b *Results for Moriond 97*, 1997.

[54] L3 note 2063, *Forward-Backward Charge Asymmetry Measurement on '91-'94 Data*, 1997.

[55] L3 note 2067, *Preliminary L3 Results of Higgs Searches at* $\sqrt{s} = 161-172$ GeV, 1997.

[56] L3 Collab., *Measurement of* R_b *with the L3 Detector*,
paper contributed to the Warsaw Conference, L3, CERN, 1996.

[57] L3 note 2057, *Preliminary Results on the Pair Production of W Bosons in* e^+e^- *Interactions at* $\sqrt{s} = 172$ GeV, 1997.

[58] M. Rijssenbeek, *Measurements of the Mass of the W Boson from CDF/D0.*
to appear in the proceedings of 28th International Conference on High Energy Physics, 25-31 July 1996, Warsaw, Poland.

[59] A. Leike, S. Riemann and T. Riemann, Univ. Munich. Preprint LMU-91/06, and FORTRAN program ZEFIT;
A. Leike, S. Riemann and T. Riemann, Phys. Lett. B291 (1992) 187.

[60] S. Riemann, L3 Note 1923, March 12, 1996.

[61] G. Altarelli, R. Barbieri and S. Jadach, Nucl. Phys. B 369 (1992) 3 and Nucl. Phys. B 376 (1992) 444;
G. Altarelli, R. barbieri and F. Caravaglios, Nucl. Phys. B 405 (1993) 3 .

[62] L3 Luminosity Collaboration, I. C. Brock *et al.*, Nucl. Inst. Meth A 381 (1996) 236.

[63] S. Jadach *et al.*, *Upgrade of the Monte Carlo program BHLUMI for Bhabha Scattering at low angles to version 4.04*, CERN-TH/96-158.

[64] The working group on LEP energy and LEP collaborations ALEPH, DELPHI, L3 and OPAL.
Measurement of the mass of the Z boson and energy calibration of LEP ,
Phys. Lett. B 307 (1993) 187, CERN-SL.93-17.

[65] The working group on LEP energy *The Energy Calibration of LEP in the 1991*, CERN-SL.92-37.

[66] The working group on LEP energy *The Energy Calibration of LEP in the 1993 Scan*, CERN-SL.95-02.

[67] L. Arnauon *et al.*, *Effects on Terrestial Tides on the LEP Beam Energy*, CERN-SL. 92-37(DI).

[68] G. Grun *et al.*, *A newly observed effect affects the LEP beam energy*, CERN-SL.96-036.

[69] M. Böge *et al.*, *Measurements of Collision Offsets and Difference in Vertical Dispersion at the LEP Interaction Points*, CERN-SL. 96-035.

[70] B. Jacobsen *1993 LEP Energy Spread and Variation From Spot Size Measurements* ALEPH 94-060.

[71] The Working Group on LEP Energy, paper in preparation.

[72] The L3 Collaboration, M. Acciarri *et al.*,
Measurement of Hadron and Lepton-Pair Production at 130 *GeV* $< \sqrt{s} <$ 140 *GeV at LEP.* CERN preprint CERN-PPE/95-191, Phys. Lett. B 370 (1996) 195-210.

[73] The L3 Collaboration, M. Acciarri *et al.*,
Measurement of Hadron and Lepton-Pair Production at 161 GeV $< \sqrt{s} <$ 172 GeV *at LEP.* CERN preprint CERN-PPE/97-52, Phys. Lett. B accepted.

[74] A. Leike, T. Riemann, J. Rose, Phys. Lett. B 273 (1991) 513;
T. Riemann, Phys. Lett. B 293 (1992) 451;
S. Kirsch, T. Riemann, Comp. Phys. Comm. 88 (1995) 89.

[75] G. Montagna, O. Nicrosini, G. Passarino and F. Piccinini, Comput. Phys. Commun. 93, 120 (1996).
G. Montagna *et al.*, Comput. Phys. Commun. 76, 328 (1993).
G. Montagna *et al.*, Nucl. Phys. B401, 3 (1993).

[76] D. Bardin *et al.*, Electroweak Working Group Reports,
Reports of the Working Group on Precision Calculations for the Z Resonance, CERN Report 95-03, eds. D. Bardin, W. Hollik and G. Passarino (Geneva, 1995).